

INFORMATION TO USERS

This manuscript has been reproduced from the microfilm master. UMI films the text directly from the original or copy submitted. Thus, some thesis and dissertation copies are in typewriter face, while others may be from any type of computer printer.

The quality of this reproduction is dependent upon the quality of the copy submitted. Broken or indistinct print, colored or poor quality illustrations and photographs, print bleedthrough, substandard margins, and improper alignment can adversely affect reproduction.

In the unlikely event that the author did not send UMI a complete manuscript and there are missing pages, these will be noted. Also, if unauthorized copyright material had to be removed, a note will indicate the deletion.

Oversize materials (e.g., maps, drawings, charts) are reproduced by sectioning the original, beginning at the upper left-hand corner and continuing from left to right in equal sections with small overlaps. Each original is also photographed in one exposure and is included in reduced form at the back of the book.

Photographs included in the original manuscript have been reproduced xerographically in this copy. Higher quality 6" x 9" black and white photographic prints are available for any photographs or illustrations appearing in this copy for an additional charge. Contact UMI directly to order.

UMI

A Bell & Howell Information Company
300 North Zeeb Road, Ann Arbor MI 48106-1346 USA
313/761-4700 800/521-0600

Dynamical processes in the middle atmosphere as observed from
Upper Atmosphere Research Satellite limb-sounding data

by

Douglas Ray Allen

A dissertation submitted to the graduate faculty
in partial fulfillment of the requirements for the degree of
DOCTOR OF PHILOSOPHY

Major: Physics

Major Professor: John L. Stanford

Iowa State University

Ames, Iowa

1997

UMI Number: 9737681

UMI Microform 9737681
Copyright 1997, by UMI Company. All rights reserved.

**This microform edition is protected against unauthorized
copying under Title 17, United States Code.**

UMI
300 North Zeeb Road
Ann Arbor, MI 48103

Graduate College
Iowa State University

This is to certify that the Doctoral dissertation of
Douglas Ray Allen
has met the dissertation requirements of Iowa State University

Signature was redacted for privacy.

Major Professor

Signature was redacted for privacy.

For the Major Program

Signature was redacted for privacy.

For the Graduate College

DEDICATION

This dissertation is dedicated to my wife, Ruthie, who's support and encouragement through the last five years have been beyond measure. Also to my son, Peter, in whom I hope to instill wonder at the beauty not only in a cloud, rainbow, and sunset, but also in the "unseen" motions of the earth's atmosphere.

The heavens declare the glory of God:

the skies proclaim His handiwork.

Day after day they pour forth speech:

night after night they display knowledge.

There is no speech or language

where their voice is not heard.

Their voice goes out into all the earth.

their words to the ends of the world.

Psalm 19:1-4

TABLE OF CONTENTS

CHAPTER 1	GENERAL INTRODUCTION	1
1.	Welcome to the middle atmosphere	1
2.	Remote sensing of atmospheric temperature and constituents	6
3.	Upper Atmosphere Research Satellite	9
4.	Microwave Limb Sounder	10
5.	Improved Stratospheric and Mesospheric Sounder	12
6.	The 4-day wave	13
7.	ISAMS CO observations in the middle atmosphere	14
8.	Explanation of dissertation format	16
CHAPTER 2	THE 4-DAY WAVE AS OBSERVED FROM THE UPPER ATMOSPHERE RESEARCH SATELLITE MICROWAVE LIMB SOUNDER	17
	Abstract	17
1.	Introduction	18
2.	Microwave Limb Sounder data	20
	a. The MLS instrument	20
	b. Temperature data	20
	c. Ozone data	20
	d. Geopotential height data	21
3.	Analysis procedure	21
4.	Results	24
	a. Temperature	24
	b. Geopotential	29

c. Ozone	32
d. Uncertainty in 4-day wave amplitude	35
e. Statistical assessments	36
f. Zonal wind, \bar{q}_y and EP flux structure	37
g. Quasigeostrophic potential vorticity	42
5. Summary	46
Acknowledgements	47
CHAPTER 3 OBSERVATIONS OF MIDDLE ATMOSPHERE CO FROM THE UARS ISAMS DURING THE EARLY NORTHERN WINTER 1991/1992	48
Abstract	48
1. Introduction	49
2. Data description	52
3. Model description	56
4. Analysis techniques: PV-mapping and MLM diagnostics	58
5. Results	60
a. Meridional structure	60
b. Evidence of CH ₄ oxidation in the upper stratosphere	62
c. Merger of two anticyclones and strong warming from 1–16 January 1992	67
d. Comparison of ISAMS and CTM CO	73
e. MLM diagnostics of vortex merger	80
6. Conclusions	86
Acknowledgements	87
Appendix: Proof that equivalent length is the same for all species in contour equilibrium	87
CHAPTER 4 GENERAL CONCLUSIONS	89
The 4-day wave	89
Observations of middle atmosphere CO	90
APPENDIX: GLOSSARY	93

REFERENCES	101
ACKNOWLEDGMENTS	108

ABSTRACT

This study uses data from the Upper Atmosphere Research Satellite (UARS) to investigate two topics in middle atmosphere dynamics: the “4-day wave” and transport processes deduced from atmospheric carbon monoxide. The 4-day wave is an eastward moving quasi-nondispersive feature with 4 day period occurring near the winter polar stratopause. Evidence of the 4-day feature is presented in UARS Microwave Limb Sounder (MLS) temperature, geopotential height, quasigeostrophic potential vorticity (PV), and ozone from the late southern winters of 1992 and 1993. Space-time spectral analyses reveal a double-peaked vertical temperature structure with an out-of-phase relationship between the two peaks. The height variation of the 4-day ozone signal compares well with a linear advective-photochemical tracer model. Regions of negative PV gradient and positive Eliassen-Palm flux divergence are shown to occur, consistent with instability dynamics playing a role in wave forcing. The three-dimensional wave structure resembles the PV “charge” concept, wherein a PV anomaly in the atmosphere (analogous to an electrical charge in a dielectric material) induces a geopotential field, a vertically oriented temperature dipole, and circulation about the vertical axis.

Observations of carbon monoxide in the upper stratosphere and lower mesosphere from the UARS Improved Stratospheric and Mesospheric Sounder (ISAMS) are presented during the early northern winter 1991/1992. High CO mixing ratios are found to saturate the polar vortex. 2D analyses in the meridional plane indicate: (1) Increasing mixing ratio with altitude. (2) Large mixing ratios near the Arctic winter pole due to downward advection from the diabatic circulation. (3) A tropical upper stratosphere maximum likely due largely to methane oxidation. ISAMS CO data are compared with CO output from a 3D chemistry and transport model (CTM), initialized with ISAMS CO. ISAMS and CTM horizontal distributions compare

favorably near the stratopause, while disagreement in the vertical zonal mean CO distributions occurs several weeks into the model run, with CTM mixing ratios biased high in the upper stratosphere outside the polar vortex and low in the stratospheric vortex and lower mesosphere. Novel modified Lagrangian mean diagnostics applied to ISAMS and CTM data provide insight into horizontal mixing processes during a rapid merger of two anticyclones.

CHAPTER 1 GENERAL INTRODUCTION

Significant changes in the earth's global atmosphere over the last several decades have prompted extensive study of the chemical, dynamical, and radiative processes which govern atmospheric behavior. With the advent of earth-orbiting satellites and remarkable remote sensing techniques our ability to observe the atmosphere, especially its upper portions, has increased exponentially. The amount of data on the meteorological state and chemical composition of the atmosphere available to the general public via internet transfer is enormous: as one atmospheric scientist described, "It's like drinking water from a fire hydrant." This study involves the analyses of dynamical processes in the middle atmosphere (defined below) as observed from two instruments on board the Upper Atmosphere Research Satellite (UARS), launched in September 1991.

This general introduction first provides a definition and cursory overview of the middle atmosphere. Following is a brief discussion of the concept of remote sensing applied to the earth's atmosphere, along with descriptions of the UARS satellite and two remote sensing instruments from which data used in this study were taken. Finally, an introduction is provided for the two topics addressed in this dissertation, analyses of the 4-day wave in the upper stratosphere and lower mesosphere and observations of middle atmosphere carbon monoxide, followed by an explanation of the dissertation format.

1. Welcome to the middle atmosphere

The atmosphere is conventionally partitioned into vertical layers based on the climatological temperature profile (see Fig. 1.1). In the troposphere (roughly 0–10 km), where humans spend the majority of their time, the temperature generally decreases with height and significant

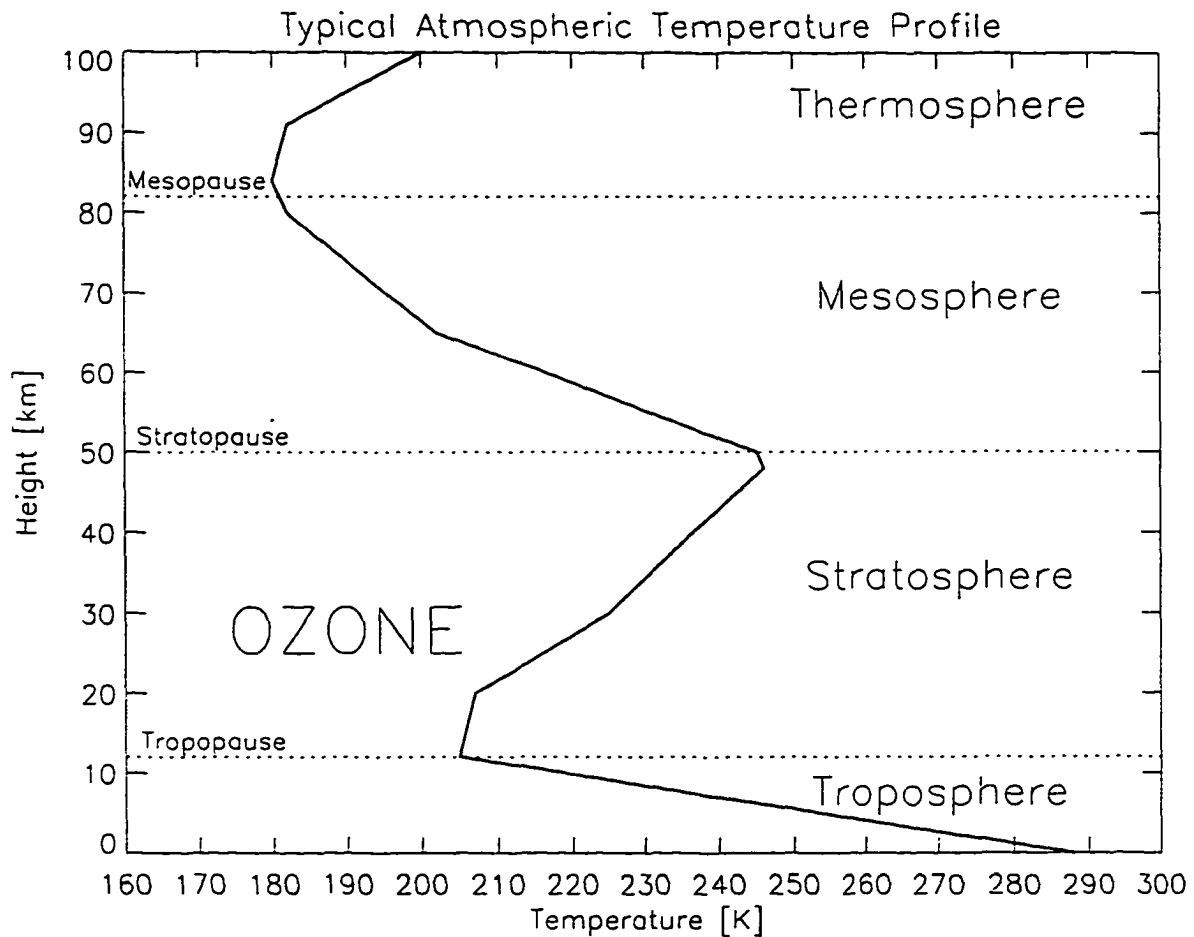


Figure 1.1 A typical midlatitude temperature profile.

mixing of air occurs in both the horizontal and vertical directions due to ubiquitous turbulent eddy motions. From 10–50 km, defined as the stratosphere, the temperature increases with height due to the presence of gaseous ozone (O_3) which absorbs solar ultraviolet (uv) radiation, providing a heat source in the stratosphere. Although ozone mixing ratio averages only about 5 parts per million by volume (ppmv), it plays a key role in protecting the biosphere from harmful uv-b radiation. Due to the positive vertical temperature gradient the stratosphere is resistant to vertical motions, so that vertical mixing and transport processes are small. Horizontal transport and mixing, however, can occur quite rapidly, as will be seen in chapter 3.

From about 50 to 80 km the mesosphere is a region of decreasing temperature with height.

while in the thermosphere (above 80 km) high energy solar radiation ionizes molecules, producing very large kinetic temperatures (up to 2000° K). Separating these regions are layers where the sign of the vertical gradient reverses, called the tropopause, stratopause, and mesopause: these serve as upper boundaries to the troposphere, stratosphere, and mesosphere, respectively. The middle atmosphere is defined roughly as the layer from 10 to 100 km, containing the stratosphere, mesosphere, and lower thermosphere. It is important to note that these definitions are a rough guide and should not be viewed rigidly. The atmosphere is in constant fluid dynamical motion, so that defining the tropopause, for example, at a given instant and location may be difficult or even impossible.

The global temperature structure varies significantly with latitude and season, as seen in Fig. 1.2a, which presents the zonal mean temperature for 1 January 1992 (near solstice) from the Goddard Space Flight Center Data Assimilation Office (DAO) meteorological assimilation. [Note: six months later the temperature would be roughly a mirror image of Fig. 1.2a]. An interesting feature is the cold summer mesopause (~ 80 km in the Southern Hemisphere). Although the solar radiation is strongest at solstice in the high summer latitudes, the coldest temperatures observed in the atmosphere occur near the summer polar mesopause. This anomaly is thought to be due to the wave-driven meridional circulation characterized by rising motions in the summer middle atmosphere (which produce subsequent cooling), transport to the winter hemisphere, and sinking in the winter polar latitudes (Andrews et al. 1987). The cold tropical tropopause (near 15 km) is related to the so-called Brewer-Dobson circulation which transports tropical tropospheric air upward into the stratosphere.

The average global zonal mean wind structure is provided in Fig. 1.2b, also from DAO assimilation on 1 January 1992. The midlatitude tropospheric westerly maxima near 300 hPa are the well-known jet streams, which play a crucial role in the propagation of weather patterns. The middle atmosphere similarly contains two wind maxima, a westerly jet in winter and an easterly jet in summer, both maximizing at over 60 ms^{-1} . A key feature in this dissertation is the winter jet, which forms the so-called polar vortex, a region of roughly circumpolar winds, which increase in magnitude away from the pole to a maximum identified as the vortex “edge.”

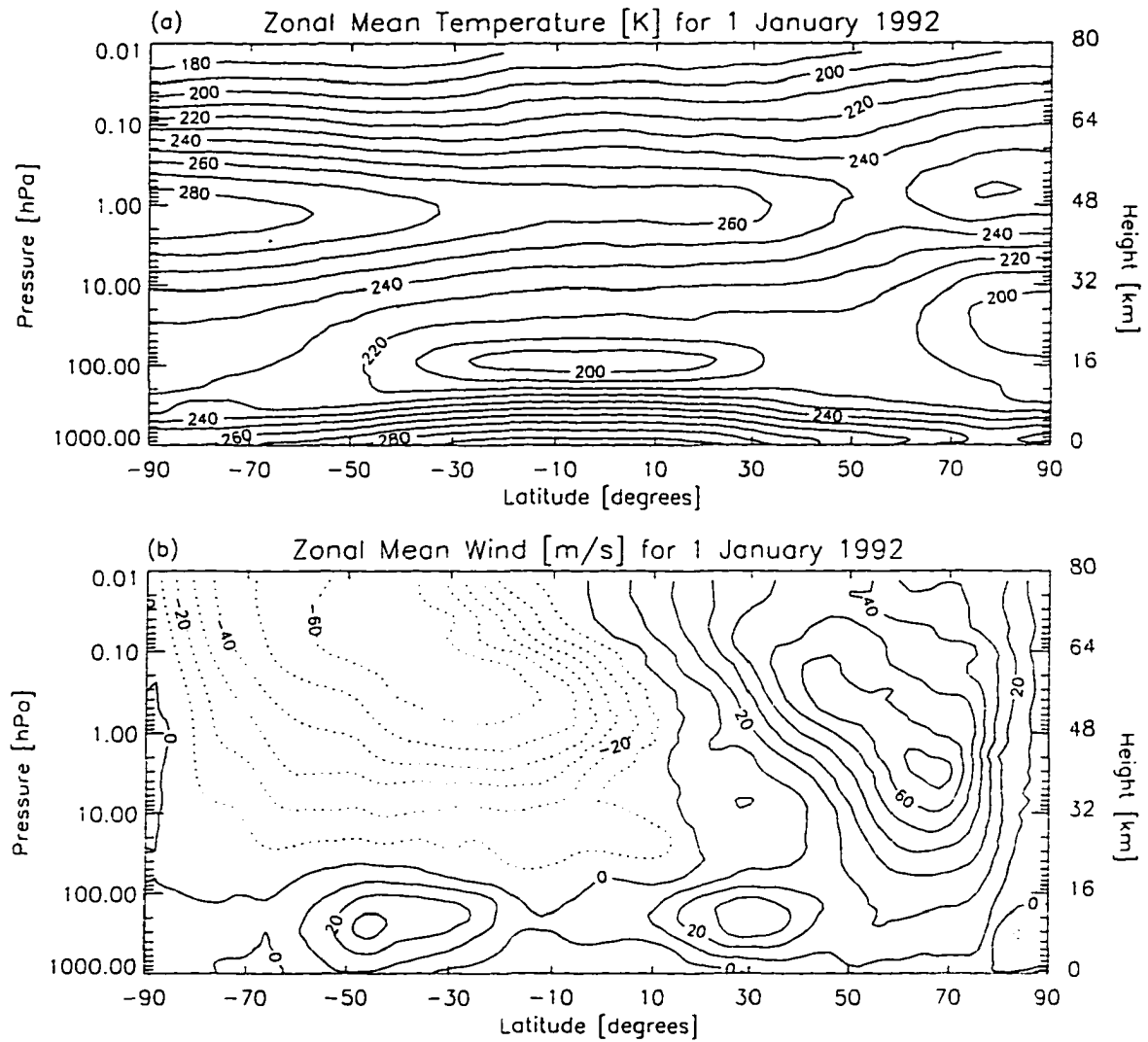


Figure 1.2 (a) Zonal mean temperature for 1 January 1992 from the Goddard Space Flight Center Data Assimilation Office (DAO) meteorological assimilation. (b) Zonal mean zonal winds for 1 January 1992 from the DAO assimilation.

occurring roughly at 60° in either hemisphere. Due to weak horizontal mixing across the edge, the vortex acts like a containment vessel, allowing a given volume of air to remain localized for periods of a month or more. The presence of a strong southern vortex is a key dynamical component involved in the development of an ozone “hole” over Antarctica during the austral spring.

The middle atmosphere is also known to support a wide variety of wave features. Properties of these features observed in atmospheric constituents and meteorological quantities can be deduced by solving the equations of motion under varying conditions. Since this study deals mainly with planetary-scale atmospheric features (on the order of thousands of km) we are mostly concerned with Rossby (or planetary) waves. The restoring mechanism for Rossby waves involves the variation with latitude of the earth’s rotation vector projected on the normal to the planetary surface. These waves propagate westward with respect to the flow of the zonal wind and have periods of several days, horizontal wavelengths from hundreds of km up to as large as zonal wavenumber 1 (in which one wavelength extends completely around a latitude circle), and vertical wavelengths of order 10 km. Rossby waves can be produced by instability mechanisms within the middle atmosphere or may propagate up from the troposphere, usually in the winter, when conditions are favorable for vertical propagation of planetary-scale waves.

Although the middle atmosphere contains only about 20% of the total atmospheric mass, it plays an important role in the delicate radiative balance necessary for global habitability. In order completely understand the complex physical and chemical mechanisms involved in that balance, comprehensive studies are needed to assess the current situation and predict atmospheric behavior in the future. Although the impact of changes in composition and structure on the welfare of mankind is important (and provides essential motivation for research funding), I as a middle atmosphere dynamicist, strive first and foremost to understand the intricate and beautiful dynamical processes that govern this region and perceive this goal to be an end in itself.

2. Remote sensing of atmospheric temperature and constituents

The history of quantitative observation of the temperature and composition of the earth's atmosphere is very rich, beginning with Galileo's invention of the thermometer and culminating in the high technology satellites of today. The earliest middle atmosphere measurements were made by large balloons which carried meteorological instruments high into the atmosphere. Balloons were followed by ground-based remote sensing instruments, stratospheric jets, and rockets, that allowed greater range to the observations. These methods are useful, but the need soon became evident for a device that could continuously monitor large portions of the atmosphere for long time periods. The advanced rocket technology led to the development of earth-orbiting satellites which were able to provide the platform for the extensive observations needed, while advanced remote sensing technology provided the instrumentation. In order to understand how satellites remotely measure atmospheric temperature and composition, one must begin with the field of radiative transfer: this section provides a brief discussion of radiative transfer as applied to remote sensing of atmospheric temperature and constituents.

Radiative transfer is the process by which radiation from various sources propagates through space. In the atmosphere, radiation is emitted by each gaseous constituent in a diverse spectrum which depends on the molecular composition, temperature, and pressure. Each constituent similarly absorbs radiation from the sun, stars, earth, or other molecules according to its characteristic absorption spectrum. To form a mathematical construction of this complicated process we use the simple case of vertical radiative transfer in one dimension to a satellite outside the atmosphere (also called nadir viewing).

The radiation absorbed in this case by a layer of thickness dz is:

$$dI_\nu = -k_\nu I_\nu \rho dz \quad (1.1)$$

where k_ν is the absorption coefficient, which is a function of ν , the frequency of the electromagnetic radiation, ρ is the density of the given absorber, and I_ν is the incident radiation on the layer. To find the radiation absorbed in a layer from z_1 to z_2 , simply integrate Eq.(1.1).

$$I_\nu(z_2) = I_\nu(z_1) \exp\left(-\int_{z_1}^{z_2} k_\nu \rho dz\right) = I_\nu(z_1) \tau_\nu(z_1, z_2) \quad (1.2)$$

where τ is the fraction of radiation transmitted from z_1 to z_2 (note: $0 \leq \tau \leq 1$).

The slab dz will also radiate energy according to the characteristic spectrum of the gas under consideration. If, however, thermodynamic equilibrium conditions exist (a good approximation for many transitions in certain regions of the atmosphere) then the radiation is given by the Planck function, $B_\nu(T)$, which depends only on temperature. Since temperature depends on height, we can write the incremental emission $dI_\nu = B_\nu(z)d\tau$, so the integral radiative transfer equation for absorption and blackbody emission over a layer from z_1 to z_2 is given by

$$I_\nu(z_2) = I_\nu(z_1)\tau(z_1, z_2) + \int_{\tau(z_1, z_2)}^1 B_\nu(z)d\tau_\nu(z, z_2). \quad (1.3)$$

Extending the layer to encompass the entire atmosphere ($z_1 = 0, z_2 = \infty$) and assuming that the incident radiation at $z = 0$ is due to the earth's blackbody radiation at surface temperature T_s [i.e., $I_\nu(0) = B_\nu(T_s)$], we can write:

$$I(\infty) = B_\nu(T_s)\tau_\nu(0, \infty) + \int_0^\infty B_\nu(T(z)) \frac{d\tau_\nu(z, \infty)}{dz} dz. \quad (1.4)$$

Here we reformulated the integral term to introduce the quantity $d\tau_\nu/dz$, called the weighting function, which gives the fractional contribution of different levels of the atmosphere to the total radiance measured at a given frequency, ν . For well-behaved weighting functions the location of the maximum indicates the altitude from which most of the radiation at that frequency originates. By varying the measured frequency one can vary the shape of the weighting function, thereby obtaining information about the vertical atmospheric structure. Figure 1.3 gives an example of weighting functions for the very simple case of an isothermal atmosphere with a constituent of constant mixing ratio and absorption coefficient k_ν that is independent of height. Weighting functions for three values of k_ν are provided, showing that the altitude of the weighting function maximum increases with k for this simple case.

To retrieve the atmospheric temperature we solve Eq.(1.4) for a constituent such as CO_2 , which is nearly uniformly mixed throughout much of the atmosphere, so that the density of CO_2 is assumed to be "known." Information on the absorption coefficient k_ν can be obtained from laboratory measurements and theoretical considerations. The surface temperature can be taken from meteorological observations [in some cases, the transmission from the surface to

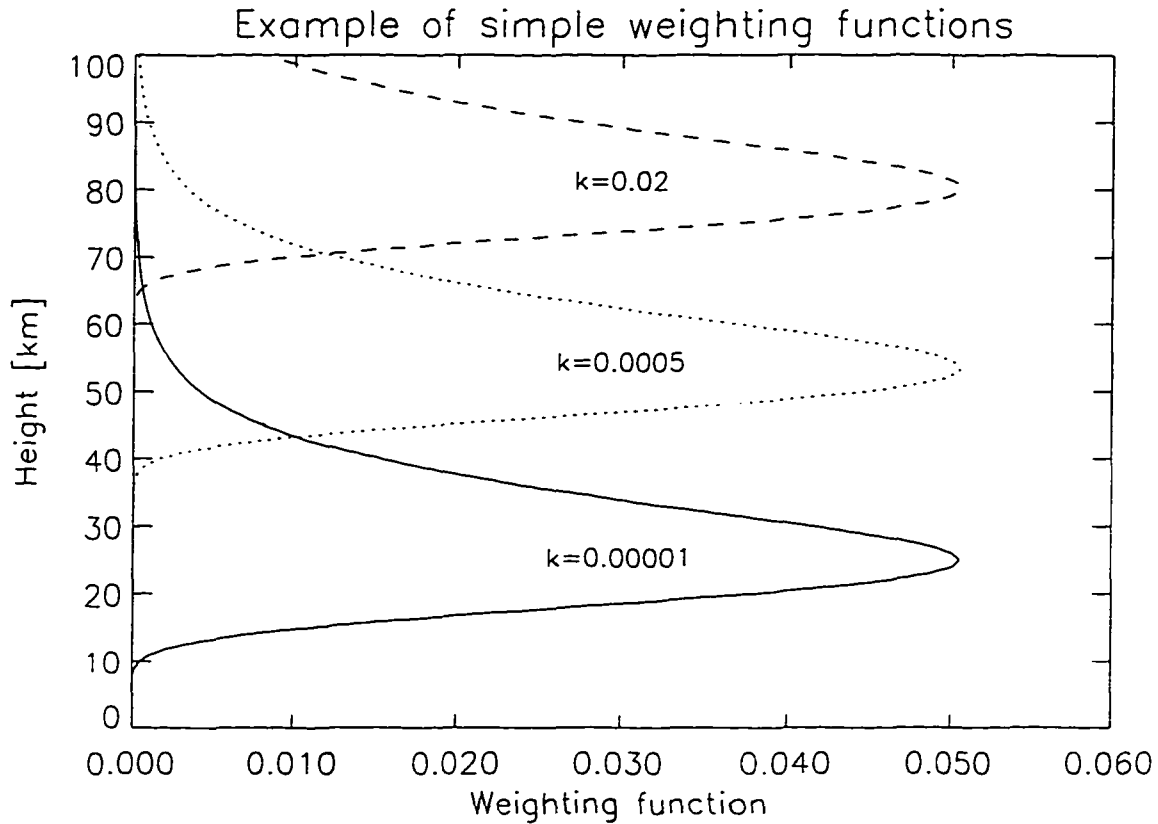


Figure 1.3 Weighting functions for an isothermal atmosphere with temperature 240° K for a gas with constant mixing ratio of 300 ppmv. Three weighting functions are given for three values of the absorption coefficient k which is constant with height.

outer space is very small, so the first term on the right side of Eq.(1.4) can be neglected.] Since the Planck function is known, and measurements of $I(\infty)$ are taken from the satellite, the only unknown in Eq.(1.4) is $T(z)$. The process of obtaining $T(z)$ from satellite measurements, called the “retrieval,” is not simple, since the basic problem is ill-conditioned (i.e., a limited number of measurements used to obtain a continuous profile). Using various techniques, scientists are able to solve the retrieval problem reliably, and useful temperature information can be obtained (Rodgers 1976). To retrieve a constituent mixing ratio, such as O_3 , the retrieved temperature is inserted for $T(z)$ in Eq.(1.4), which is then solved for the unknown quantity ρ_{O_3} .

The process when applied to the real atmosphere is much more complicated than that described here. Those who do retrievals must deal with numerous complications: scattering of radiation, inaccuracy of absorption coefficients, breakdown of thermodynamic equilibrium,

line-broadening by pressure and Doppler effects, and overlapping of absorption lines, to name a few. Since many atmospheric scientists use the “well-polished” processed data, the retrieval method may seem somewhat like a “black box,” but it is important to appreciate the work required to obtain useful physical quantities from the raw radiance measurements. Although the retrieved data from UARS also undergo significant validation by various methods before distribution to the general public, it is important to keep close contact with the instrument teams, since incremental processing versions (ISAMS is currently at version 12) may contain significant variations that must be understood in order to do accurate data analyses.

3. Upper Atmosphere Research Satellite

The Upper Atmosphere Research Satellite (UARS) was launched on the Space Shuttle Discovery in September 1991 with a mission to provide a comprehensive global data base of various atmospheric constituents and parameters to assist scientists in studying the photochemistry, radiation, and dynamics of the middle (10 to 100 km) and upper (above 100 km) atmosphere. UARS carries ten instruments, strategically placed on a multi-modular spacecraft, which contains the devices for recording and relaying data to the earth, a power supply, and steering components.

The UARS orbits the earth with a 57° inclination to the equator. Unlike most polar-orbiting satellites (90° inclination), the local solar time at which UARS passes a given latitude drifts slightly with each orbit, making a complete diurnal cycle every 72 days. Since several of the UARS instruments can be damaged by direct solar radiation the satellite makes a 180° yaw every 36 days to keep those instruments on the dark side of the satellite. Several of the UARS instruments use limb-sounding geometry to view thermal emission from the atmospheric limb (Fig. 1.4). Limb-sounding has two distinct advantages over the nadir view (discussed in the previous section). First, the optical path of the limb view is about 70 times greater, allowing measurements of species with smaller concentrations. Second, limb-sounding allows better vertical resolution, although what is gained in the vertical is somewhat lost in the horizontal. The distance from the UARS orbit path to the limb path is 23° great circle, thus with a 57°

UARS Limb-Sounding Geometry

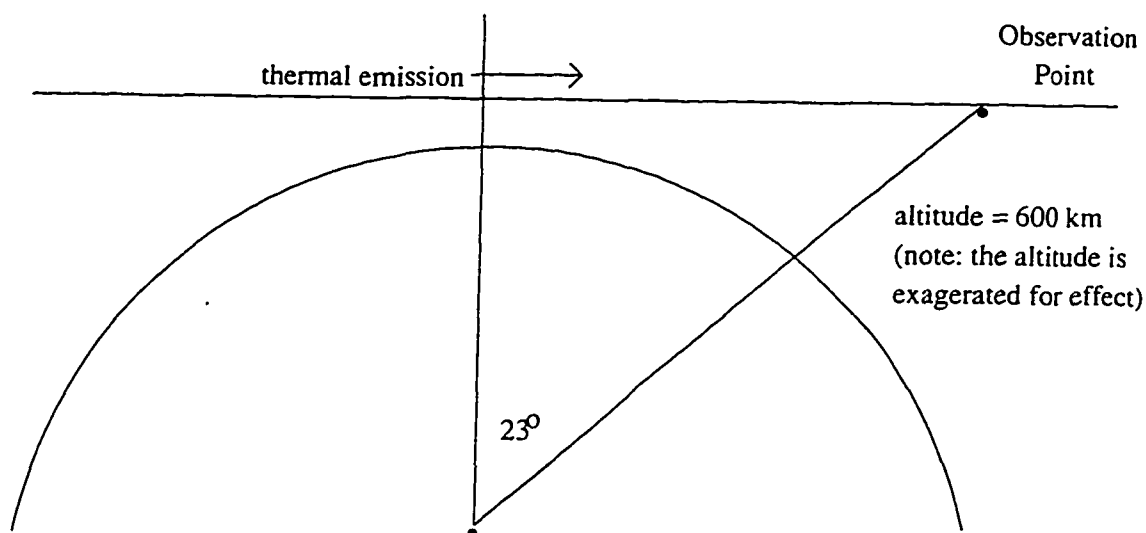


Figure 1.4 Schematic of the limb-sounding geometry used by the MLS and ISAMS instruments on UARS. Note that if this picture was to scale the orbit altitude and limb tangent points would be much closer to the earth's surface.

orbit inclination coverage is allowed from 80° in one hemisphere to 34° in the other. Figure 1.5 shows the tangent point scan path covered by a typical UARS instrument in one day. The satellite altitude is 600 km with an orbital period of 97 minutes (about 15 orbits per day). The spatial limitations of the orbit allow zonal resolution of wavenumbers 1 through 7 and temporal resolution of periods from 0.96 to 36.1 days.

4. Microwave Limb Sounder

Chapter 2 of this thesis involves analyses of data from the Microwave Limb Sounder (MLS), one of the ten UARS instruments. MLS takes advantage of recent improvements in microwave sensitivity and ease of instrument fabrication to provide the first satellite measurements using limb-sounding techniques in the microwave region. MLS measures thermal emission at 63, 183, and 205 GHz as the instrument field-of-view is scanned vertically through the atmospheric limb (Barath et al. 1993). This allows the determination of chlorine monoxide, ozone, nitric acid,

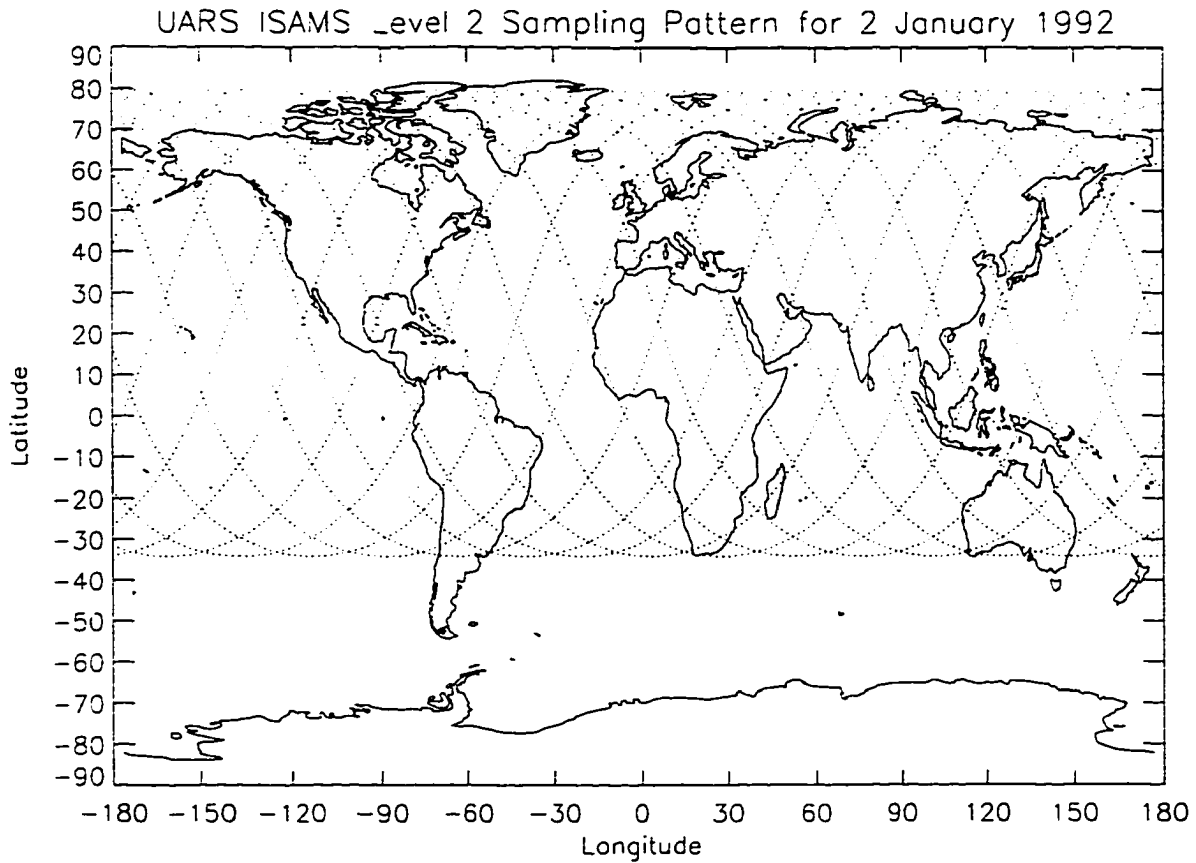


Figure 1.5 The spatial location of all UARS level 2 measurement points for 2 January 1992.

sulfur dioxide, temperature, geopotential height, water vapor, and cirrus ice during both day and night and in the presence of stratospheric clouds and aerosols.

The MLS limb scan ranges from 5 to 95 km in discrete steps every 65 seconds. With the improved microwave technology, the spectral resolution can be made arbitrarily fine, so the only actual limitation, besides measurement integration time, is the overlapping of spectral lines. With an integration time of 1.8 seconds, MLS measures at roughly 1 km intervals in the lower stratosphere to 5 km in the mesosphere, with average vertical resolution of 2–3 km. At the end of a 65 second scan, the instrument is re-calibrated with an accuracy of roughly 3% by looking into empty space and an on-board blackbody target. The UARS satellite travels 4° in latitude every minute, thus slightly blurring the measurements, while the horizontal line-of-sight resolution is ~ 300 – 400 km. MLS has provided nearly continuous coverage of the middle

atmosphere from the satellite launch (September 1991) through the present (June 1997) and shows no signs of failure in the near future, although observations are currently limited due to a slow decline in available satellite power.

5. Improved Stratospheric and Mesospheric Sounder

The Improved Stratospheric and Mesospheric Sounder (ISAMS) was developed mainly at Oxford University, which has pioneered many advances in the field of remote sensing beginning with Gordon Dobson's invention of the Dobson Ozone Spectrometer in the 1930s. The ISAMS instrument is a product of years of research on a novel sensing technique called Pressure Modulator Radiometry (PMR), see Taylor et al. (1993). A brief discussion of this useful technique is provided here before discussing specifics of the ISAMS instrument.

Pressure modulator radiometry is an advanced version of the Selective Chopper Radiometry (SCR) technique. In SCR instruments, atmospheric radiation received at the satellite is reflected by a mirror either through an empty cell or a cell containing the gas being measured (e.g. CO₂). The signal measured by the detector is the difference between the signal which passes through the empty cell and the signal which passes through the gas chamber. Since the CO₂ in the cell will absorb some of the emission from CO₂ in the atmospheric limb, the difference between the two signals is solely due to CO₂. This technique is especially useful to discriminate between closely spaced or overlapping emission lines. There are two major problems associated with SCR. First, a precise optical balance must be maintained in flight between the two cells so that the resulting "difference" signal is due only to CO₂. Second, it is absolutely necessary to know precisely the pressure of CO₂ in the cell; this is extremely difficult to calibrate remotely.

PMR solves the first problem by using only one cell containing the gas in question rather than two; the cell is fitted with an oscillating piston which changes the cell's gas pressure. The restoring force on the piston from the compressed gas will be a minimum when the piston is oscillating at a resonant frequency, which is determined solely by the pressure. This allows the pressure to be monitored precisely, thus eliminating the second major problem with the SCR

technique. Since the amount of absorption by the cell depends on the CO_2 density, varying the pressure will produce different signals at the detector for the CO_2 lines in question, and the difference between the signals can be used to retrieve the atmospheric CO_2 abundance.

The ISAMS instrument uses the PMR technique to measure thermal infrared emission from the atmospheric limb to obtain the following quantities: O_3 , H_2O , N_2O , NO , NO_2 , HNO_3 , CH_4 , N_2O_5 , CO , temperature, and certain aerosols. The instrument measures with a vertical spacing of ~ 2.4 km and a horizontal sampling of ~ 200 km along the tangent track, twice the sampling rate of MLS. The horizontal resolution due to the weighting function is about 4° latitude (~ 400 km) along the line of sight. The ISAMS scan partially corrects for the horizontal velocity of the satellite, so that the limb-track resolution is only ~ 18 km. ISAMS has the unique ability to switch from either northward or southward viewing to allow global coverage (80° N to 80° S) on any given day. Problems with the instrument's chopper caused the termination of ISAMS measurements on 29 July 1992. In total, 180 days of ISAMS data are available in the period between 26 September 1991 to 29 July 1992.

6. The 4-day wave

Chapter 2 examines the 4-day wave as observed from the UARS MLS (Allen et al. 1997). A review of previous studies is included in that chapter, so here we introduce only the salient points. The 4-day wave, which is ubiquitous in the polar winter upper stratosphere, is observed in synoptic maps as a warm pool of air several thousands of km across that rotates eastward around the winter pole with a four day rotation period. The wave is forced by barotropic and/or baroclinic instability processes associated with the jet structure in the stratosphere and mesosphere. The wave has been observed in temperature and geopotential height and is expected (according to 3D model results) to have a double-lobed structure in the perturbation temperature field with one lobe in the upper stratosphere and another in the lower mesosphere.

The current work provides the first (other than an unpublished conference report) conclusive evidence of the 4-day wave in a constituent (ozone), although since the publication of chapter 2 the feature has also been identified in MLS water vapor (Dr. Gloria Manney, per-

sonal communication). This study was also the first to observe the double-lobed temperature structure with rapid vertical phase variations between the lobes predicted from a 3D model (Manney and Randel 1993). The 4-day feature is also shown to exist in quasigeostrophic potential vorticity (PV) derived from MLS geopotential heights. An elegant and conceptually satisfying paradigm for the 4-day wave is presented by using the potential vorticity “charge” concept (Hoskins et al. 1985; Bishop and Thorpe 1994), wherein a PV anomaly in the atmosphere acts like an electrical charge in a dielectric material, with an associated vector field. The PV field induces temperature, geopotential, and wind anomalies with structure similar to the 4-day wave observations in MLS data. The PV charge paradigm, coupled with its generation by instability mechanisms, provides a novel physical explanation for the 4-day wave.

7. ISAMS CO observations in the middle atmosphere

Although carbon monoxide plays an important role in tropospheric chemistry, especially with respect to ozone and urban pollution, it has only a minor role in the chemistry of the middle atmosphere. However, since CO is rather unreactive in the stratosphere and mesosphere (especially in the winter polar region) it can often be used as a tracer of the atmospheric motion. Chapter 3 uses CO observed from the UARS ISAMS to examine transport processes in the early northern winter 1991/92. The introduction in chapter 3 details previous studies of CO in the middle atmosphere, while here we elaborate on the general concept of deducing atmospheric motions from tracer transport, a concept essential to the study.

An atmospheric tracer is a quantity used to label a given fluid parcel. This may be the mixing ratio of a given molecule or a derived meteorological quantity such as potential temperature or potential vorticity. In order for a quantity to be used as a tracer it must exhibit sufficient spatial variability. CO₂, for example, has a nearly constant mixing ratio throughout the middle atmosphere, and therefore assigning that value as a tracer of all fluid parcels in the middle atmosphere would be useless. Other molecules such as CO, N₂O, CH₄, and O₃, which have middle atmospheric sources and/or sinks, maintain sufficient gradients to be considered as tracers.

The equation regulating tracer transport for chemical constituents is the continuity equation:

$$\frac{D\chi}{Dt} = S, \quad \frac{D(\)}{Dt} = \frac{\partial(\)}{\partial t} + \mathbf{V} \cdot \nabla(\). \quad (1.5)$$

where χ is the constituent mixing ratio, $D(\)/Dt$ is the derivative following an air parcel advected by the 3D wind \mathbf{V} , and S is the net source term. If the net source is negligible (i.e., the tracer is “long-lived”), and if the time scale is short enough that microscale diffusion is small, then a given parcel of air will maintain the same mixing ratio. By examining the time evolution of long-lived constituents one can obtain information about dynamical process in the atmosphere. Chapter 3 uses CO as a tracer of northern winter polar vortex evolution in the upper stratosphere and lower mesosphere.

The other tracer used in this study is potential vorticity (PV). PV in Ertel’s form (see Appendix for complete derivation) is derived from the equations of motion by first taking the curl of the momentum equation (Newton’s second law applied to fluid motions in the earth’s reference frame) to get the vorticity equation. Then take the scalar product of the vorticity equation with the gradient of potential temperature to obtain an equation for Ertel’s potential vorticity, $Q = \rho^{-1} \zeta_a \cdot \nabla \theta$. For adiabatic, frictionless motion, with θ as the vertical coordinate, the potential vorticity equation becomes

$$\frac{D_\theta(Q)}{Dt} = 0, \quad (1.6)$$

so the potential vorticity is conserved following isentropic air motion. Potential vorticity is commonly used to study middle atmosphere transport, especially in the context of the polar vortex. Chapter 3 compares the temporal evolution of PV with CO to examine the Arctic polar vortex during the early northern winter 1991/1992. CO is also mapped using PV as a quasi-meridional coordinate. This technique is quite useful, especially when the atmospheric structure deviates significantly from a zonally uniform state.

8. Explanation of dissertation format

This dissertation follows the alternate format, in which two papers are included that have been (or will soon be) submitted to scholarly journals. The candidate had primary responsibility for both papers. Chapter 2 was published in the 1 March 1997 issue of the *Journal of the Atmospheric Sciences*, and chapter 3 will soon be submitted to the *Journal of Geophysical Research-Atmospheres*. The style required by the *Journal of the Atmospheric Sciences* has been followed in both sections. General conclusions are provided in chapter 4 followed by a glossary of important terms and complete list of cited references.

CHAPTER 2 THE 4-DAY WAVE AS OBSERVED FROM THE UPPER ATMOSPHERE RESEARCH SATELLITE MICROWAVE LIMB SOUNDER

A paper published in the *Journal of the Atmospheric Sciences*¹,
a publication of the American Meteorological Society.

D. R. Allen², J. L. Stanford², L. S. Elson³, E. F. Fishbein³,
L. Froidevaux³, and J. W. Waters³

Abstract

The “4-day wave” is an eastward moving quasi-nondispersive feature with period near 4 days occurring near the winter polar stratopause. This paper presents evidence of the 4-day feature in Microwave Limb Sounder (MLS) temperature, geopotential height, and ozone data from the late southern winters of 1992 and 1993. Space-time spectral analyses reveal a double-peaked temperature structure consisting of one peak near the stratopause and another in the lower mesosphere, with an out-of-phase relationship between the two peaks. This double-peaked structure is reminiscent of recent three-dimensional barotropic/baroclinic instability model predictions and is observed here for the first time. The height variation of the 4-day ozone signal is shown to compare well with a linear advective-photochemical tracer model. Negative regions of quasigeostrophic potential vorticity (PV) gradient and positive Eliassen-Palm flux divergence are shown to occur, consistent with instability dynamics playing a role in wave forcing. Spectral analyses of PV derived from MLS geopotential height fields reveal a 4-day signal peaking near the polar stratopause. The three-dimensional structure of the

¹Reprinted with permission from *J. of the Atmospheric Sciences*, 1997, **54**, 420–434.

²Department of Physics and Astronomy, Iowa State University, Ames, Iowa

³Jet Propulsion Laboratory/California Institute of Technology, Pasadena, California

4-day wave resembles the potential vorticity “charge” concept, wherein a PV anomaly in the atmosphere (analogous to an electrical charge in a dielectric material) induces a geopotential field, a vertically oriented temperature dipole, and circulation about the vertical axis.

1. Introduction

The 4-day wave is a ubiquitous feature in the polar winter upper stratosphere. It was first observed in temperature data as a strong 4-day signal in zonal wavenumber 1 (Venne and Stanford 1979). Later studies showed that it consists of waves 1 through at least 4 all moving with the same phase speed, such that the period of wave 1 is near 4 days. Synoptic plots of temperature reveal a quasi-nondispersive “warm pool” of air, which rotates eastward around the winter pole near the stratopause with a 4-day rotation period (Prata 1984; Lait and Stanford 1988b; Lawrence et al. 1995). Numerous observational (Venne and Stanford 1979, 1982; Prata 1984; Lait and Stanford 1988b; Randel and Lait 1991; Manney 1991; Fraser et al. 1993; Lawrence et al. 1995; Lawrence and Randel 1996) and theoretical (Hartmann 1983; Manney et al. 1988; Manney 1991; Manney and Randel 1993; Bowman and Chen 1994; Orsolini and Simon 1995) studies have examined the 4-day phenomenon.

The wave has been observed in both hemispheres but is stronger in the Southern Hemisphere (Venne and Stanford 1982). The horizontal phase structure is variable, with both poleward and equatorward momentum flux events (Venne and Stanford 1982; Prata 1984; Manney 1991). The wave is generally barotropic, although some episodes show strong equatorward heat flux (Randel and Lait 1991). The episodes studied by Randel and Lait (1991) and Lawrence and Randel (1996) reveal a dipole structure of positive and negative Eliassen–Palm flux divergence associated with the 4-day wave, with the positive region overlapping negative quasigeostrophic potential vorticity gradient, a signature of instability processes.

Theoretical studies have focused on instability of the jet structure as the mechanism for 4-day wave growth. Hartmann (1983) and Manney et al. (1988) showed that periods of 4-day wave growth are consistent with barotropic instability of the stratospheric polar night jet. Manney and Randel (1993) used a 3D instability model to show that realistic 4-day

wave growth rates exist in monthly mean background wind states only if both barotropic and baroclinic components are included. Their model also predicted a double-lobed structure in the perturbation temperature field with one lobe in the upper stratosphere and another in the lower mesosphere, with rapid phase variation in between. Further insight into the lifecycles and mixing processes of barotropically unstable waves in the middle atmosphere has been gained by several recent studies using nonlinear barotropic models (Ishioka and Yoden 1994; Bowman and Chen 1994; Orsolini and Simon 1995).

The present paper takes advantage of the coverage and vertical resolution of the Microwave Limb Sounder (MLS) on board the *Upper Atmosphere Research Satellite (UARS)* to examine the 4-day wave during the late austral winters of 1992 and 1993. As will be shown below, strong 4-day signals exist in MLS temperature, geopotential height, and ozone. The vertical coverage provided by MLS allows resolution of a double-peaked structure in perturbation temperature with an out-of-phase relationship between the upper and lower peaks, as predicted by Manney and Randel (1993). Spectral analyses of MLS ozone reveal a 4-day signal in zonal wavenumber 1 near the polar stratopause. A linear advective-photochemical model is used to calculate the ozone response to temperature and wind perturbations associated with the 4-day wave. The vertical variation of model ozone amplitude and phase is in good agreement with observations of MLS ozone. Negative regions of quasigeostrophic potential vorticity (PV) gradient and positive Eliassen-Palm flux divergence are shown to occur, consistent with wave forcing by instability dynamics.

The 4-day feature is also shown to exist in quasigeostrophic PV derived from MLS geopotential heights. The three-dimensional structure of this signal resembles the PV “charge” discussed by Hoskins et al. (1985) and more recently by Bishop and Thorpe (1994). The latter authors have also extended the concept to Ertel PV (Thorpe and Bishop 1995), although the present paper focuses on quasigeostrophic PV. In this electrostatics analogy, a PV anomaly in the atmosphere acts like an electrical charge in a dielectric material, with an associated vector field (independent of static stability, density, and boundary conditions) that produces “action-at-a-distance.” Isolated PV charges induce geopotential anomalies, circulation about

the vertical axis, and a vertically oriented temperature dipole, similar to observations of the 4-day wave presented in this study.

2. Microwave Limb Sounder data

a. The MLS instrument

The Microwave Limb Sounder is 1 of 10 instruments on board the *Upper Atmosphere Research Satellite*. MLS uses a 1.6-m scanning antenna to observe the atmospheric limb emission simultaneously in spectral bands at 63, 183, and 205 GHz (Barath et al. 1993). These observations allow the determination of chlorine monoxide, ozone, water vapor, nitric acid, sulfur dioxide, temperature, and geopotential height in the stratosphere and mesosphere during both day and night and in the presence of stratospheric clouds and aerosols. This study analyzes temperature, geopotential height, and ozone data from two austral late-winter time periods, 14 August–20 September 1992 and 9 August–16 September 1993, when MLS was viewing southward (coverage from 80°S to 34°N).

b. Temperature data

MLS temperature is obtained by viewing limb emission of O₂ at 63 GHz. The version 3 data (used here) are retrieved on every other *UARS* pressure level n (the *UARS* level-3 pressure grid is $1000 \times 10^{-n/6}$ hPa, where $n = 0, 1, 2, \dots$) and have precisions ranging from 1.4 K at 22 hPa to 3.1 K at 0.46 hPa. MLS temperatures are used at eight pressure levels from 22 hPa to 0.1 hPa (22, 10, 4.6, 2.2, 1.0, 0.46, 0.22, 0.1 hPa). The last two levels are contaminated by large systematic errors and are biased by a zonal mean climatology. Wave structures estimated at these levels are attenuated and should be viewed with some caution. Validation information on version 3 MLS temperature is available in Fishbein et al. (1996).

c. Ozone data

MLS ozone retrievals are obtained from limb emission in two bands centered near 205 and 183 GHz. The version 3 ozone data are retrieved on every other *UARS* pressure level. The

205-GHz data have smaller uncertainties throughout the stratosphere, while the 183-GHz data are less noise limited in the mesosphere. Both 205- and 183-GHz ozone data are used in this paper from 22 to 0.22 hPa. Validation information on version 3 MLS ozone is available in Froidevaux et al. (1996) and Ricaud et al. (1996). Single-profile precision for ozone retrievals is in the 0.1–0.4 ppmv range, depending on altitude.

d. Geopotential height data

The MLS geopotential height dataset used in this study is a preliminary dataset, which is not available in version 3 but is planned in future versions. The geopotential height is obtained by measuring pressure as a function of tangent-point height. Pressure is obtained from the same radiances as temperature, but the radiances are sensitive to pressure from 10 hPa to 0.046 hPa. Tangent-point altitude is determined from the orientation of the MLS antenna, measured by an angle encoder, the *UARS* attitude control system, and the ground-tracked *UARS* orbit determination. The pressure (in log pressure coordinates with atmospheric scale height 7 km) precision ranges from 5 m at 10 hPa to 10 m at 0.1 hPa, while the altitude precision is altitude independent and is estimated to be around 100 m. Errors in geopotential height (excluding precision) arising from the tangent-point altitude are synchronized to the *UARS* orbit and contaminate the zonal mean and high frequencies near the diurnal tide. However, the analyses performed in this paper (zonal wave 1, 3–5-day periods) have sufficiently long periods to avoid significant effects from these errors. Good agreement is found on these spatial and temporal scales between MLS temperature (coined $T_{retrieved}$ in this paper) and temperature derived from MLS geopotential height data (T_{geoh}), as discussed in section 4a.

3. Analysis procedure

MLS data used in this analysis were produced by the asynoptic mapping method (Salby 1982a,b; Lait and Stanford 1988a). The specific technique used for this study is presented in detail in Elson and Froidevaux (1993). Briefly, data are binned by latitude and separated into ascending and descending time series. The time and space axes are rotated to a new coordinate

system where a fast Fourier transform (FFT) is applied to calculate the spectral coefficients. An inverse transformation and interpolation allows data to be mapped onto synoptic maps, which are processed every 12 hours. Satellite orbital period drift generally limits the procedure to approximately 1-week analysis periods. The procedure here is essentially a remapping in time so that periods longer than a week can be analyzed. Data are interpolated onto horizontal grids of 4° latitude by 5° longitude and onto the standard *UARS* pressure levels.

The twice-daily synoptic maps described above were decomposed in space and time by applying a two-dimensional sinusoidal transform [see appendix of Ziemke and Stanford (1990)]. Power spectral density is defined in this study as $(2\Delta f)^{-1}[A^2(k, \omega) + B^2(k, \omega)]$, and amplitude is defined as $[A^2(k, \omega) + B^2(k, \omega)]^{0.5}$, where Δf is the unit bandwidth $(\text{NDAT } \Delta t)^{-1}$. NDAT is the number of data points in the time series (NDAT=38 for 1992, NDAT=30 for 1993) and Δt is the temporal sampling interval (0.5 day); $A(k, \omega)$ and $B(k, \omega)$ are the cosine and sine coefficients of the discrete Fourier expansions

$$\{T_{\pm}, \Phi_{\pm}, \mu_{\pm}\}(x, t) = \sum_{k=0}^{\pi/\Delta x} \sum_{\omega=0}^{\pi/\Delta t} \left[A_{\pm}(k, \omega) \cos(kx \pm \omega t) + B_{\pm}(k, \omega) \sin(kx \pm \omega t) \right]. \quad (2.1)$$

Here T , Φ , and μ are temperature, geopotential, and ozone mixing ratio; $+$ ($-$) refers to westward (eastward) components; t is time; x is zonal distance; Δx is the zonal grid interval of $2\pi a \cos \phi / 72$; k is the zonal wavenumber; ω is the angular frequency; a is the earth's radius; and ϕ is latitude. A 1-2-1 running mean was applied in frequency space to power spectral density, but not to amplitude. The time mean was removed before applying the FFT to focus the analysis on traveling waves.

Filtered time series in this study were produced by first applying the bandpass filter response function (with half-amplitude points at 3 and 5 day periods) given by Murakami (1979) to the temporal FFT coefficients and then recombining the coefficients through an inverse FFT.

As a comparison to the MLS temperature measurements, temperature was also calculated from MLS geopotential height using the hydrostatic approximation $T = R^{-1} \partial \Phi / \partial (\ln p)$, with $R = 287 \text{ J kg}^{-1} \text{ K}^{-1}$ (dry air gas constant) and constant vertical spacing $d(\ln p) = 0.387$ (determined from *UARS* standard pressure surfaces). Quasigeostrophic potential vorticity q'

and potential vorticity gradient \bar{q}_y were calculated using the spherical formulation of Matsuno (1970):

$$q' = \frac{1}{fa^2} \left[\frac{\Phi'_{\lambda\lambda}}{\cos^2 \phi} + \frac{f^2}{\cos \phi} \left(\frac{\cos \phi}{f^2} \Phi'_{\phi} \right)_{\phi} + \frac{f^2 a^2}{\rho_o} \left(\frac{\rho_o \Phi'_z}{N^2} \right)_z \right] \quad (2.2)$$

$$\bar{q}_y = \frac{2\Omega \cos \phi}{a} - \left[\frac{(\bar{u} \cos \phi)_{\phi}}{a^2 \cos \phi} \right]_{\phi} - \frac{1}{\rho_o} \left(\frac{\rho_o f^2 \bar{u}_z}{N^2} \right)_z. \quad (2.3)$$

Here u is the zonal wind, $\rho_o = \rho_{oo} e^{-z/H}$, ρ_{oo} is the density at the surface (1000 hPa), z is the log-pressure coordinate, λ is longitude, f is the Coriolis parameter, and Ω is the earth's angular frequency. Overbars denote zonal means, primes denote deviation from the zonal mean, and subscripts denote partial derivatives. The Brunt-Väisälä parameter and atmospheric scale height were given the constant values $N^2 = 4 \times 10^{-4} \text{ s}^{-2}$ and $H = 7 \text{ km}$; q' was calculated from MLS geopotential height data, while \bar{q}_y was calculated from U. K. Meteorological Office (UKMO) zonal winds. MLS data were not used in the calculation of \bar{q}_y due to the known inaccuracy in the zonal mean geopotential height (see section 2d).

UKMO horizontal winds and temperatures on UARS pressure surfaces, obtained from the Goddard Space Flight Center Distributed Active Archive Center (DAAC), were interpolated with a cubic spline onto horizontal grids of 4° latitude by 5° longitude. These winds and temperatures were used in the calculation of \bar{q}_y and also in the tracer model discussed in section 4c.

The quasigeostrophic Eliassen-Palm (EP) flux vector and the EP flux divergence were calculated with the the following spherical formulation:

$$\mathbf{F} = (F_{\phi}, F_z) = \rho_o a \cos \phi \left(-\overline{u'v'}, \frac{R}{H} f \frac{\overline{v'T'}}{N^2} \right) \quad (2.4)$$

$$\nabla \cdot \mathbf{F} = \frac{1}{a \cos \phi} \frac{\partial}{\partial \phi} (\cos \phi F_{\phi}) + \frac{\partial F_z}{\partial z}. \quad (2.5)$$

Here u' and v' (meridional wind) are calculated from MLS geopotential heights (using the geostrophic approximation) and T' is from MLS-retrieved temperatures. In the EP flux diagram (Fig. 2.11), the vector components are multiplied by $2\pi a \cos \phi$. This factor accounts for the spherical geometry of the earth to make the arrow pattern look nondivergent if and only if $\nabla \cdot \mathbf{F} = 0$ (see Edmon et al. 1980).

4. Results

a. Temperature

Space-time spectral decomposition is a useful tool for isolating the 4-day wave from other atmospheric signals. Figure 2.1a presents a periodogram for zonal wavenumber 1 power spectral density (defined in section 3 and hereafter called *power*) for MLS-retrieved temperature (hereafter $T_{retrieved}$) at 72°S latitude for 18 August–6 September 1992. A clear 4-day eastward period signal exists near 1 hPa (48 km) and a somewhat weaker signal occurs near 0.22 hPa (60 km). These signals are also evident in temperature derived from MLS geopotential height (hereafter T_{geoh}) in Fig. 2.1b, although the lower signal maximizes near 2.2 hPa (42 km). An even stronger 4-day signal is found during 2–16 September 1993 in both $T_{retrieved}$ (Fig. 2.1c) and T_{geoh} (Fig. 2.1d). The 4-day signal dominates the traveling wave spectra for this time period with two lobes centered near 2.2 hPa (42 km) and 0.22 hPa (60 km). Sections 4d and 4f further discuss the validity of the 4-day signal in terms of uncertainty and statistical significance.

The 1992 4-day wave event was further isolated by filtering a 38-day series of $T_{retrieved}$ for zonal wavenumber 1 and periods (both eastward and westward) of 3–5 days and plotting on a Hovmöller (time vs longitude) diagram for 64°S and 1 hPa (Fig. 2.2). The 4-day wave amplitude increases over the first 10 days and remains constant for another 10 days before dissipating near 1 September 1992. The mode makes at least five revolutions around the pole with a rotation period near 3.8 days.

Spectral plots of $T_{retrieved}$ for zonal wavenumbers 2 and 3 (not shown here) for the 1992 event show signals at 1 hPa with eastward periods of 2.0 and 1.3 days, respectively. These sinusoidal components move at the same phase speed of the wave 1, 4-day signal and combine with wave 1 to form a “warm pool” of air at 1 hPa (coupled with a slightly less prominent “cold pool”) that rotates around the pole with a period near 4 days. This feature is shown in Fig. 2.3, where $T_{retrieved}$ data have been filtered over 14 August–20 September 1992 for waves 1–3 and eastward rotation periods of 3–5 days. (Wave 4 and higher were not analyzed because

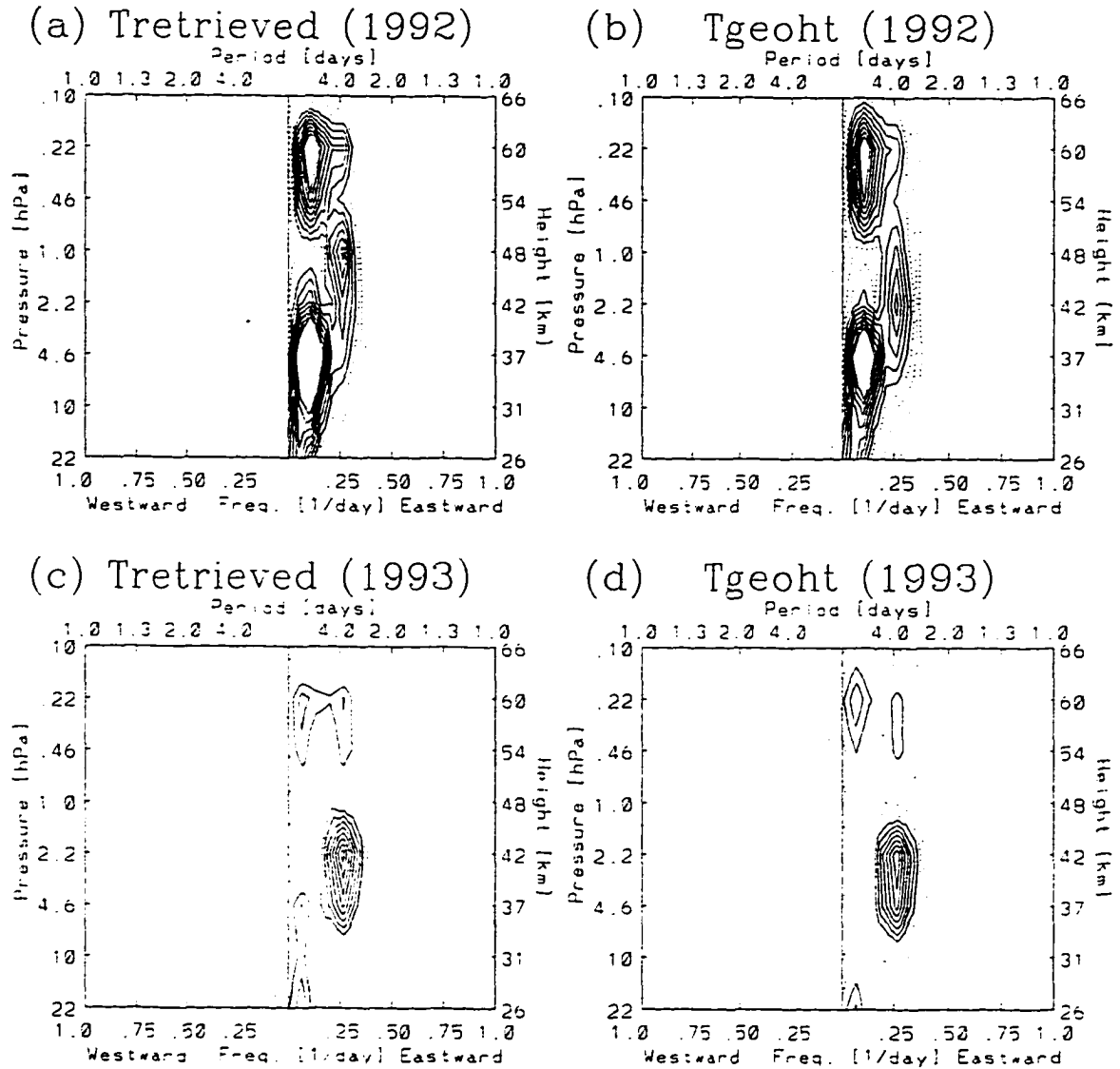


Figure 2.1 (a) East-west power spectrum for wave 1 MLS temperature ($T_{\text{retrieved}}$) at 72°S for 18 August–6 September 1992. Dashed contours are at 10, 20, and 30 $\text{K}^2 \text{ day}$ and solid contours are from 40 to 100 $\text{K}^2 \text{ day}$ by 10 $\text{K}^2 \text{ day}$. (b) Same as (a) but for temperature derived from MLS geopotential height (T_{geoht}). (c),(d) Same as (a),(b) but for 2–16 September 1993.

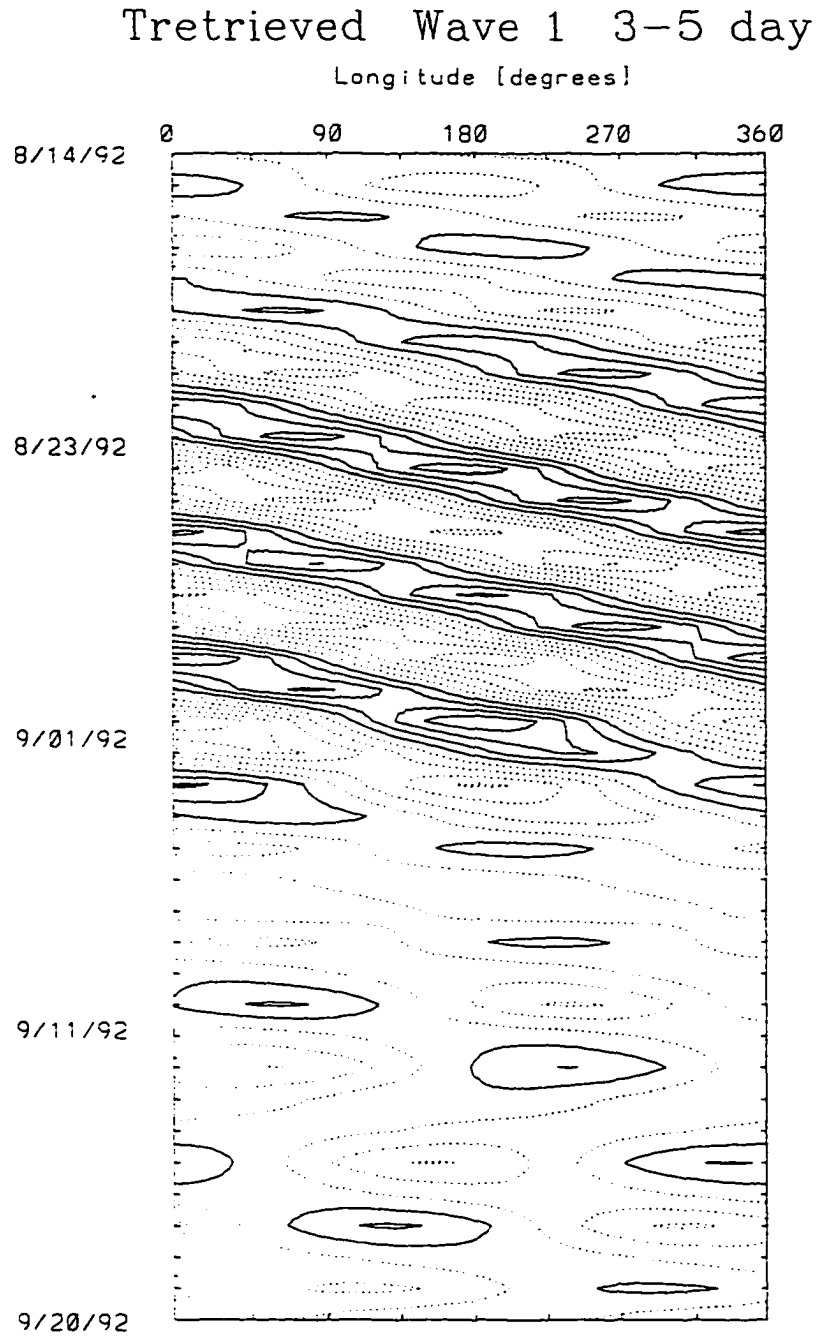


Figure 2.2 Time vs longitude plot of $T_{\text{retrieved}}$ at 64°S and 1 hPa (48 km) filtered for wave 1 and 3–5 day periods (eastward and westward) for 14 August–20 September 1992. Dashed contours are from -4 to 0 K by 1 K. Solid contours are from 1 to 4 K by 1 K.

Tretrieved Waves 1-3 3-5 day (1 hPa)

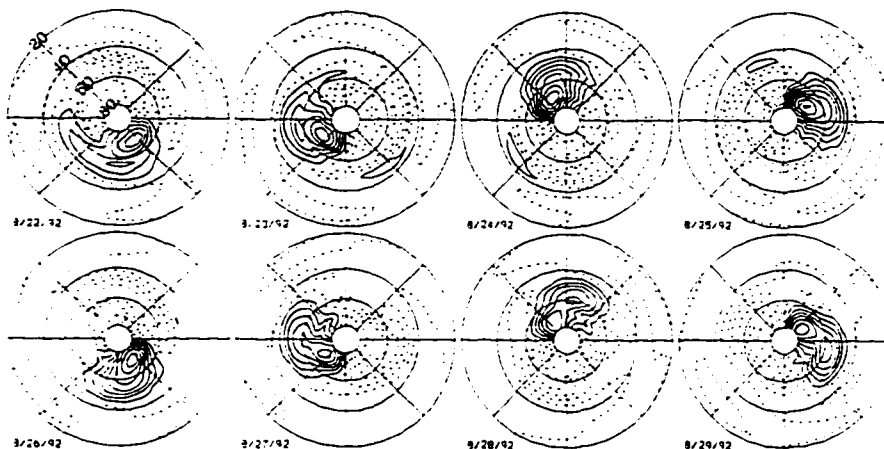


Figure 2.3 Polar stereographic plots of MLS temperature at 1 hPa filtered for waves 1-3 and 3-5 day eastward periods for 22-29 August 1992. Latitude circles are at 20°, 40°, 60°, and 80°S with the South Pole at the center. Eastward direction is clockwise with 0° longitude on the positive vertical axis. Dashed contours are from -5 to 0 K by 1 K. Solid contours are from 1 to 8 K by 1 K.

the frequency of interest, 4 days divided by integer wavenumber, is near or outside the Nyquist limit of approximately 1 day^{-1} .) The warm pool rotates around the pole as an identifiable entity throughout the record shown displaying the quasi-nondispersive (soliton-like) nature of the feature.

The perturbation temperature ($T_{\text{retrieved}}$) amplitude for wave 1 and 3.8-day eastward period is plotted in Fig. 2.4a for the 1992 4-day wave event. A large lobe exists in the upper stratosphere, peaking near 48 km and 72°S with maximum amplitude of 4.2 K. A smaller upper lobe is centered at 60 km and 68°S. This double-lobed structure is similar to that predicted by the instability study of Manney and Randel (1993). In their results, the upper lobe is larger and extends well into the mesosphere. However, $T_{\text{retrieved}}$ is largely climatology at 66 km, forcing zonally asymmetric wave amplitudes to zero; therefore, the abrupt fall-off with height above 60 km in Fig. 2.4a may not be real. The 1993 series also displays a double-lobed structure (Fig. 2.4b), with maxima near 42 km, 76°S (amplitude of 5.8 K) and 60 km, 80°S.

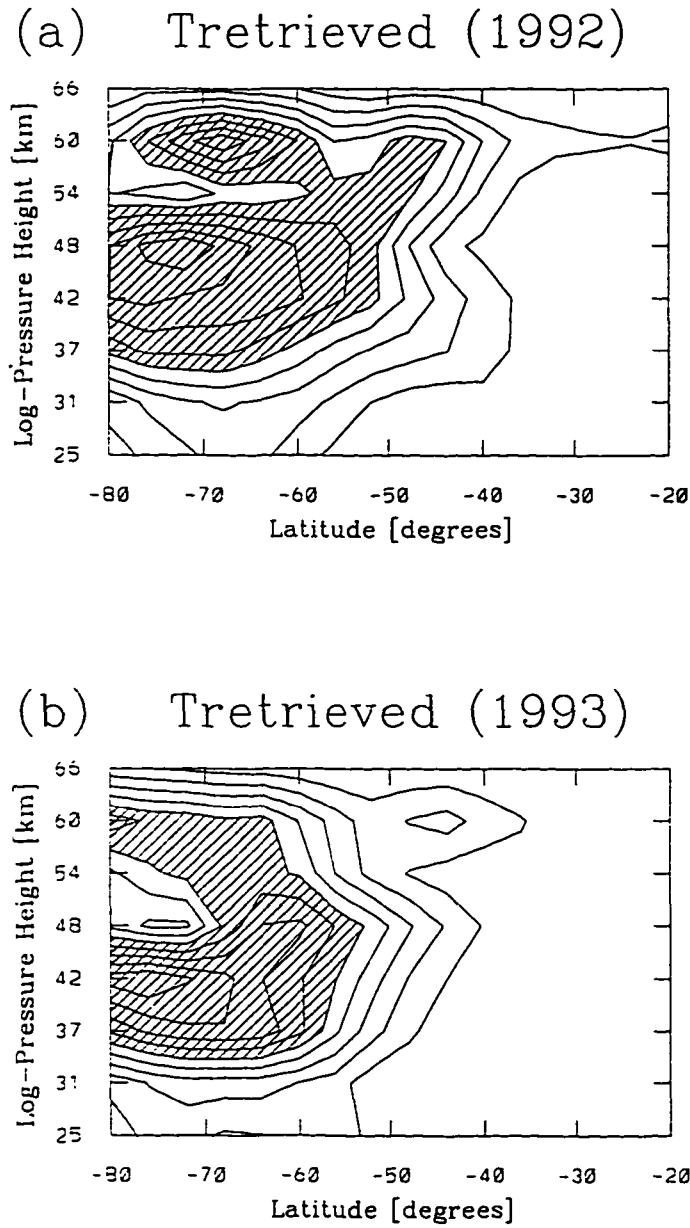


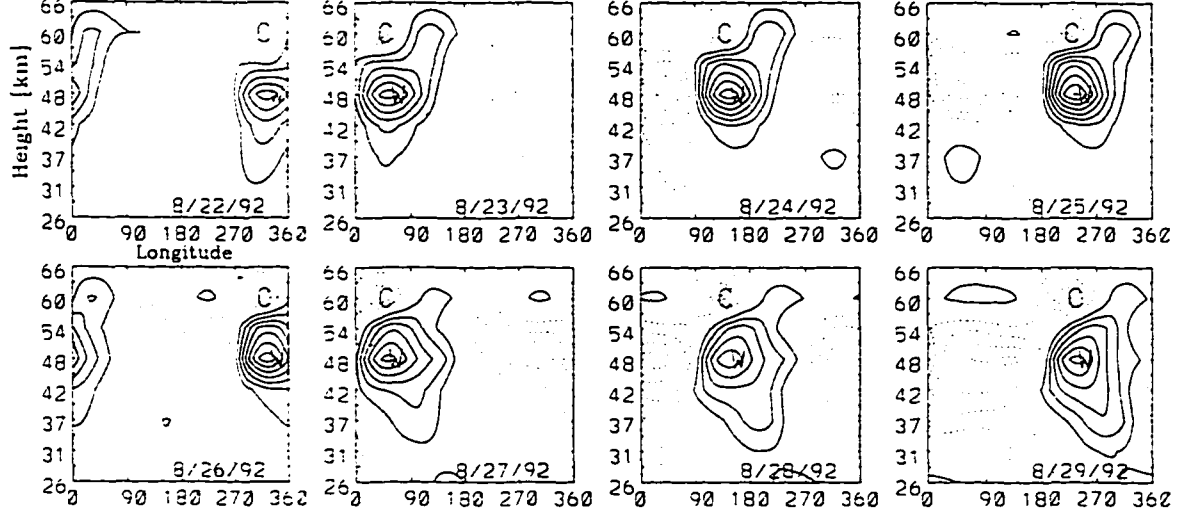
Figure 2.4 (a) $T_{retrieved}$ amplitude for wave 1 and 3.8-day eastward period for 18 August–6 September 1992. Contours are every 10% interval of the maximum (4.2 K), with values higher than 50% shaded. (b) $T_{retrieved}$ amplitude for wave 1 and 3.75 day eastward period for 2–16 September 1993. Contours are every 10% of the maximum (5.8 K), with values higher than 50% shaded.

Manney and Randel (1993) also predict rapid vertical phase variation between the two lobes. Such behavior can be explicitly seen in height versus longitude plots of $T_{retrieved}$ at 72°S, filtered for waves 1–3 and eastward rotation periods of 3–5 days. Figure 2.5a presents 8 days during the peak amplitude of the 1992 time series. The plots reveal a warm anomaly near 48 km bounded above by a cold anomaly near 60 km. This dipole pattern continues throughout the 4-day wave lifecycle, suggesting that the two peaks constitute one entity. The 1993 series also reveals this vertical temperature dipole (Fig. 2.5b). Here the lower peak has a strong wave 1 structure that begins near 48 km and descends to 42 km over this 8-day period. The upper feature, which maximizes near 60 km, is approximately 180° out of phase with the lower feature. The quadrupole pattern produced by the two out-of-phase lobes remains stable for at least two weeks, through the end of the *UARS* month (16 September 1993), when MLS changed to northward viewing (coverage from 80°N to 34°S).

b. Geopotential

The vertical temperature dipole structure seen in Fig. 2.5 suggests that the perturbation geopotential amplitude should increase with height throughout the region of the lower temperature lobe and decrease with height in the region of the upper lobe. This is confirmed in Fig. 2.6a, which shows the geopotential amplitude for the 1992 series for eastward moving wave 1 with a period of 3.8 days. The signal maximizes near 57 km, at the boundary between the warm and cold anomalies (see Fig. 2.5a), and decreases above it. The 1993 geopotential amplitude (Fig. 2.6b) peaks near 48 km, consistent with the perturbation temperature structure for that series (Fig. 2.5b). The geopotential signal decreases with altitude more rapidly in the 1993 time series, due to a larger-amplitude upper temperature lobe in 1993 than in 1992. The meridional structure shown here is similar to previous observations of the 4-day wave in geopotential height (Manney 1991; Lawrence and Randel 1996).

(a) Retrieved W 1-3, 3-5 day (22-29 August 1992)



(b) Retrieved W 1-3, 3-5 day (4-11 September 1992)

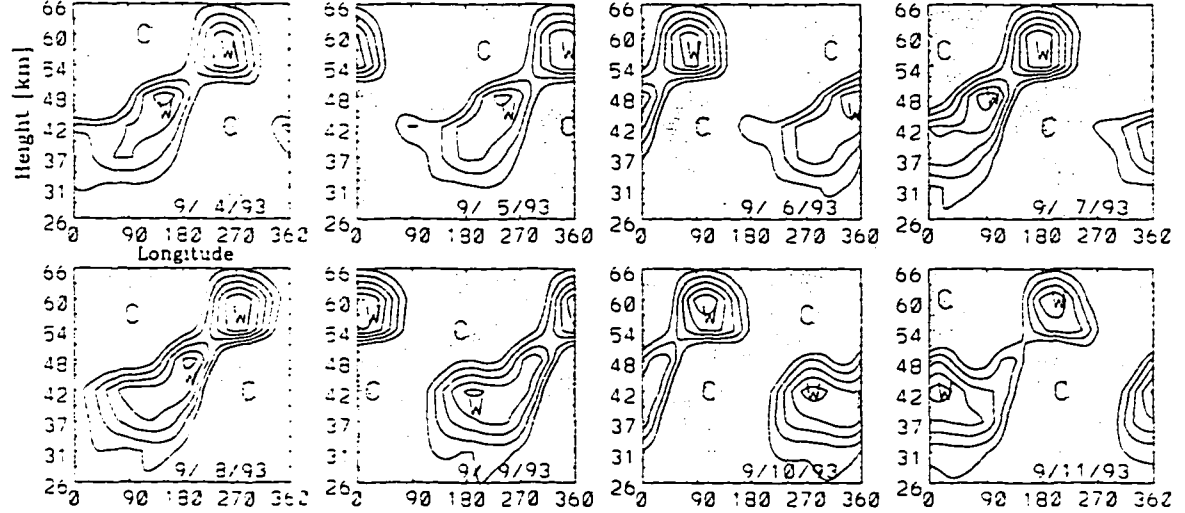
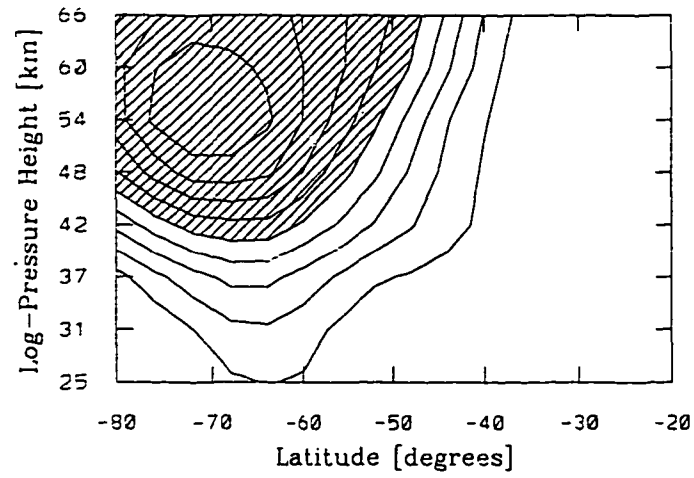


Figure 2.5 (a) $T_{\text{retrieved}}$ on a height vs longitude grid at 72°S filtered for waves 1-3 and 3-5-day eastward rotation period for 22-29 August 1992. (b) Same as (a) but for 4-11 September 1992. Contours are every 1 K with solid (dashed) lines having positive (negative) values. Here, W (C) refers to warm (cold) anomalies.

(a) Geopotential (1992)



(b) Geopotential (1993)

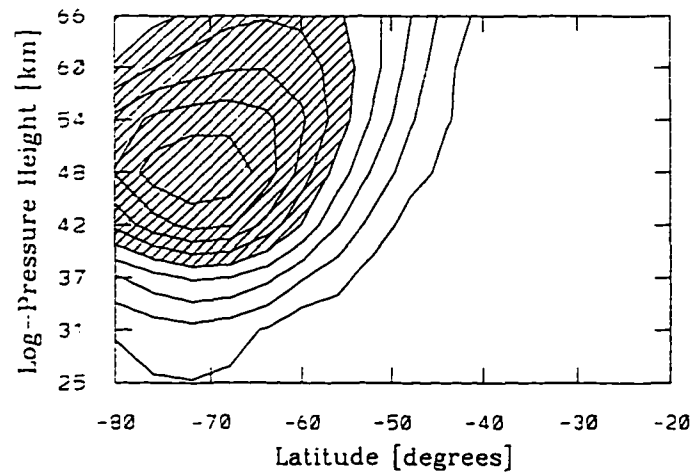


Figure 2.6 (a) MLS geopotential amplitude for wave 1 and 3.8-day eastward period for 18 August–6 September 1992. (b) Same as (a) but for 2–16 September 1993, 3.75-day eastward period. Contours are at every 10% interval of the maximum with values higher than 50% shaded.

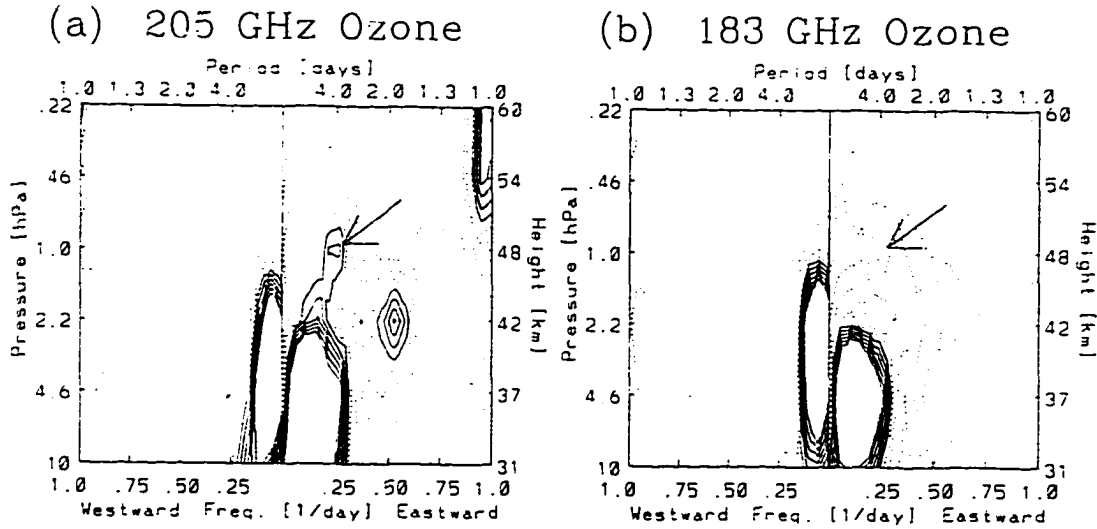


Figure 2.7 (a) East-west power spectrum for wave 1 MLS ozone (205 GHz) at 72°S for 18 August–6 September 1992. Contour increment is 0.02 ppmv²·day. Dashed lines are from 0.02 to 0.08 ppmv²·day. Solid lines are from 0.10 to 0.20 ppmv²·day. (b) Same as (a) but for 183-GHz MLS ozone.

c. Ozone

Other than the unpublished conference report by Randel et al. (1992), the present paper is the first to present observations of the 4-day wave in ozone. Periodograms for wave 1 MLS ozone (both 205- and 183-GHz data) at 72°S during 18 August–6 September 1992 are presented in Fig. 2.7. A 4-day peak exists near the stratopause (1.0 hPa), coincident with the $T_{\text{retrieved}}$ maximum at the same altitude; see Fig. 2.1a. A 2-day eastward period signal exists at 2.2 hPa; the source of this signal is unknown and is not thought to be related to the 4-day wave. The 2-day feature does not exist in spectra from 5 to 20 September 1992.

To ascertain the relationship between the 4-day feature in ozone and the other atmospheric variables, a linear advective–photochemical model was used to calculate the ozone response to temperature and meridional wind perturbations associated with the 4-day wave. The procedure combines the linearized thermodynamic and ozone continuity equations to obtain an expression for the ozone mixing ratio (Hartmann and Garcia 1979; Rood and Douglass 1985; Randel 1990, 1993). Because the 4-day wave amplitudes in the various components (T , u , v , and μ) are

observed to be much less than their respective zonal-mean values ($T' \ll \bar{T}$, etc.), we use a linearized thermodynamic equation,

$$T'_t + \bar{u}T'_x + v'\bar{T}_y + w'S = 0 \quad (2.6)$$

$$S = \frac{1}{H} [\kappa\bar{T} + H\bar{T}_z],$$

where w' is the vertical wind component, $\kappa = R/c_p \approx 2/7$, and $H = 7$ km; and a linearized ozone continuity equation,

$$\mu'_t + \bar{u}\mu'_x + v'\bar{\mu}_y + w'\bar{\mu}_z = -\Gamma\mu' - \Theta T'. \quad (2.7)$$

The photochemical relaxation rate, Γ , and the linearized ozone response to small temperature perturbations, Θ , are shown in Fig. 2.8a, adapted from Hartmann and Garcia (1979), who studied ozone transport by planetary waves in the winter stratosphere using a linearized β -plane model centered at 60° . Radiative damping of the temperature perturbations is neglected, since the radiative timescale is of order 10 days in the region of interest (26–57 km) [see Hartmann and Garcia (1979)], while the advective timescale $[k(\bar{u} - c)]^{-1}$ is of order 1–2 days from 26 to 42 km, and the photochemical timescale Γ^{-1} is less than 1 day from 42 to 57 km. Radiative heating from ozone perturbations has also been neglected, as in Randel (1990, 1993), since it is likely small compared to changes due to advection. Solving Eq.(2.6) for w' and substituting into Eq.(2.7) gives the following differential equation for μ' :

$$\left(\frac{\partial}{\partial t} + \bar{u} \frac{\partial}{\partial x} + \Gamma \right) \mu' + \left(\bar{\mu}_y - \frac{\bar{\mu}_z}{S} \bar{T}_y \right) v' - \left[\frac{\bar{\mu}_z}{S} \left(\frac{\partial}{\partial t} + \bar{u} \frac{\partial}{\partial x} \right) - \Theta \right] T' = 0. \quad (2.8)$$

To relate μ' to T' and v' , we write $(\mu', T', v') = (M, T, V) e^{ik(x-ct)}$, where M , T , and V denote complex-valued perturbation amplitudes. From this,

$$M = - \frac{(\Theta - ib)T + \xi V}{\Gamma + ia} \quad (2.9)$$

$$\xi \equiv \bar{\mu}_y - \bar{\mu}_z \bar{T}_y / S \quad a \equiv k(\bar{u} - c) \quad b \equiv k(\bar{u} - c) \bar{\mu}_z / S.$$

Figure 2.8b presents the resulting model ozone amplitude for the wave 1, 3.8-day period signal at 60°S (thick solid line). Also plotted are the observed ozone amplitudes at 60°S

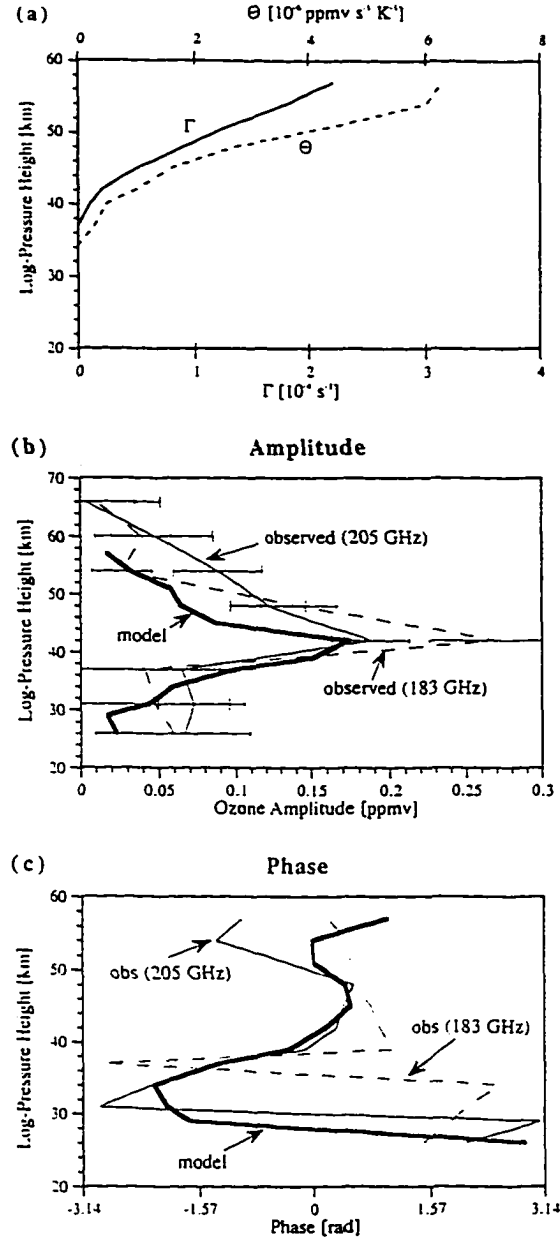


Figure 2.8 (a) Ozone photochemical parameters adapted from Hartmann and Garcia (1979). The curve Γ is the photochemical relaxation rate, and Θ is the linearized ozone response to small temperature perturbations. (b) Wave 1 ozone amplitude (in ppmv) at 60°S for 3.8-day eastward period from 18 August to 6 September 1992. Lines are model (thick solid), 205-GHz observations (thin solid), and 183-GHz observations (dashed). Error bars were calculated using the procedure described in section 4d. Large (small) caps show the extent of the 205 (183) GHz ozone error bars. (c) Same as (b) but for phase and excluding error bars.

for 205-GHz (thin solid) and 183-GHz (dashed) data. Error bars on the observed data were calculated using the procedure described in section 4d. Reasonable agreement is found between the observed and model amplitudes, with low values in the middle stratosphere and lower mesosphere, and a maximum in the upper stratosphere (near 42 km). Results from a purely advective model ($\Gamma = \Theta = 0$) and a purely photochemical model [$\mu_{amp} = (\Theta/\Gamma) T_{amp}$, see Randel (1990)] show a transition region between dynamical and photochemical control from approximately 37 to 49 km, where both dynamics and photochemistry play an important role.

The phase of the model and observed 4-day feature is provided in Fig. 2.8c. Good agreement exists between the 205-GHz observed phase and the model throughout the stratosphere, while the 183-GHz observed phase agrees with the model in the lower mesosphere but diverges somewhat in the stratosphere. As mentioned in section 2c the 205-GHz data have smaller uncertainties in the stratosphere, while the 183-GHz data are less noise limited in the mesosphere, so the phase results shown here are consistent with the data quality.

The good agreement (at least to first order) between model and observations suggests that the observed 4-day signal in ozone is produced largely by the coupled effects of constituent advection by the 4-day wave perturbation winds in the presence of zonal-mean constituent gradients and photochemical processes associated with the 4-day wave perturbation temperature and mixing ratio anomalies.

d. Uncertainty in 4-day wave amplitude

In order to assess the uncertainty in the 4-day wave amplitude calculation, a random number generator was used to make a noise dataset with level 3AT format (along-track, evenly spaced in time) with values between -0.5 and $+0.5$ (arbitrary units), giving a root mean square (rms) variation of 0.29. This represents the random noise in a given MLS measured quantity with an rms error (defined here as uncertainty) of 0.29. These data were passed through the asymptotic mapping routine described in section 2 and synoptic maps were produced. The rms variation in the synoptic maps is 0.19, which is 65% of the input value. The decrease is mainly due to interpolation to a regular horizontal grid. Fourier decomposition was then applied to

isolate the amplitude of the wave 1, 3.8-day component from 500 different time series, each randomly generated. This Monte Carlo procedure yielded rms variations in amplitude of 0.018 for the 1992 simulated series (38 time components used, 72 longitudes) and 0.020 for the 1993 simulated series (30 time components used, 72 longitudes). The uncertainty in amplitude is $0.018/0.29 \approx 1/16$ times the uncertainty in the level 3AT data for 1992 and $1/14$ for 1993. The difference between $1/16$ and $1/14$ is due to the different bandwidth used in each year. This method can now be used to obtain estimated uncertainties in 4-day wave amplitudes observed in MLS temperature and ozone.

The estimated uncertainty in version 3 MLS temperature at 1 and 2.2 hPa is 3.4 and 2.2 K, respectively (Fishbein et al. 1996). The estimated wave 1 3.8-day eastward period amplitude uncertainty in the lower peak of Fig. 2.4a (1992) is $3.4/16 = 0.21$ K, which is much smaller than the observed amplitude of 4.2 K. In 1993 the uncertainty in the lower peak (Fig. 2.4b) is $2.2/14 = 0.16$ K, which is much less than the observed amplitude of 5.8 K. This Monte Carlo analysis shows that the observed amplitudes are not significantly affected by random noise in the data.

This method was also used to obtain estimated errors for 205- and 183-GHz MLS ozone data. The error bars shown in Fig. 2.8b were computed using the above formulation along with data uncertainties at different pressure levels as given by Froidevaux et al. (1996).

e. Statistical assessments

Because the 4-day wave is a well-established atmospheric phenomenon (see references in the introduction), statistical assessment of the 4-day features found here can be made on the basis of a priori statistics (Madden and Julian 1971). Briefly, before analysis it is decided to examine spectral features near 4-day periods. [If spectral peaks are examined at previously unreported frequencies, a posteriori statistics must be used (Madden and Julian 1971).] The null hypothesis is made that any spectral peak at 4 days is due to random sampling fluctuations. Under this hypothesis, the ratio of spectral peak to nearby spectral background can be estimated statistically. For the Fourier transform spectra used here, chi-squared statistics are employed

to estimate the maximum peak to background ratio that will occur in 95% of the cases for random sampling fluctuations. If the observed peak exceeds this ratio, with 95% confidence the spectral feature can be said to be statistically significant.

Figures 2.9a,b show the $T_{retrieved}$ spectra at 2 and 0.2 hPa during 2–16 September 1993. These are plotted without smoothing in Figs. 2.9a,b and correspond to the smoothed plot shown in Fig. 2.1c. Also indicated by dashed lines in Fig. 2.9 are the estimated background and 95% confidence limit (for two degrees of freedom, appropriate to this case of unsmoothed Fourier transform spectral estimates). Both features easily satisfy a priori statistical significance.

The 1992 temperature spectral 4-day peak, shown smoothed in Fig. 2.1a, reveals a strong peak centered at 1 hPa that also easily exceeds the a priori 95% confidence limit (not shown here). The weaker temperature peak at 0.22 hPa is close to a stronger lower-frequency feature. By examination of unsmoothed spectral results (not shown here), it can be shown that the 0.22-hPa 4-day peak also meets the criterion for a priori statistical significance.

The 183-GHz ozone spectrum at 1 hPa for 1992 (shown smoothed in Fig. 2.7b) is plotted unsmoothed in Fig. 2.9c. The 4-day peak exceeds the 95% confidence limit and is judged statistically significant. The 205-GHz ozone 4-day peak at 1 hPa (Fig. 2.7b) also exceeds the 95% confidence limit (not shown here).

f. Zonal wind, \bar{q}_y and EP flux structure

Theoretical studies show that barotropic and/or baroclinic instability of the polar night jet can produce quasi-nondispersive modes similar to the observed 4-day wave. The instability episodes are generally accompanied by regions of negative quasigeostrophic potential vorticity gradient \bar{q}_y and nonzero EP flux divergence. Figure 2.10a shows the zonal mean UKMO east–west wind averaged over the lifecycle of the 1992 4-day wave event (18 August–6 September 1992). A strong stratospheric westerly jet is centered near 34 km, 60°S. The associated wind curvature produces a region of negative \bar{q}_y near 50°S at altitudes above 50 km (Fig. 2.10b). Daily wind maps reveal a “double jet” structure near the beginning of the time se-

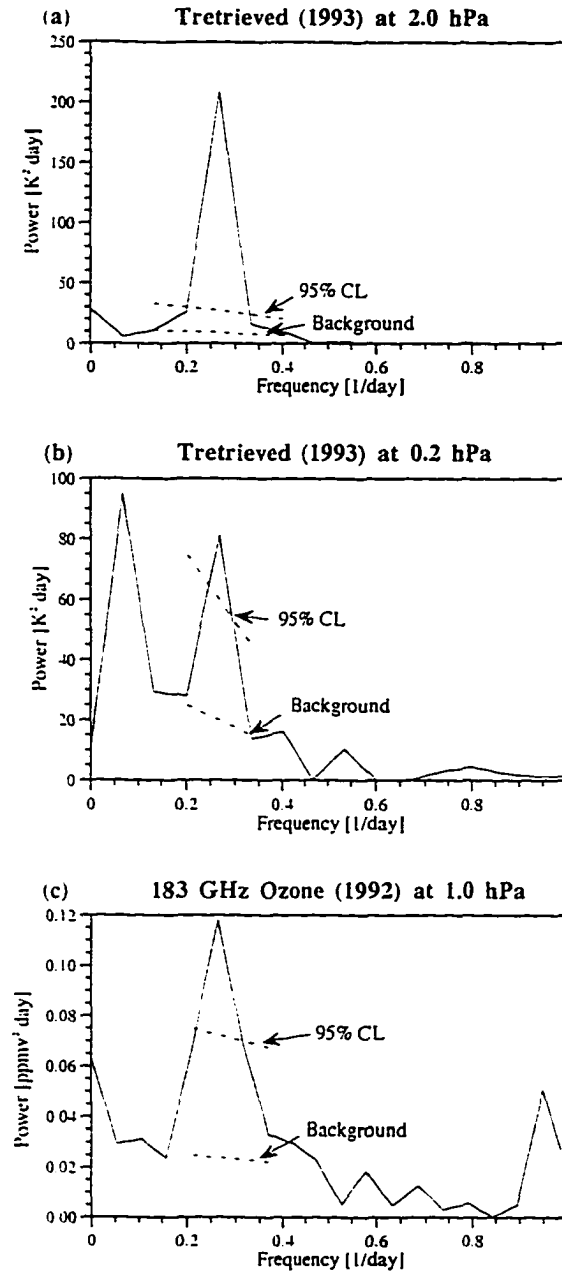
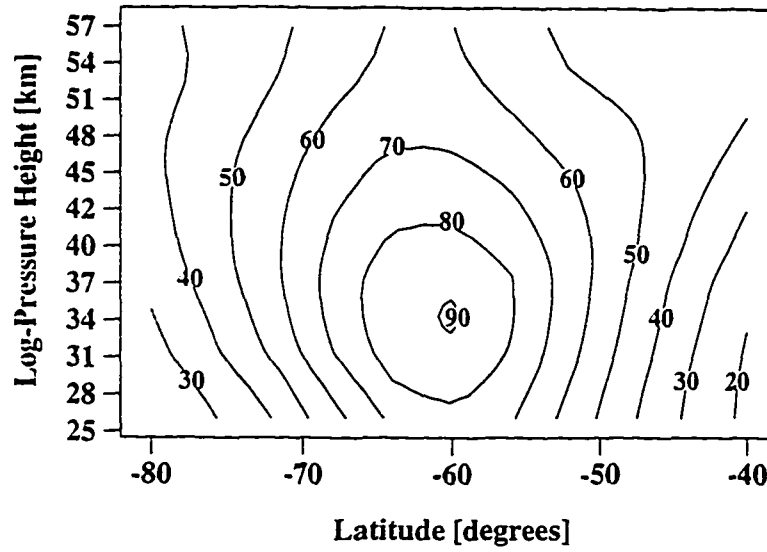


Figure 2.9 Unsmoothed power spectra for wave 1 at 72°S plotted along with estimated background and 95% confidence level. (a) $T_{\text{retrieved}}$ for the 1993 series at 2 hPa. (b) $T_{\text{retrieved}}$ for the 1993 series at 0.2 hPa. (c) 183-GHz ozone for the 1992 series at 1.0 hPa.

(a) UKMO Zonal Wind 18 August - 6 September 1992



(b) QGPV Gradient 18 August - 6 September 1992

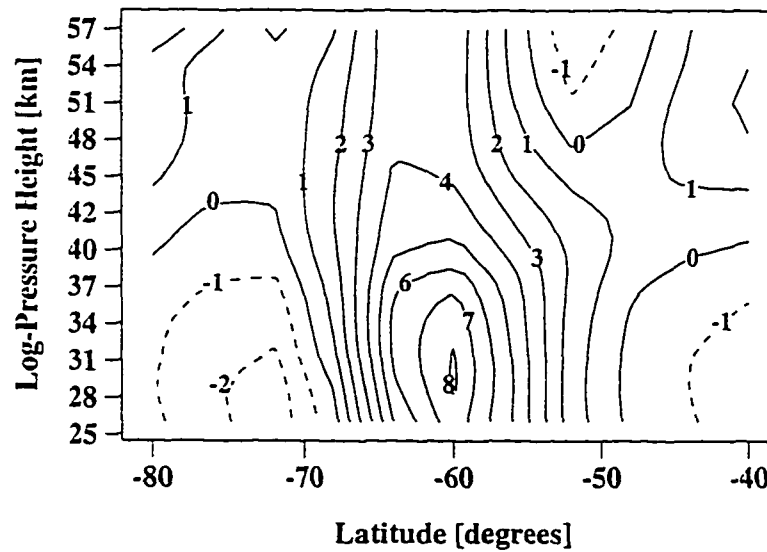


Figure 2.10 (a) UKMO zonal mean zonal wind (westerly, in m s^{-1}) averaged from 18 August to 6 September 1992. (b) Quasi-geostrophic potential vorticity gradient, \bar{q}_y , averaged from 18 August to 6 September 1992. Contour increment is $1.0 \times 10^{-11} \text{ m}^{-1} \text{ s}^{-1}$ with negative values dashed.

ries, which is often present during 4-day wave events (Manney 1991; Randel and Lait 1991). Manney et al. (1996) showed that daily maps of Ertel PV (on isentropic surfaces) calculated from UKMO winds sometimes exhibit unrealistic structure in the Southern Hemisphere winter middle and upper stratosphere poleward of about 70°S . Our analyses here, however, focus on quasigeostrophic PV averaged over 20 days. Comparison of Fig. 2.10a with National Centers for Environmental Prediction (NCEP, formerly NMC) zonal winds (not shown here) suggests good overall agreement. However, \bar{q}_y calculated from the NCEP data (which extends only to 54 km) does not show the negative region near 50°S for this time-averaged period, although negative \bar{q}_y does exist near 50°S , 54 km for several of the individual NCEP-derived daily maps during the first half of this time series. (Note that time-averaged fields are more smoothed than the wind field on any given day, so they often underestimate instability.)

Linear theory requires that wave growth by barotropic instability be accompanied by negative PV gradients. [The integral over latitude of \bar{q}_y times a positive definite quantity must be zero for wave growth to occur by *barotropic* instability. However, *baroclinic* instability is possible with positive \bar{q}_y , given suitable variation with latitude of the vertical gradient of \bar{u} at the lower boundary: see Holton (1992).] The presence here of negative \bar{q}_y regions is consistent with the fact that negative \bar{q}_y is a necessary, although not sufficient, condition for wave growth by barotropic instability.

Figure 2.11 displays the EP flux diagram for this wave episode, giving details about the net effect on the zonal mean state of eddy and momentum fluxes due to wave events. The EP flux was calculated using MLS temperature and geopotential height from 18 August to 6 September 1992, filtered for the wave 1 and 3.8-day eastward period. The geostrophic approximation was used to calculate the winds from the 4-day wave perturbation geopotential field. The EP vectors are plotted over contours of $DF = \nabla \cdot \mathbf{F} / (\rho_0 a \cos \phi)$, which is a force per unit mass on the zonal-mean wind (in $\text{m s}^{-1} \text{ day}^{-1}$) due to the eddy effects associated with the wave 1 component of the 4-day wave. Positive (negative) regions of DF act to accelerate (decelerate) the zonal-mean westerly wind. Positive DF exists between 50° and 75°S at the top of the plot, near 57 km, acting to accelerate the lower-mesospheric winds, while a negative DF region near 54 km,

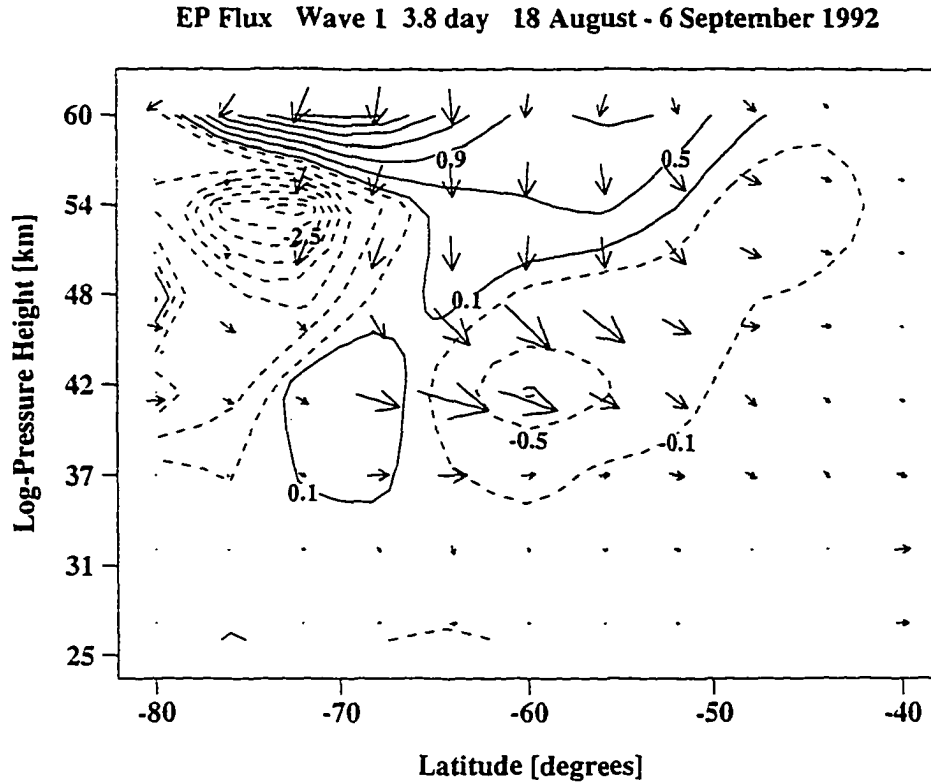


Figure 2.11 Eliassen-Palm flux diagram calculated for the wave 1, 3.8-day eastward period components of MLS temperature and geopotential height from 18 August to 6 September 1992. Contours are $DF = \nabla \cdot \mathbf{F} / (\rho_0 a \cos \phi)$ starting at 0.1 and incremented at $0.4 \text{ m s}^{-1} \text{ day}^{-1}$ with solid (dashed) line indicating positive (negative) values. Arrows are the Eliassen-Palm flux vectors.

72°S acts to decelerate the stronger stratopause winds (see Fig. 2.10a). Figure 2.11 predicts eddy-induced reduction of vertical shear in the 60°S – 75°S lower-mesosphere region, consistent with baroclinic instability mechanisms driving the 4-day wave in the lower mesosphere. The EP flux structure above 48 km is similar to the model results from Manney and Randel (1993, their Fig. 2.2d), with a region of negative DF bounded above and to the north by positive DF .

The EP flux vectors indicate strong equatorward heat flux (downward pointing arrows) and equatorward momentum flux (poleward pointing arrows) above 48 km and poleward of 65°S (also similar to Manney and Randel 1993, Fig. 2.2d) and largely poleward momentum

flux elsewhere. The vectors are predominantly vertical (indicating baroclinic processes) in the lower mesosphere, while strong momentum flux (indicated by horizontal components of EP flux vectors) near 42 km, 60°S suggests barotropic processes play a sizable role there. This is confirmed by the positive (70°S) and negative (60°S) DF regions at 42 km, which act to reduce the latitudinal shear associated with the stratospheric jet (a signature of barotropic instability).

Manney and Randel (1993) and Lawrence and Randel (1996) show overlapping regions of negative \bar{q}_y and positive $\nabla \cdot \mathbf{F}$ during 4-day wave episodes. This spatial coincidence is recognized as a source region of wave activity $A = (1/2)\overline{q'^2}/\bar{q}_y$, where q' represents the perturbation quasigeostrophic potential vorticity. Neglecting diabatic and frictional effects, a conservation equation can be written (Andrews and McIntyre 1976, 1978):

$$\frac{\partial A}{\partial t} + \nabla \cdot \mathbf{F} = 0. \quad (2.10)$$

Clearly, when \bar{q}_y is negative, the wave activity will increase in magnitude when $\nabla \cdot \mathbf{F} > 0$. One region of negative \bar{q}_y occurs in the vicinity of positive DF near 57 km, 52°S. This is consistent with instability dynamics driving the 4-day wave in the lower mesosphere. According to Eq.(2.10), wave activity will also increase if $\bar{q}_y > 0$ and $\nabla \cdot \mathbf{F} < 0$. The regions of negative DF near 54 km, 80°S–65°S and 42 km, 60°S overlap positive \bar{q}_y , suggesting instability forcing may also exist in these regions.

g. Quasigeostrophic potential vorticity

Spectral analyses of quasigeostrophic PV calculated from MLS geopotential heights reveal 4-day signals in both the 1992 and 1993 series. Figure 2.12 shows periodograms for 72°S during 18 August–6 September 1992 (Fig. 2.12a) and 2–16 September 1993 (Fig. 2.12b). Clear 4-day eastward period signals in PV are seen near the stratopause (48 km or 1 hPa) during both time periods. (In 1992, a significant longer-period feature is seen in the upper stratosphere. This eastward moving power with periods of several weeks is not directly related to the 4-day wave considered here.) A height versus latitude plot of PV amplitude for wave 1 and 3.8-day eastward period is provided in Fig. 2.13a for the 1992 series. A region of large PV amplitude

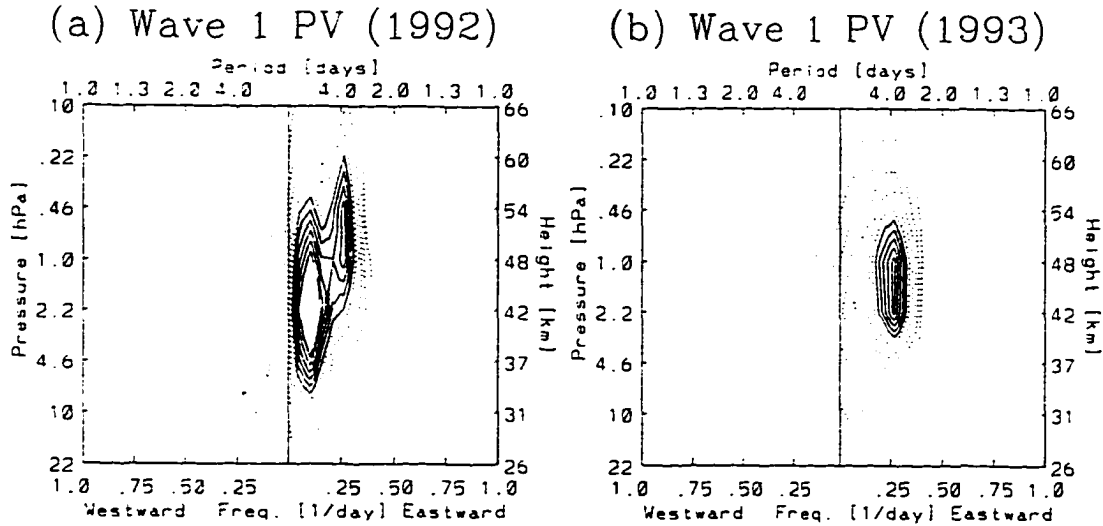
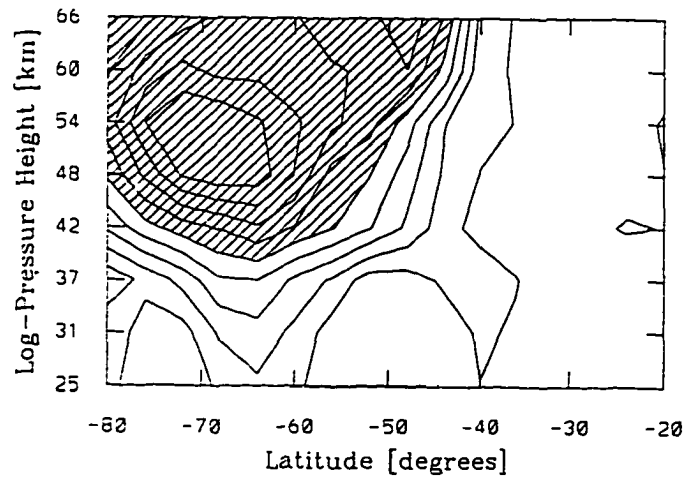


Figure 2.12 (a) East-west power spectrum for wave 1 quasigeostrophic potential vorticity derived from MLS geopotential height at 72°S for 18 August–6 September 1992. (b) Same as (a) but for 2–16 September 1993. Contours are arbitrary with solid lines representing larger values.

is centered near 50 km, 68°S. Figure 2.13b shows the wave 1, 3.75-day signal in 1993, which has a similar structure to the 1992 feature, although centered slightly lower and with contours somewhat more compact.

The three-dimensional structure of the perturbation PV resembles the “PV charge” concept discussed by Hoskins et al. (1985) and more recently by Bishop and Thorpe (1994), who considered the effects on the atmosphere of a uniform spherical quasigeostrophic PV anomaly in a basic state with constant static stability and density and in a two-layer vertical static stability basic state representing the effects of the tropopause. In this analogy, the atmosphere represents an isotropic dielectric material, static stability represents dielectric properties, geopotential (or streamfunction) represents electric potential, and an isolated PV anomaly represents an electrostatic charge, with an accompanying vector field that produces action-at-a-distance (a fundamental concept in PV thinking). This “PV field” (which is independent of static stability, density, and boundary conditions) induces perturbation temperature, geopotential, and wind fields as shown in Fig. 2.14a (for the case of constant static stability), adapted from

(a) Wave 1 PV (1992)



(b) Wave 1 PV (1993)

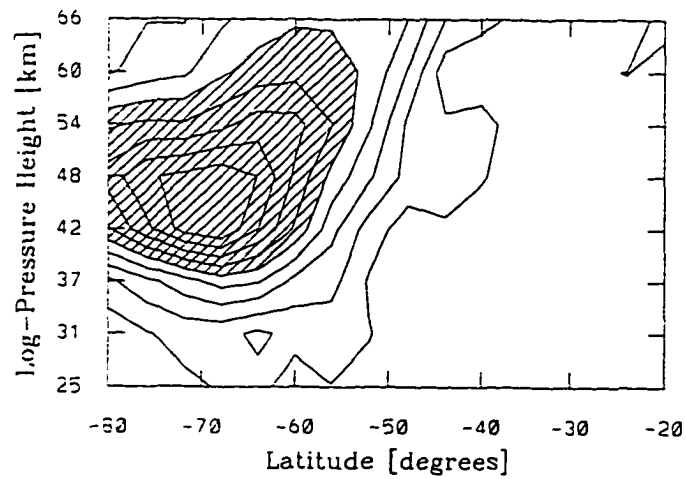
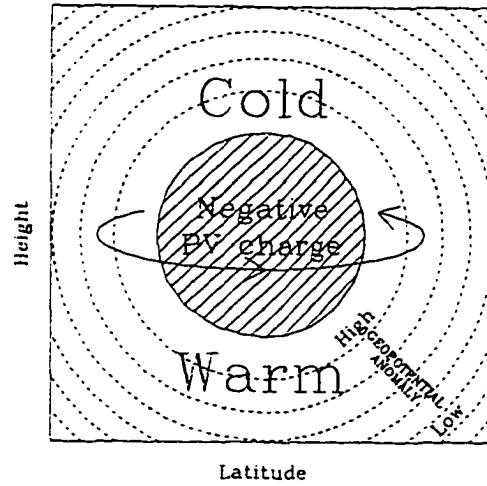


Figure 2.13 (a) Quasigeostrophic potential vorticity amplitude for wave 1 and 3.8-day eastward period for 18 August–6 September 1992. (b) Same as (a) but for 2–16 September 1993, 3.75-day period. Contours are at every 10% interval of the maximum with values higher than 50% shaded.

(a) PV Charge Schematic



(b) 1992 4-Day Wave

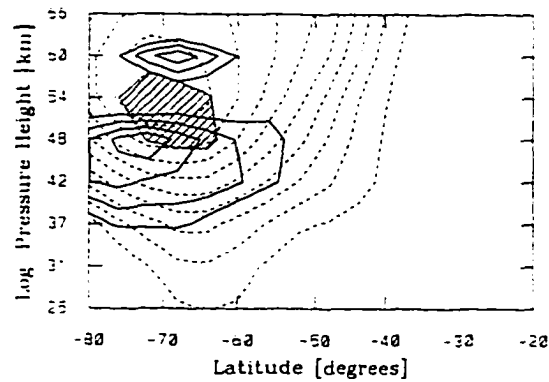


Figure 2.14 (a) “PV charge” schematic adapted from Bishop and Thorpe (1994), Figs. 1 and 2. The negative PV anomaly induces temperature, geopotential, and wind (solid line with arrows) anomalies as shown. Note: the PV, temperature, and geopotential anomalies are viewed here as a meridional cross section of the three-dimensional PV charge, while the circulation is in a horizontal plane that projects out of the page. (b) Amplitude of wave 1, 3.8-day eastward period signal from 18 August to 6 September 1992. Hatched region includes PV amplitude greater than 90% of the maximum. Solid lines are perturbation temperature amplitude of 60%–90%, incremented by 10% of the maximum. Dashed lines are perturbation geopotential amplitude at every 10% of the maximum. Adapted from Figs. 2.4a, 2.6a, and 2.13a of this paper.

Figs. 1 and 2 of Bishop and Thorpe (1994). Here a negative spherical PV charge induces a vertical temperature dipole with cold temperature perturbation on top, spherical geopotential anomaly, and anticyclonic circulation about the vertical axis. Note that circulation shown here is for the Southern Hemisphere ($f < 0$); the direction should be reversed for the Northern Hemisphere ($f > 0$).

In comparison, Fig. 2.14b shows the amplitude of the wave 1, 3.8-day period mode during the 1992 series as a function of height and latitude. The hatched region includes PV amplitude greater than 90% of the maximum. Solid lines are perturbation temperature amplitude of 60%–90% of the maximum, incremented by 10%, and the dashed lines are perturbation geopotential amplitude at every 10% of the maximum. Here we see the PV anomaly bounded above and below by two temperature lobes, which are out of phase, resembling the cold and warm perturbations in Fig. 2.14a. The geopotential anomaly surrounds the region of large PV amplitude, although centered slightly higher. There would also be an induced circulation about the vertical axis associated with the geopotential anomaly, similar to that shown in Fig. 2.14a.

This analogy suggests that the 4-day wave may be more fundamentally viewed as a PV anomaly than a temperature anomaly. The wave life cycle begins with an unstable atmosphere that allows growth in PV anomaly amplitude, which in this paradigm induces anomalies in temperature, geopotential, and wind. This view also appeals to the “wave activity” interpretation of eddy features discussed in section 4f, since PV anomalies relate directly to the EP flux divergence forcing of the zonal-mean state. The PV charge paradigm, coupled with its generation by instability mechanisms, appears to provide a satisfying physical explanation for the 4-day wave.

5. Summary

This study takes advantage of the vertical coverage and resolution of the Microwave Limb Sounder instrument to analyze 4-day wave features during August–September 1992 and 1993. Strong 4-day wave events are found during both time series. A double-peaked structure is

found in temperature with maxima in the upper stratosphere and lower mesosphere and strong vertical phase variation in between, as predicted by the model of Manney and Randel (1993). Four-day eastward period signals are also evident in MLS ozone, geopotential height, and quasigeostrophic potential vorticity derived from MLS geopotential height. The ozone signal compares well with results from a linear advective-photochemical model that calculates the ozone response to temperature and wind perturbations associated with the 4-day wave. A negative region of quasigeostrophic potential vorticity gradient coexists with positive EP flux divergence, suggesting that instability dynamics plays a role in the wave forcing. The three-dimensional wave structure is shown to resemble the potential vorticity charge concept, which includes a vertical temperature dipole and anomalies in PV, geopotential, and horizontal wind. The PV paradigm, in which temperature, geopotential, and wind anomalies are induced by a potential vorticity charge, itself the result of instability growth processes, offers an elegant and conceptually satisfying explanation of the physics of the 4-day wave.

Acknowledgements

We want to thank Dr. Jerald Ziemke for assistance in spectral computations and graphics. The paper benefited from conversations with Dr. Gloria Manney (who also provided the NCEP data) and Dr. William Randel, and helpful comments by two anonymous reviewers. Drs. R. Swinbank and A. O'Neill developed the UKMO data that we obtained from the EOS Distributed Active Archive Center (DAAC, code 902.2) at the Goddard Space Flight Center. The activities of the EOS DAAC and the *Upper Atmosphere Research Satellite* Project (code 916) are sponsored by NASA's Mission to Planet Earth Program. ISU coauthors are sponsored in part by National Aeronautics and Space Administration Grant NAG 5-2787. Work at the Jet Propulsion Laboratory, California Institute of Technology, was performed under contract with the National Aeronautics and Space Administration. Part of this work was done by D. Allen as a guest graduate student at Argonne National Laboratory.

CHAPTER 3 OBSERVATIONS OF MIDDLE ATMOSPHERE CO FROM THE UARS ISAMS DURING THE EARLY NORTHERN WINTER 1991/1992

A paper to be submitted to the Journal of Geophysical Research.

D. R. Allen¹, J. L. Stanford¹, M. A. López-Valverde², N. Nakamura³, D. J. Lary⁴,
A. R. Douglass⁵, M. C. Cerniglia⁶, F. W. Taylor⁷, J. J. Remedios⁷

Abstract

Observations of carbon monoxide in the upper stratosphere and lower mesosphere from the *Upper Atmosphere Research Satellite* Improved Stratospheric and Mesospheric Sounder (ISAMS) are presented during the dynamically active early northern winter 1991/1992. CO mixing ratios are shown to generally increase with altitude from 30 to 70 km. Large mixing ratios are found in the Arctic winter polar region due to downward advection from the mean meridional circulation. Comparison with Ertel potential vorticity shows that high CO mixing ratios saturate the winter polar vortex. A simple chemical model is used to show that the observed tropical upper stratosphere maximum is likely due largely to methane oxidation. Downward transport from thermospheric source region is shown to enhance CO in the mesosphere and upper stratosphere. ISAMS CO data are compared with CO output from the Goddard Space Flight Center 3D chemistry and transport model (CTM), initialized with ISAMS CO. ISAMS and CTM horizontal distributions are in good agreement near the stratopause, even

¹Department of Physics and Astronomy, Iowa State University, Ames, Iowa

²Instituto de Astrofísica de Andalucía (CSIC), Granada, Spain

³Department of Geophysical Sciences, University of Chicago, Chicago, IL

⁴Centre for Atmospheric Science, Cambridge University, U.K.

⁵NASA Goddard Space Flight Center, Greenbelt, MD

⁶Applied Research Corporation, Landover, MD

⁷Department of Physics, Oxford University, U.K.

during highly dynamic periods. Disagreement in the zonal mean vertical gradients occurs several weeks into the model run, with CTM mixing ratios biased high in the upper stratosphere outside the polar vortex and low in the stratospheric vortex and lower mesosphere. Modified Lagrangian mean diagnostics applied to ISAMS and CTM data provide insight into horizontal mixing processes during a merger of two anticyclones and massive vortex erosion.

1. Introduction

The major source of CO in the upper middle atmosphere (mesosphere and lower thermosphere) is CO₂ photolysis in the thermosphere (see Fig. 3.1):



CO mixing ratios generally increase with height throughout the middle atmosphere due to the thermospheric source and downward advective and diffusive flux into the mesosphere and stratosphere. Methane oxidation plays a large role in the stratospheric budget, providing a CO source that maximizes near 30 km. Although some CO molecules produced from combustion and natural sources near the surface reach the stratosphere, most are destroyed in the troposphere (Brasseur and Solomon 1986). The only major CO loss mechanism in the middle atmosphere is the reaction with OH:



which occurs during the sunlit hours, since OH is produced from photolysis reactions (e.g., with H₂O).

In the upper stratosphere and mesosphere, the photochemical lifetime of CO is on the same order (weeks to months) as vertical transport time scales and is generally larger than horizontal transport time scales (days to weeks), making it useful tracer of the atmospheric transport (Hays and Olivero 1970; Wofsy et al. 1972; Allen et al. 1981; Solomon et al. 1985). In the polar night stratosphere and mesosphere CO is conserved due to the lack of OH, making it a particularly good tracer of winter polar vortex dynamics.

Carbon Monoxide Chemistry and Transport in the Middle Atmosphere

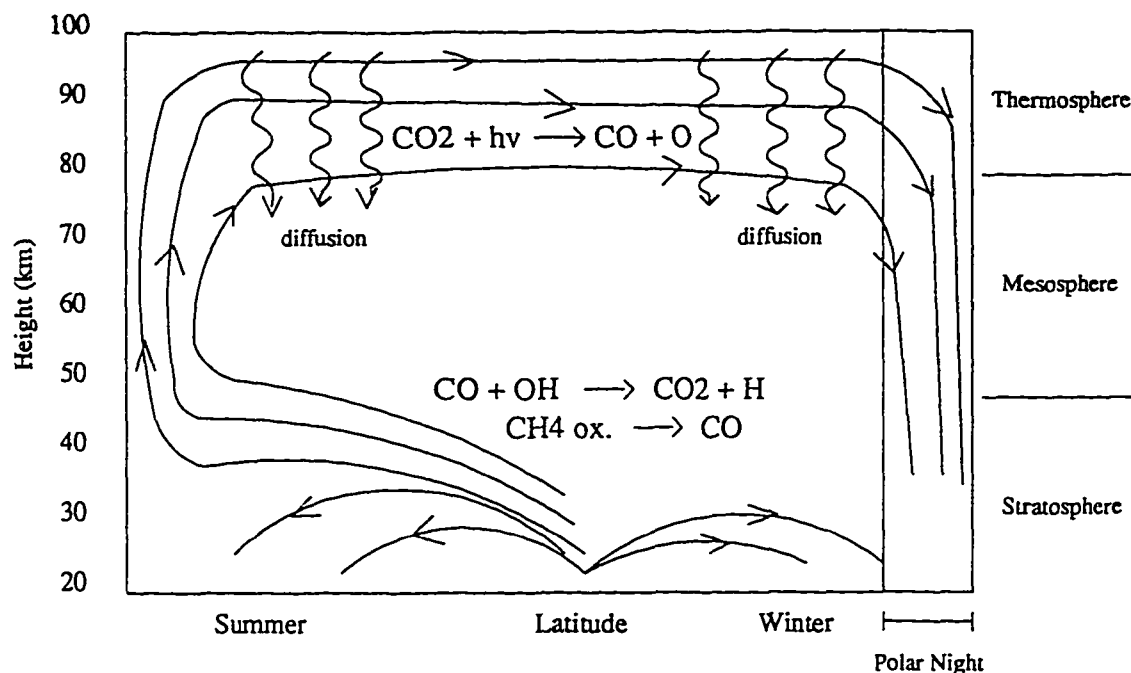


Figure 3.1 Schematic diagram of CO chemistry and transport processes in the meridional plane under solstice conditions. adapted from Solomon et al. (1985).

Early predictions of CO mixing ratio in the middle atmosphere were made by Hays and Olivero (1970) who incorporated CO and CO₂ photochemistry and vertical transport in a 1D model to calculate mixing ratio profiles from 0–200 km for two recombination regimes and three eddy diffusion formulations. They found that CO mixing ratio increases with height throughout the middle atmosphere due to CO₂ photolysis with CO mixing ratios reaching at least 30 ppmv in the thermosphere. Wofsy et al. (1972) and Wofsy (1976) furthered this work by including more complex photochemistry and quantified the importance of CO₂ photolysis, CH₄ oxidation, and loss from OH for the CO distribution.

A pioneering study of CO in the middle atmosphere by Solomon et al. (1985) used a 2D chemistry and transport model from 10 to 116 km to examine the distribution and seasonal evolution of CO. Salient points from the study include: (1) CO mixing ratios increase with height throughout most of the middle atmosphere; (2) Mesospheric CO abundances are larger

in winter than in summer due to vertical advective transport; (3) Extremely large CO mixing ratios are found in the polar night mesosphere/upper stratosphere due to diabatic descent and lack of OH, with especially sharp CO gradients occurring at the polar night terminator; (4) Midlatitudes may exhibit significant CO variability during periods of large amplitude planetary waves.

CO mixing ratios in the middle atmosphere have been previously measured by ground based microwave techniques (Waters et al. 1976; Goldsmith et al. 1979; Kunzi and Carlson 1982; Clancy et al. 1982, 1984; Bevilacqua et al. 1985; Aellig et al. 1995). These studies have shown the general tendency of CO mixing ratios to increase with altitude and become larger in the winter hemisphere and propose that chemical as well as dynamical processes such as planetary wave activity (Bevilacqua et al. 1985), gravity wave activity (Aellig et al. 1995), vertical and horizontal mixing, and interhemispheric circulations in the middle atmosphere, contribute to large CO variability on time scales of days to years.

Satellite observations of infrared CO emission by the Stratospheric and Mesospheric Sounder (SAMS) instrument on board NIMBUS 7 were obtained from the fundamental vibrational-rotational band at $4.6\ \mu\text{m}$ (Murphy 1985). The SAMS CO indicated large variability with altitude, latitude, and time in the middle atmosphere, as expected from model predictions (Solomon et al. 1985). CO measurements in the middle atmosphere have also been made by infrared occultation instruments on various shuttle missions (Girard et al. 1988; Gunson et al. 1990; Gunson et al. 1996; Chang et al. 1996).

This study examines CO obtained from the Improved Stratospheric and Mesospheric Sounder (ISAMS) on board the *Upper Atmosphere Research Satellite (UARS)*. This platform provides nearly global coverage with good vertical resolution to examine the CO distribution from approximately 10 to 0.03 hPa (roughly 30 to 70 km). Preliminary zonal mean maps of ISAMS CO were presented in López-Valverde et al. (1993) and a more detailed discussion of the seasonal zonal mean evolution was described in López-Valverde et al. (1996). The present study examines in detail the ISAMS CO distribution and evolution during the early northern winter 1991/1992. Salient features include the following: (1) Generally increasing CO mixing

ratio with altitude from 30 to 70 km: (2) Large CO concentrations in the Arctic polar region due to downward advection from the mean meridional circulation: (3) Persistent tropical upper stratospheric maximum likely due largely to CH₄ oxidation: (4) Significant horizontal variability in the upper stratosphere during periods of large planetary wave activity.

ISAMS CO data are compared with output from the Goddard Space Flight Center (GSFC) 3D Chemistry and Transport Model (CTM), initialized on 8 December 1991 with ISAMS CO observations, and driven by the GSFC Data Assimilation Office (DAO) assimilated wind fields. Horizontal maps of ISAMS and CTM CO compare favorably near the stratopause, even during highly dynamic events, while differing vertical gradients result in much larger ISAMS CO mixing ratios in the lower mesosphere and stratospheric polar vortex in January 1992. Mixing processes accompanying large planetary wave events in January 1992 are analyzed with novel modified Lagrangian mean (MLM) diagnostics applied both to ISAMS and CTM data.

2. Data description

This study examines retrieved CO data from the ISAMS, one of the ten *UARS* instruments. ISAMS measures the CO concentration in the upper stratosphere and mesosphere by detecting infrared limb emission from the vibrational-rotational band near 4.6 μm . The CO signal is contaminated by emissions from other constituents, mainly N₂O, CO₂, and O₃. Although pressure modulation techniques (see Taylor et al. 1993) help to discriminate between closely spaced or overlapping emission lines, contamination is still a major concern in the CO retrieval.

Another difficulty in the retrieval is that CO is in non-local thermodynamic equilibrium (non-LTE) in most of the middle atmosphere (López-Valverde et al. 1991; López-Puertas et al. 1993). In non-LTE conditions thermodynamic equilibrium is not met and therefore the population of the emitting level does not follow the Boltzmann distribution. In this case the source function for the given transition must be used in the retrieval rather than the Planck function. The non-LTE model used in the ISAMS retrieval is described by López-Puertas et al. (1993) and López-Valverde et al. (1996).

ISAMS CO retrievals are performed from approximately 10 to 0.03 hPa. At pressures

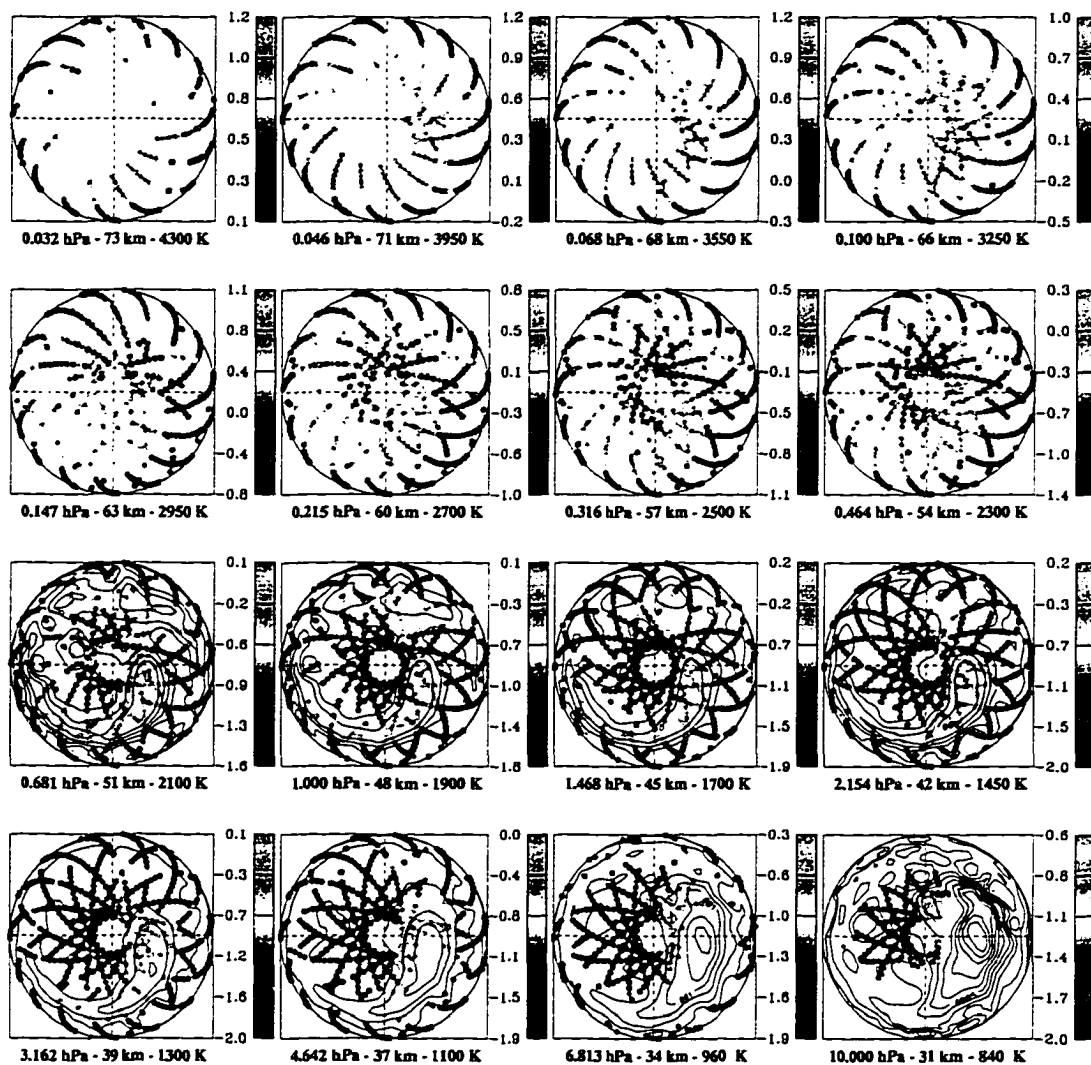
higher than 10 hPa the signal is significantly contaminated by Pinatubo aerosols. The criteria used for judging the quality of the retrieved measurement is the ratio of the retrieved variances to the a priori variances. When this ratio exceeds 2 the data quality (denoted QUAL here) is flagged by setting it negative. At this point, the data contain as much information from the measurements as from the a priori climatology, which for version 12 ISAMS CO is a seasonally varying zonal mean field, derived from a blended data set of GSFC 2D model output and version 10 ISAMS CO.

This study uses level 2 and level 3AT CO from ISAMS processing version 12. Version 12 CO has several improvements over the previously validated version 10 (see López-Valverde et al. 1996), including in-line non-LTE source function calculation rather than tabulated source function and use of ISAMS N₂O to remove contamination rather than a 2D climatology. Level 2 refers to the first retrieved data product arranged as consecutive vertical profiles, which are positioned along the satellite limb track at regular time intervals, but irregularly spaced in the vertical. Level 3AT is a standard *UARS* format produced by interpolating level 2 data horizontally along the limb track to equally spaced times (~ 65 s) and vertically to standard *UARS* pressure surfaces. ISAMS measures with twice the horizontal sampling rate of the level 3AT output, so the interpolation from level 2 to level 3AT involves a roughly 50% decrease in the horizontal resolution.

Figure 3.2 provides the distribution of good quality CO retrieval points for 12 January 1992, along with Ertel potential vorticity derived from National Centers for Environmental Prediction (NCEP) meteorological analyses at 8 nearby potential temperature surfaces (data provided by G. Manney). Here level 3AT data in the Northern Hemisphere are plotted at 16 pressure levels from 10 to 0.032 hPa. Each shaded circle marks one level 3AT measurement with the shade representing the Log_{10} of the CO mixing ratio in ppmv. Data flagged with negative QUAL are not plotted, resulting in gaps in Fig. 3.2. For example, in part of the displaced polar vortex (as identified by the PV contours) at 4.6 hPa the CO data are flagged as “poor,” even though CO mixing ratios in the polar vortex are expected to be large (as will be explained later) and therefore may be expected to provide sufficient radiance to make a reliable

Figure 3.2 Version 12 ISAMS CO at 16 pressure levels on 12 January 1992. Each shaded circle represents one observation on the *UARS* level 3AT grid. The color bar (in greyscale) for each level is the Log_{10} of the CO mixing ratio in ppmv. Data flagged as “poor” by the retrieval are not included in the plot. The lowest eight levels are overlaid by contours of NCEP-derived PV on the potential temperature surfaces indicated. Nominal altitudes are provided for each pressure level. Projection is orthographic with 0° (180°) longitude on the right (left) side.

Version 12 ISAMS L3AT DATA -- Log10 of CO vmr in ppmv
12 January 1992



measurement. However, by comparing these plots with ISAMS temperature distributions (not shown here) it was found that a strong zonally asymmetric temperature pattern is present with a maximum displaced slightly west (clockwise) of the vortex maximum near 0° longitude. It is likely that the low temperatures offset the high CO mixing ratios, making the radiance measured in this region by ISAMS too small to make an accurate retrieval. Large regions of poor data are found above 0.1 hPa due to excessive noise in the measured radiances. Only limited nighttime data are available in the mesosphere, while solar non-LTE pumping allows for reliable daytime mesospheric retrievals (López-Valverde et al. 1996).

Gridded ISAMS CO used in this study were produced from level 2 data by first interpolating vertically in log pressure coordinates at each latitude/longitude point to a given pressure grid (the same grid used by the CTM discussed below). At each pressure level the data were interpolated horizontally to a 2° latitude by 5° longitude grid using a triangular interpolation routine. To ensure nearly hemispheric coverage of gridded CO, all data were used in the gridding, even data flagged as “poor.” A comparison of zonal mean maps made with and without data flagged by negative QUAL show only small differences, none of which affect any of the conclusions made in this paper. This procedure also does not adversely affect the horizontal maps presented in this paper at 1.0 hPa, since most of the data points at that pressure have positive QUAL (see Fig. 3.2). Regions of missing data (largely 80° to 90° N, beyond the viewing geometry of *UARS*) were filled with CTM CO scaled by the ratio of the zonal mean ISAMS CO to CTM CO at 78° N. A 9-point (3 by 3) smoothing was applied to the subsequent data both to ease the transition from ISAMS to CTM CO at 80° N and to reduce random variability from instrument noise.

3. Model description

This study compares ISAMS CO with CO distributions simulated by the GSFC 3D CTM [see Douglass et al. (1996) and accompanying references.] The CTM was initialized with CO, N_2O , and CH_4 on 8 December 1991 using a PV/potential temperature mapping scheme (Lary et al. 1995) incorporating meteorological data from the GSFC data assimilation office (DAO)

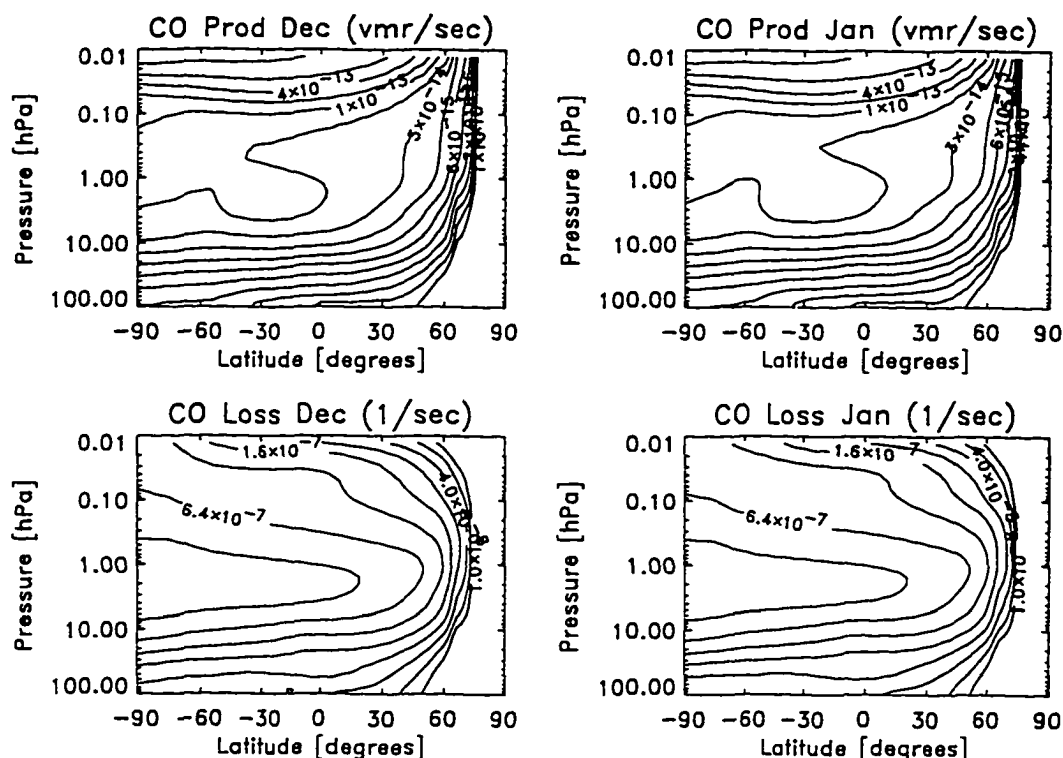


Figure 3.3 The CO production and loss terms used for the GSFC 3D CTM run analyzed in this study. The files are monthly and zonal means for December 1991 and January 1992.

along with ISAMS CO and Cryogenic Limb Array Etalon Spectrometer N_2O and CH_4 . The winds and temperatures used in this calculation are taken from an updated version of the assimilation which includes 70 sigma levels from the surface to 0.01 hPa. Numerical transport within the CTM is calculated using the piecewise-parabolic scheme of Lin and Rood (1996). A monthly mean parameterization of photochemical loss from the GSFC 2D model (Jackman et al. 1996) was used for CO, N_2O , and CH_4 , and monthly mean production was used for CO (see Fig. 3.3 for model CO photochemistry). In addition, a passive tracer was introduced that was initialized identically to CO. The model run was from 8 December 1991 to 18 January 1992, with output once per day at 00 UTC on a 2° latitude by 2.5° longitude grid.

4. Analysis techniques: PV-mapping and MLM diagnostics

A fundamental shift in descriptions of atmospheric dynamics is occurring as Lagrangian analyses are replacing conventional Eulerian analyses. This shift has been facilitated by the production of relatively high-resolution isentropic potential vorticity (PV) maps. A technique, denoted here as “PV-mapping,” is becoming an increasingly popular diagnostic tool for analyzing atmospheric chemical transport. PV-mapping involves averaging constituent mixing ratios along PV contours on isentropic surfaces (i.e. surfaces of constant potential temperature, θ) to produce 2D maps in PV and θ coordinates. This procedure effectively filters out reversible (and resolvable) wave motions that can cause confusion in zonal mean analyses. PV-mapping has proved to be quite useful for analyzing constituent transport, especially in the polar stratosphere, and for constructing constituent distributions from limited observations (e.g., Schoeberl et al. 1989).

PV-mapping basically involves a transformation of the tracer continuity equation to conservative coordinates (Schoeberl and Lait 1991). Potential temperature is chosen as the vertical coordinate, and PV, which is conserved for adiabatic, frictionless motion, is used in the horizontal. To the extent that both the constituent mixing ratio and PV are conserved, the two quantities will maintain a close correlation. As non-conservative processes (diabatic heating, friction, mixing, or photochemical effects) become important, the close correlation will be lost. For the PV-mapping in this study, PV on isentropic surfaces, derived from U. K. Meteorological Office (UKMO) meteorological analyses, is first converted to equivalent latitude, the latitude of a zonal circle centered at the pole that encompasses the same area as a given PV contour (see Lary et al. 1995). The equivalent latitude is then interpolated to the (longitude, latitude, pressure) locations of the ISAMS level 2 output. Similarly, potential temperature is calculated from UKMO data and interpolated to the ISAMS level 2 output locations. This results in a series of points of the form (equivalent latitude, potential temperature, CO mixing ratio). The mixing ratios were then binned every 5° in equivalent latitude and 50° K in potential temperature, averaged, and smoothed with a 9 point (3 by 3) filter to further remove instrument noise. To avoid errors from climatological bias and day/night differences, only day-

time data with $QUAL > 0$ were used in the PV-mapping. The resulting map for 12 January 1992 is examined in section 5a.

The effects of non-conservative processes on tracer transport are also explored in this study using novel Lagrangian mean techniques. The modified Lagrangian mean theory, which originated with McIntyre (1980), has been re-formulated (Nakamura 1996, 1997) to include isentropic diffusion and diabatic heating. (Nakamura's formulation is denoted MLM here to distinguish from PV-mapping, which is also a Lagrangian mean technique). In MLM, the mass enclosed by tracer contours is used rather than PV to diagnose tracer transport. Non-conservative processes (largely isentropic mixing and diabatic heating for long-lived tracers) "advect" tracer mixing ratios across isolines of the mass coordinate, or equivalently, "advect" mass across tracer contours.

The MLM diagnostic derivation (here we exclude diabatic effects) starts with the simple horizontal advection-diffusion equation for the tracer mixing ratio χ :

$$\frac{\partial \chi}{\partial t} + J(\Psi, \chi) = D \nabla^2 \chi \quad (3.3)$$

where Ψ is the streamfunction, J is the Jacobian, and ∇^2 is the Laplacian. This derivation assumes a constant microscale diffusion coefficient D and nondivergent horizontal winds (a good approximation for the stratosphere). Next an area operator $AREA(\beta, \chi, t)$ is defined as the integral of the quantity β over the area bounded by a given tracer contour with mixing ratio χ at time t . When this operator is applied to each term in Eq.(3.3) the resulting MLM tracer continuity equation results:

$$\frac{\partial}{\partial t} \chi(A, t) = D \frac{\partial}{\partial A} \left(L_\epsilon^2 \frac{\partial \chi}{\partial A} \right) \quad (3.4)$$

$$L_\epsilon^2(A, t) = \langle |\nabla \chi|^2 \rangle (\partial \chi / \partial A)^{-2}, \quad (3.5)$$

where the angle brackets denote the average around a given tracer contour, and A is the area enclosed by that contour, $A(\chi, t) = AREA(1, \chi, t)$. Isentropic diffusion is characterized in MLM by L_ϵ^2 , or "equivalent length," which is a measure of the "scrambledness" of tracer contours. The quantity $D L_\epsilon^2$ acts as an effective horizontal diffusivity in the MLM framework so that minima in equivalent length correspond to mixing barriers while maxima occur in

regions of large horizontal mixing. In this study we use a normalized equivalent length (ξ) defined by:

$$\xi = \text{Ln}(L_e^2/L_o^2) \quad (3.6)$$

where $L_o = 2\pi a \cos \phi_e$ is the length of the contour that surrounds a pole-centered circle at latitude ϕ_e , the equivalent latitude defined by $A(\lambda, t) = 2\pi a^2(1 - \sin \phi_e)$, where a is the earth's radius. Section 5e analyzes barrier evolution and horizontal mixing that occur during large wave events in January 1992 by applying MLM diagnostics to ISAMS and CTM data in the upper stratosphere and lower mesosphere.

5. Results

a. Meridional structure

The map of ISAMS CO for 12 January 1992 (Fig. 3.4a), constructed using the PV-mapping technique described in the previous section, provides a wealth of information about the transport and chemistry of CO in the middle atmosphere. Mixing ratios generally increase with potential temperature except from 30°N to 30°S equivalent latitude, below 1800 K (note: the Log_{10} of the mixing ratio in ppmv is plotted in Fig. 3.4). Winter polar descent, bringing CO-rich air downward, is shown by the high CO mixing ratios poleward of 50°N equivalent latitude. The CO mixing ratio increases by an order of magnitude between 40° and 80°N equivalent latitude over the potential temperature range 1000 to 1800 K. The large mesospheric CO mixing ratios appear to reach 1000 K (~ 35 km). There are few observations below 1000 K, and therefore the sharp vertical gradient at high equivalent latitudes between 800 and 1000 K does not denote the lower boundary of diabatic descent.

CO mixing ratios decrease from high to low northern equivalent latitudes in the mesosphere (above ~ 1900 K) while in the stratosphere near 1500 K minima are found near 20°N and 30°S equivalent latitude with a local maximum near 5°S. This feature persists without much change throughout November and December 1991 and January 1992. A similar map of N₂O (Fig. 3.4b) displays monotonically increasing mixing ratios from high to low equivalent latitudes as expected for a long-lived tracer with tropospheric source advected by the mean meridional

(a) PV-Mapping of V12 ISAMS CO for 12 January 1992 (Log of vmr in ppmv)

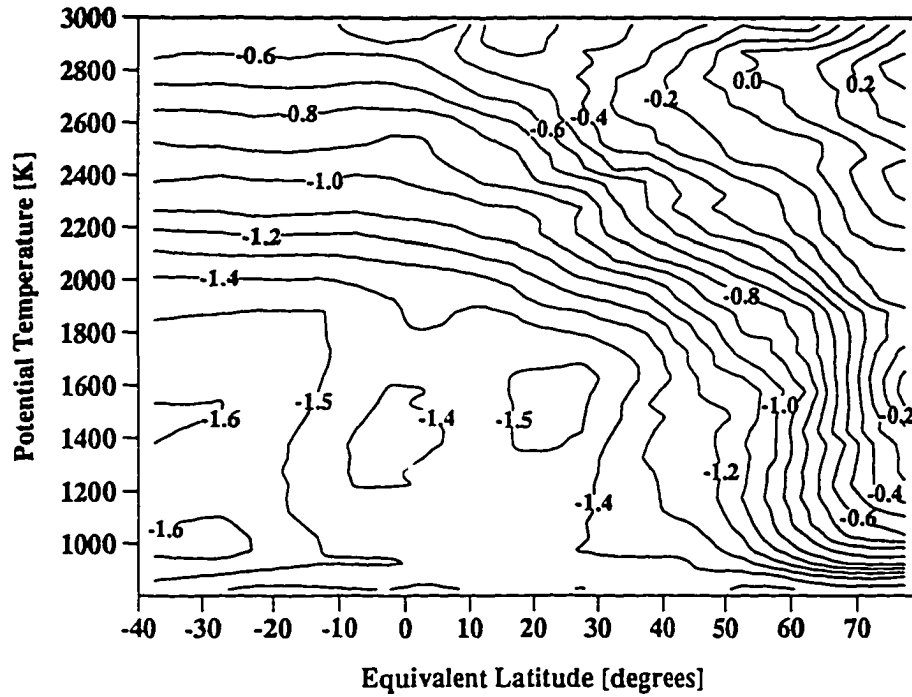
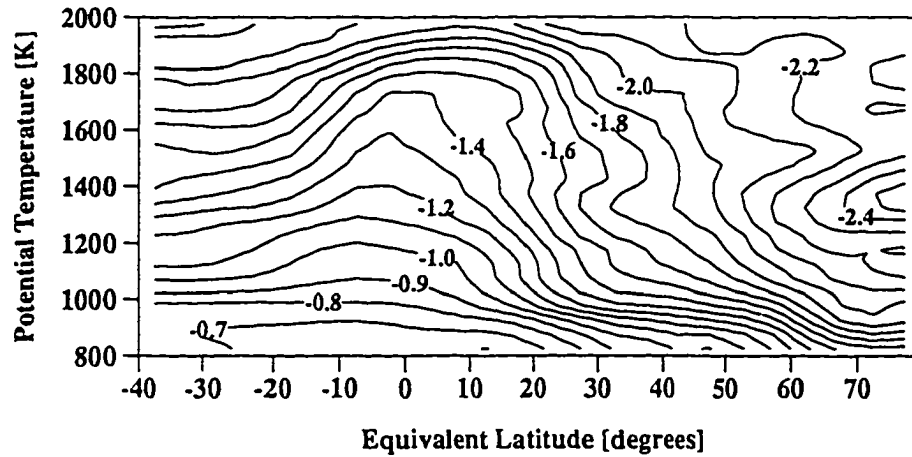
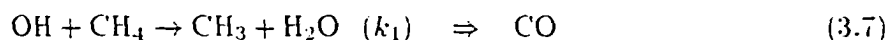
(b) PV-Mapping of V12 ISAMS N₂O for 12 January 1992 (Log of vmr in ppmv)

Figure 3.4 (a) Potential vorticity (in equivalent latitude coordinates)-potential temperature map of ISAMS CO for 12 January 1992. made with UKMO temperatures and UKMO-derived PV. Only daytime data with good quality (as identified by the quality factor in the retrieval) were used in this analysis. Units are Log_{10} of the mixing ratio in ppmv. (b) Same as (a) but for ISAMS N₂O [note the difference in extent of the vertical scales in (a) and (b).]

circulation. The contrast between CO and N₂O suggests that chemistry is likely affecting the tropical CO distribution. Section 5b examines this feature in detail, arguing that the low latitude CO maximum is likely due largely to methane oxidation.

b. Evidence of CH₄ oxidation in the upper stratosphere

The amount of CO produced from CH₄ oxidation in the upper stratosphere can be estimated by assuming a first order balance between the following two reactions:



Here we assume efficient conversion from CH₄ to CO in the upper stratosphere through the rate limiting reaction given in Eq.(3.7). Equations (3.7) and (3.8) represent one source and one sink of CO, which if balanced, provide the CH₄/CO ratio:

$$\frac{[\text{CH}_4]}{[\text{CO}]} = \frac{k_2}{k_1}. \quad (3.9)$$

Figure 3.5a shows the observed zonal mean CH₄/CO ratio in the upper stratosphere from 30°S to 30°N for 1 January 1992 as calculated from ISAMS version 12 data, while Fig. 3.5b shows the predicted ratio from Eq.(3.9) using reaction rates from DeMore et al. (1992) and temperatures from the DAO assimilation. The observed and predicted ratios show similar slope structure from 5 to 2 hPa for the region 30°S to the equator. North of 10°N, the observed ratio decreases rapidly with latitude while the predicted ratio remains nearly constant with latitude from 10°S to 30°N. The Northern Hemisphere discrepancy is likely related to the downward transport of CO-rich air into the winter mesosphere and stratosphere, combined with large meridional excursions of vortex air to low latitudes observed on this day (see Fig. 3.11a). Since the CO mixing ratio varies by an order of magnitude inside and outside the vortex, even localized regions of vortex air can cause large perturbations in the zonal mean CO. The very large ISAMS CH₄/CO ratios observed near 10 hPa are likely influenced significantly by aerosol contamination of both the CO and CH₄ ISAMS channels (López-Valverde et al. 1996; Remedios et al. 1996). Above 2 hPa the observed ratio decreases more rapidly with altitude

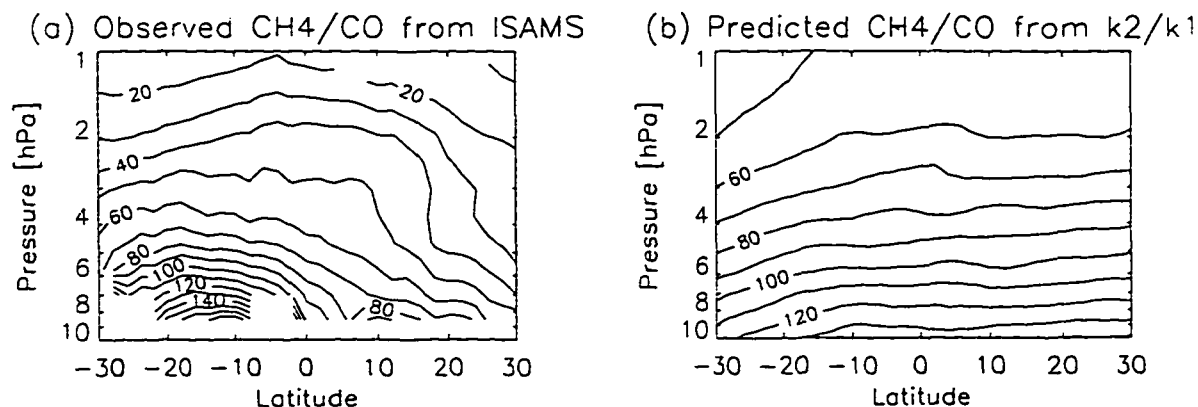


Figure 3.5 (a) Zonal mean CH_4/CO ratio as observed from ISAMS version 12 data for 1 January 1992. ISAMS level 2 were gridded using a triangulation scheme and the resulting zonal mean was taken for CH_4 and CO . (b) The predicted CH_4/CO ratio for 1 January 1992 as calculated from Eq.(3.9) using reaction rates from DeMore et al. (1992) and temperatures from the GSFC DAO assimilation (see text).

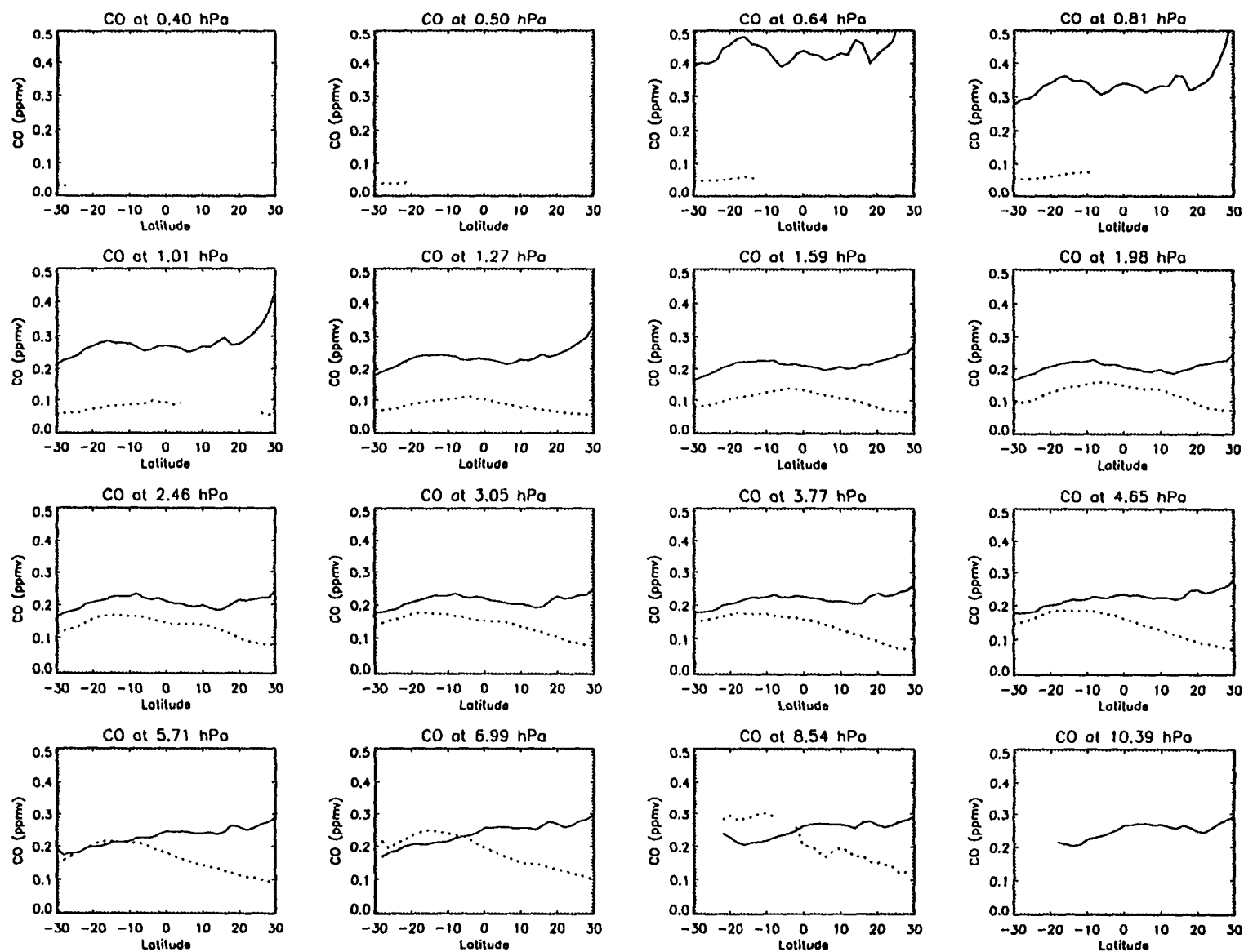
Remedios et al. 1996). Above 2 hPa the observed ratio decreases more rapidly with altitude than the predicted ratio. This is due to the increasing effect of CO_2 photolysis on the CO budget, as described below.

Equation (3.9) can be rearranged to calculate the expected CO contribution from the CH_4 oxidation alone:

$$[\text{CO}] = \frac{k_1}{k_2} [\text{CH}_4] \quad (3.10)$$

The zonal mean ISAMS CO mixing ratio (solid line) and that calculated from Eq.(3.10) (dashed) using version 12 ISAMS CH_4 are shown in Fig. 3.6 for sixteen pressure levels on 1 January 1992. In the southern tropical latitudes at 8.54 and 6.99 hPa the predicted CO mixing ratio is larger than the observed ratio (which as mentioned may be affected by aerosol contamination at these pressure levels). From 7 to 2 hPa there is fairly good (better than 50%) agreement in magnitude between the observed and predicted CO from 30°S to the equator with both showing a clear maximum near 10°S from 3.77 to 1.98 hPa. A similar feature can be seen in Fig. 2 of Solomon et al. (1985) where the modeled Northern Hemisphere winter solstice CO distribution at 74 km exhibits a local maximum at 20°S. The meridional solstice distribution

Figure 3.6 Observed zonal mean ISAMS version 12 CO (solid) and CO predicted from CH₄ oxidation alone [dashed, from Eq.(3.10)] at 16 pressure levels for 1 January 1992.



cation is difficult from their plot due to widely-spaced contours in the tropical stratosphere. The CO production term used in the GSFC CTM (see Fig. 3.3 of this paper) shows a low latitude maximum, again suggesting that this feature is largely due to photochemical processes. Indeed, a passive tracer initialized in the CTM with a similar distribution to ISAMS CO on 8 December 1991 shows no distinguishable tropical maximum on 1 January 1992.

At altitudes above 2 hPa the observed CO increases rapidly with height, while the predicted CO decreases. This is due to the increased influence of CO₂ photolysis and decreasing contribution from CH₄ oxidation. Reaction rates in Allen et al. (1981) show that above ~ 55 km (~ 0.4 hPa), the primary source of CO is from CO₂ photodissociation, while at the stratopause (~ 50 km or ~ 1 hPa) and below, methane oxidation dominates. Since the observed CO mixing ratio at 1 hPa is roughly three times larger than that predicted from methane oxidation, even though methane oxidation is expected to be the dominant source, it is likely that vertical diffusion from higher altitudes accounts for the increased CO abundance. Although CO₂ photodissociation maximizes in the thermosphere, the present analyses suggest that the weaker source in the mesosphere/stratosphere combined with vertical diffusion downward from the thermosphere affects the CO mixing ratio strongly at altitudes above about 2 hPa.

The influence of vortex excursions and/or horizontal mixing of CO-rich vortex air to low latitudes is found to extend to at least 10°N from 3 to 1 hPa, where the shape of the observed CO mixing ratio differs from the monotonically decreasing CO mixing ratio predicted from CH₄ oxidation alone. Northward of 30°N (not shown here) the observed CO mixing ratio increases rapidly toward the pole while the predicted value from CH₄ oxidation decreases monotonically. The deviations of observed CO from that predicted by CH₄ oxidation alone thus provides valuable information about vertical mixing in the upper stratosphere/lower mesosphere, the CO contribution from CO₂ photolysis, and the horizontal transport of vortex air to the tropics.

c. Merger of two anticyclones and strong warming from 1–16 January 1992

The early northern winter stratosphere 1991/1992 has been the subject of several observational and modeling studies. Rosier et al. (1994) examined the dynamical evolution of this

period using ISAMS temperatures and derived winds and potential vorticity: O'Neill et al. (1994) used the UKMO data assimilation to study the Northern Hemisphere circulation during this winter; Ruth et al. (1994) examined tracer transport with ISAMS N_2O data; Sutton et al. (1994) applied Lagrangian trajectory calculations to study fine scale mixing. Before further scrutinizing this period with ISAMS and CTM data we present a brief meteorological overview of the mid-stratosphere during the early northern winter 1991/92, described in further detail by Ruth et al. (1994) and O'Neill et al. (1994).

From late October to late November winter westerlies exist throughout the extratropical Northern Hemisphere stratosphere, strengthening steadily with time. Two periods of growth and decay of the Aleutian high (centered near the international date line) occur in early to mid-November. Around 26 November the vortex splits into two branches that surround the Aleutian high, accompanied by a tongue of high latitude air pulled off the vortex southward of the high. The two branches of the jet recombine by 5 December as the high decays leaving a cold westerly vortex that encloses the pole.

December 1991 to mid-January 1992 are marked by three warming events accompanied by large incursions of low latitude air penetrating to high latitudes and tongues of polar vortex air peeling off, stretching, and mixing in low latitudes. The most significant event occurred in mid-January when an anticyclonic vortex, originating near the Greenwich Meridian, was advected eastward and merged with the persistent Aleutian high, forming an intense anticyclone that completely pushed the vortex off the pole and weakened it considerably. Here we provide a synoptic view of this vortex merger at 1.0 hPa (near 50 km) in ISAMS and GSFC CTM CO.

Figure 3.7 shows ISAMS CO at 1.0 hPa (shaded contours) overlaid with NCEP-derived PV data at 1900 K (solid line contours) for 1–12 January 1992, and Fig. 3.8 shows CTM CO (near 1 hPa) for the same period. On 1 January the vortex (defined by large values of PV and CO) is centered nearly over the pole and slightly elongated on the 30° – 210° longitude axis. A tongue of vortex air is stretched along approximately the 30°N latitude from 180° to 90°E . This tongue elongates further over the next four days while a tongue of low latitude, low CO mixing ratio air encroaches from near 90°E (see dark region near 100°E , 50°N on 2

Figure 3.7 Lambert equal area projections of gridded ISAMS version 12 CO at 1.01 hPa for 1–12 January 1992, overlaid with contours of NCEP-derived PV at 1900 K [PV contours are at 0.006, 0.010, 0.014, 0.018, and 0.024 K m²/(kg s).] The grid provided on 1 January has latitude circles at 0°, 30°, and 60°N, and longitudes are indicated for every 90°.

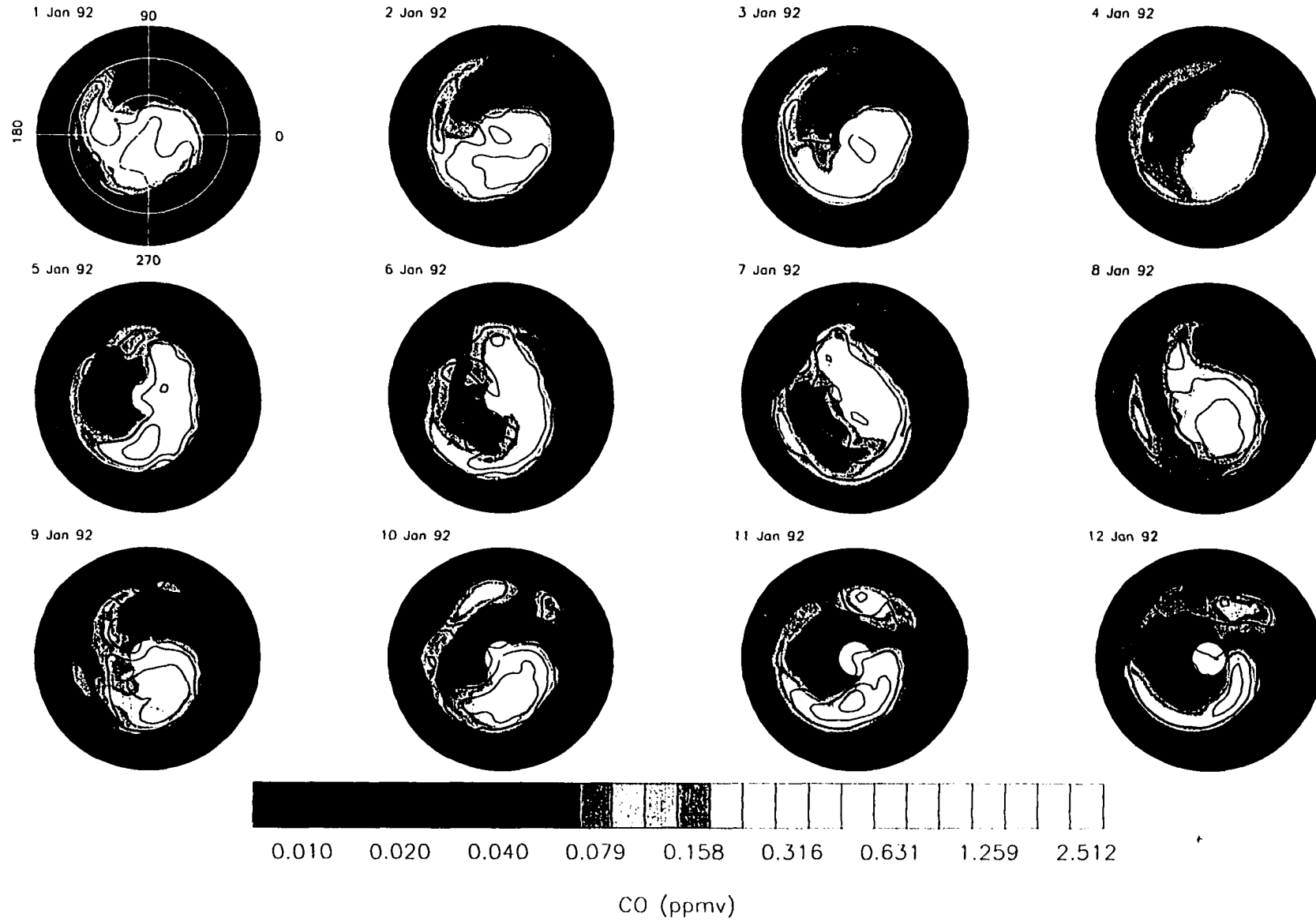
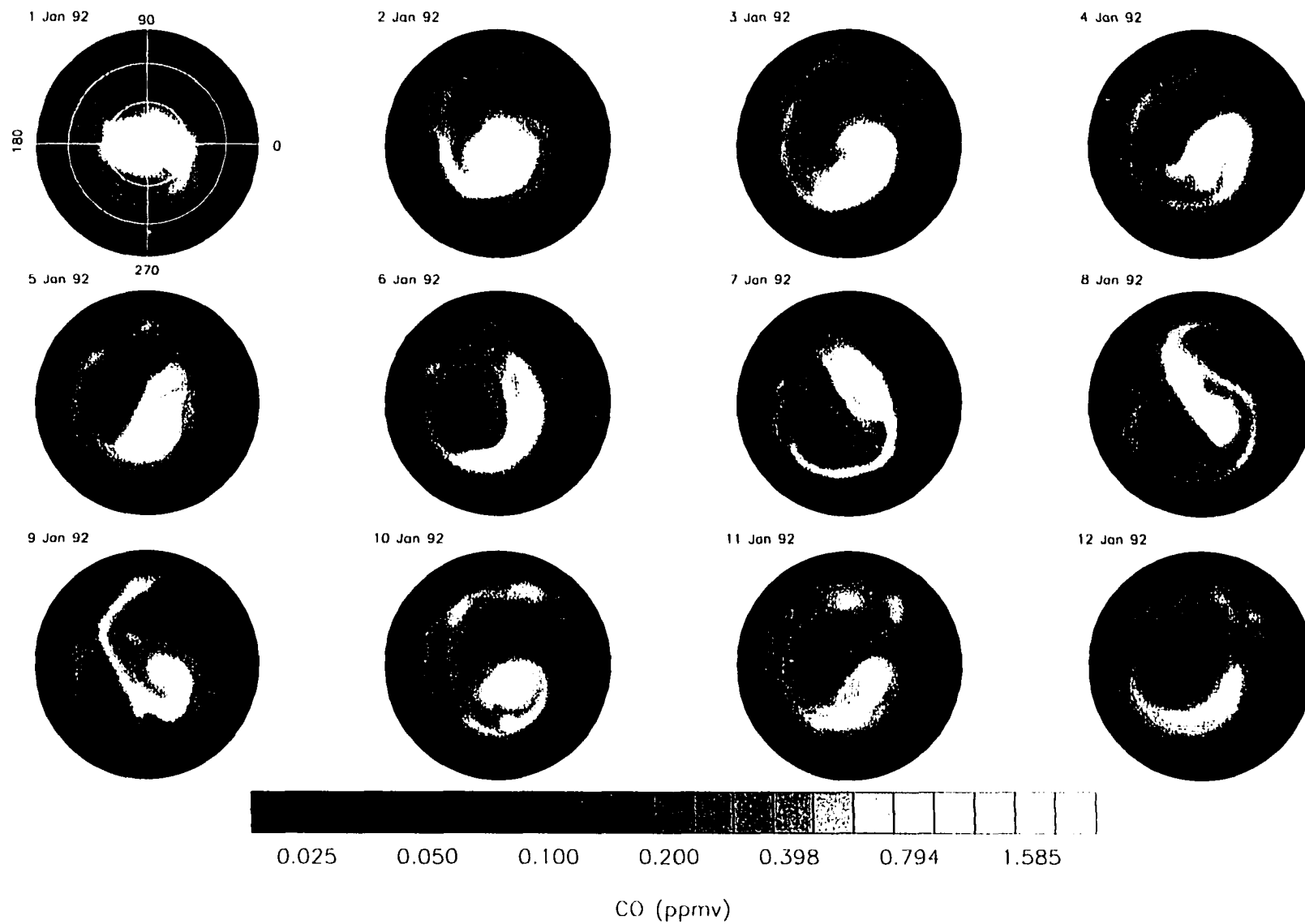


Figure 3.8 Synoptic maps of GSFC 3D CTM CO at 1.01 hPa for 1–16 January 1992. Projection is identical to Fig. 7.



January, Fig. 3.7). This feature is most prominent on 3–4 January when the vortex exhibits a “comma” shape with main cell and extending tail of high PV and CO, resolved clearly in both ISAMS and CTM CO. Concurrently, the Aleutian high (near 180°) is growing rapidly and by 6 January is quite strong. Both ISAMS and CTM CO on 6 January show this feature as a region of low CO mixing ratio surrounded by a ring of high CO vortex air. By this time the vortex “tail” has nearly re-connected with the main vortex cell near 120°E .

O'Neill et al. (1994) explain that on 6 January another anticyclone, apparent in UKMO wind fields, is beginning to form near 30°N , 30°E , apparent in UKMO wind fields. This feature moves eastward over the next two days and by 8 January is centered near 70°E . The effects of this anticyclone on CO are observed by ISAMS and the CTM on 8 January as the counterclockwise winds begin to pull a tongue of CO-rich air off the main vortex near 30°N , 90°E . This tongue elongates from 9–11 January as the traveling anticyclone moves further eastward, advecting CO-rich air to the south, while the Aleutian high is drawn into a thin tongue that partly mixes with the now dominant traveling anticyclone; this vortex decay is captured quite well by the model (see Fig. 3.8, 8–11 January), but is not resolvable by ISAMS after 8 January (see Fig. 3.7). The horizontal structure on 12 January resembles that of 6 January, with a comma shaped main vortex cell completely displaced off the pole and a strong Aleutian anticyclone surrounded by a ring of vortex air. By 12 January the vortex area has been reduced significantly as evidenced by the diminished regions of high ISAMS CO mixing ratios (compare bright regions of Fig. 3.7 for 1 and 12 January). The period from 13–16 January (not shown here) involved rapid mixing and vortex erosion that produced a highly irregular state on 16 January with nearly indistinguishable vortex. A more detailed analysis of mixing processes accompanying these events is provided in section 5e, where novel mixing diagnostics are applied to ISAMS and CTM data.

O'Neill et al. (1994) applied high resolution trajectory methods to elucidate mixing accompanying the vortex merger. They showed that a portion of the air that constitutes the Aleutian high on 8 January was drawn into the traveling anticyclone while another portion was drawn eastward along the southern boundary of the displaced main vortex. The latter

effect is clearly resolved in the CTM CO on 10 January: note the dark region near 30°N , 180° to 270° longitude in Fig. 3.8, while ISAMS (Fig. 3.7) is not able to resolve this feature. The ISAMS CO distribution at 1 hPa, however, does agree well with the major large-scale features observed in the CTM CO during this period (more below). The trajectory analysis of O'Neill et al. (1994) interestingly revealed that the strong anticyclone on 12 January is actually composed of particles that originated from three distinct vortices: the Aleutian high, the traveling anticyclone, and the polar vortex.

Another interesting analysis of this time period (Sutton et al. 1994) used Lagrangian trajectory techniques to make high resolution tracer fields from low resolution satellite observations. By applying a five-day back trajectory (or reverse domain fill, RDF) they constructed 1150 K N_2O fields at high resolution for 7–12 January. The RDF analyses revealed active mixing from middle to low latitudes and vice versa during January, while in the satellite data much of the fine-scale structure was obscured and therefore information on mixing was limited. The anticyclone merger from 9–12 January was shown by the trajectory analysis to be accompanied by intrusions of low latitude air that could not be resolved in ISAMS N_2O .

d. Comparison of ISAMS and CTM CO

A cursory comparison between ISAMS and CTM CO was made in the previous section by examining the January vortex merger in ISAMS (Fig. 3.7) and CTM (Fig. 3.8) CO at 1 hPa. A qualitative look at the two figures reveals the ability of both model and observations to resolve the large-scale features involved in the vortex evolution. This section compares in more detail horizontal distributions of ISAMS and CTM CO several weeks into the model run. Good correlation between the two would suggest both that the ISAMS CO data provide a reliable picture of the actual CO distribution and that the CTM is accurately modeling the atmospheric transport and chemistry during this period. Where the two distributions diverge, one must question the observations or the model or both. Comparing ISAMS CO with modeled CO is important for validation purposes since the availability of correlative observations is limited. López-Valverde et al. (1996) used comparisons with 2D and 3D models to aid in the validation

of version 10 ISAMS CO.

Figure 3.9 compares ISAMS and CTM CO for 8 and 12 January at 1 hPa along with CTM CO sampled and gridded identically to the ISAMS data (see below). On 8 January the distorted vortex with extending “hook” near 90°E produced from the traveling anticyclone is evident in ISAMS (Fig. 3.9a) and CTM (Fig. 3.9b) CO. The model reveals a very distinct region of low CO near 220° apparently associated with a strong Aleutian high, while in ISAMS the Aleutian high appears to be stretched into a thin tongue of low CO. This discrepancy could be due to the fact that whereas CTM data are synoptic (at 00 UTC), the ISAMS data are taken over a period of 24 hours (00 to 24 UTC): as mentioned in section 2 no effort was made in the gridding of ISAMS data to correct for the asynoptic sampling.

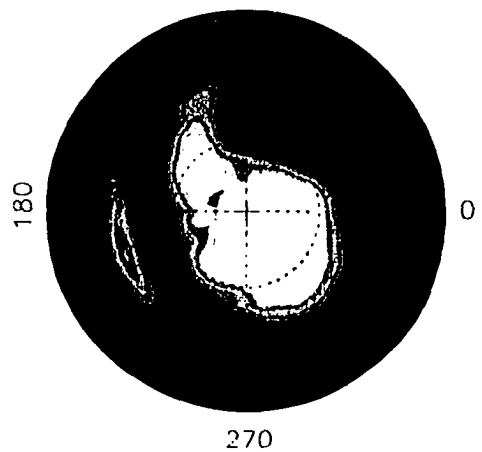
To analyze this more closely we “flew” *UARS* through the CTM by linearly interpolating the synoptic CTM data in space and time to the ISAMS level 2 grid and subsequently mapped the data with the identical procedure used with ISAMS CO (see section 2). The resulting map for 8 January (Fig. 3.9c) appears to show a slight improvement over the synoptic CTM map, especially in the orientation of the main vortex cell and shape of the decaying Aleutian high.

On 12 January, as the vortex becomes completely displaced off the pole, both ISAMS and CTM CO show good spatial agreement of all large-scale features. The comma shaped vortex structure is well defined while a region of high CO mixing ratio has been pulled from the vortex tail and has nearly reconnected with the main vortex. The model reveals interesting fine-scale structure that is not resolvable by ISAMS. The ISAMS-equivalent map of CTM CO for 12 January (Fig. 3.9f) also shows relatively good agreement with ISAMS CO (Fig. 3.9d), providing confidence that the distributions shown in observations and model are a realistic picture of the CO distribution in the upper stratosphere. We conclude that, in a qualitative sense, the horizontal ISAMS and CTM CO structures at 1.0 hPa are similar, even during this highly dynamic period. CO, as expected from photochemical arguments, is found to be a useful tracer of horizontal transport in the winter polar stratosphere.

Zonal mean plots of ISAMS and CTM CO from 10 to 0.1 hPa on 1 and 13 January 1992 are provided in Fig. 3.10 along with the ISAMS/CTM ratio. On 1 January both ISAMS and CTM

Figure 3.9 (a),(c) ISAMS CO for 8, 12 January 1992 at 1 hPa. (b),(d) CTM CO for 8, 12 January at 1 hPa. (e),(f) CTM CO gridded equivalently to the ISAMS data (see text) for 8,12 January at 1 hPa. Projections are Lambert equal area with latitude circles at 0°, 30°, and 60°N.

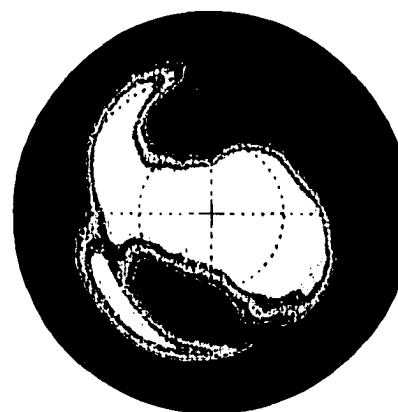
(a) ISAMS CO 8 Jan 92 1 hPa
90



(b) CTM CO 8 Jan 92 1 hPa



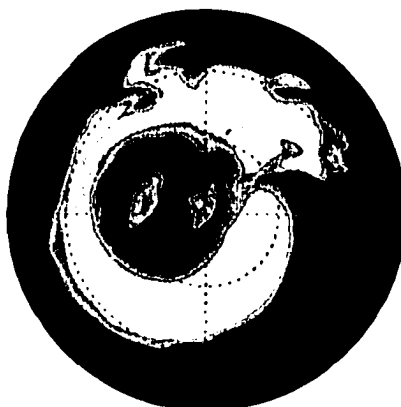
(c) L2 Equiv. CTM CO 8 Jan 92



(d) ISAMS CO 12 Jan 92 1 hPa



(e) CTM CO 12 Jan 92 1 hPa



(f) L2 Equiv. CTM CO 12 Jan 92

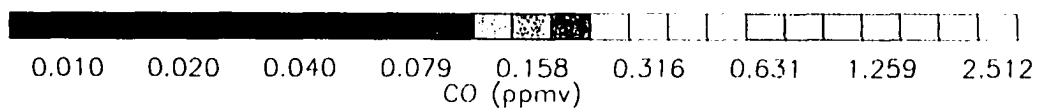
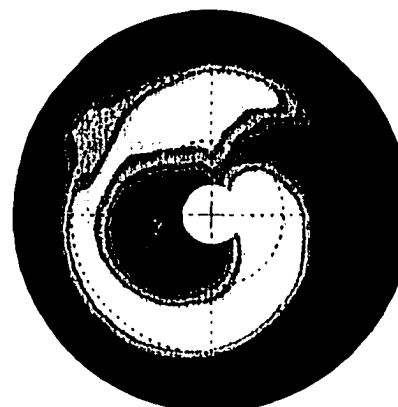
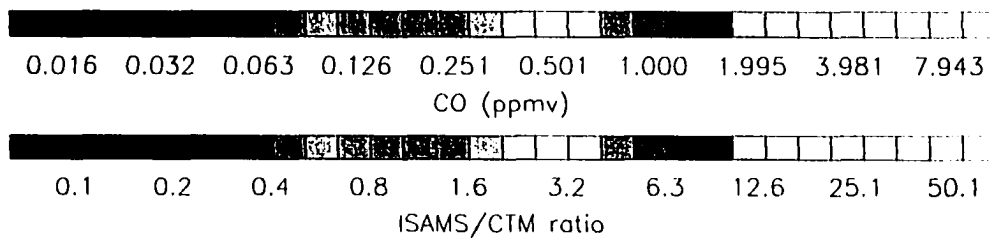
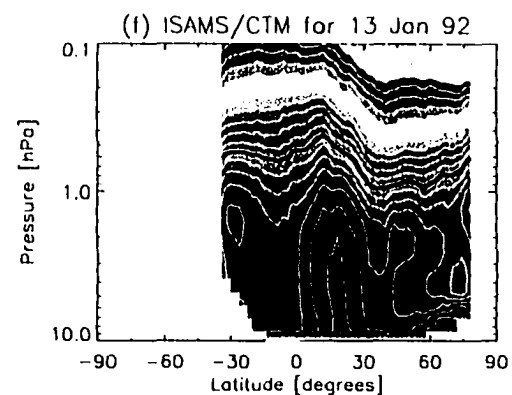
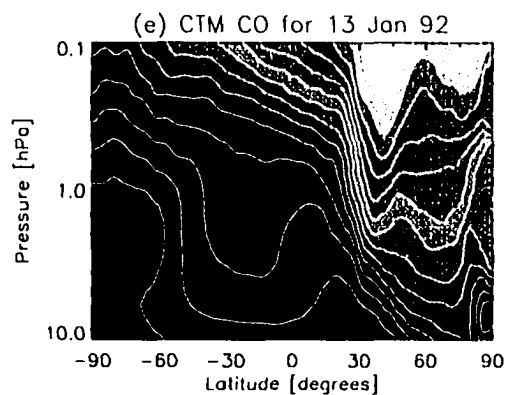
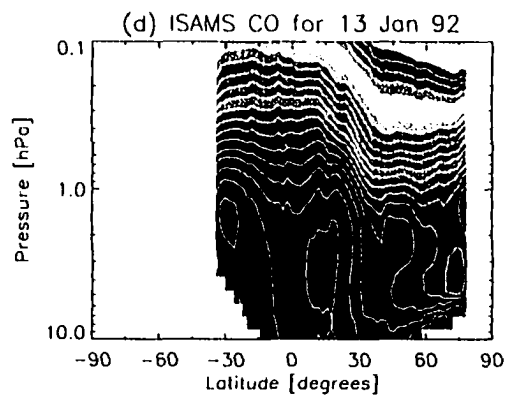
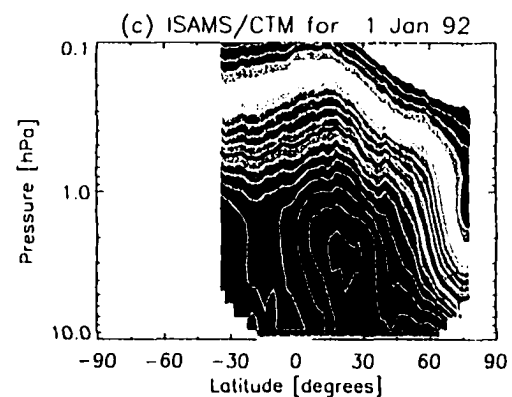
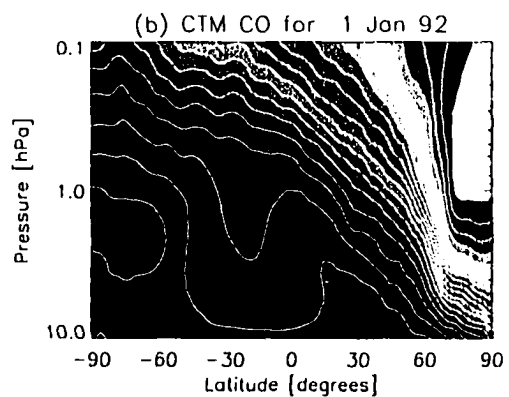
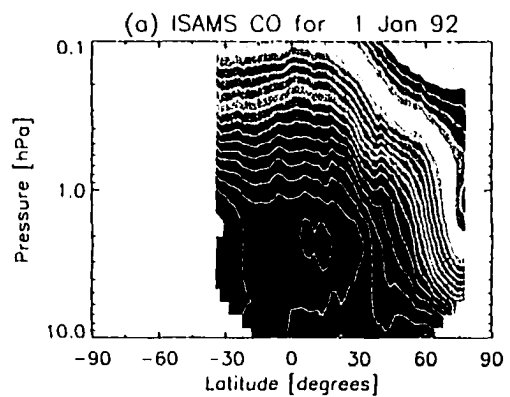


Figure 3.10 Zonal mean (a) ISAMS CO, (b) CTM CO, and (c) ISAMS/CTM ratio for 1 and January 1992. (d)–(f), Same as (a)–(c) but for 13 January 1992.



CO show strong meridional gradients near 60°N from 10 to 1.0 hPa, signifying the “edge” of the polar vortex. The low latitude maximum in the upper stratosphere, evident in ISAMS by the double-lobed minima near 30°S and 15°N, is present in the model, but not as distinct. By 13 January this feature becomes more obscured in the model, while ISAMS continues to display the robust double-lobed structure. Vertical gradients in ISAMS are larger than in the model from 1 to 0.1 hPa on both 1 and 13 January. The ISAMS/CTM ratios provided in Fig. 3.10 c,f show that ISAMS CO is larger than CTM CO in much of the lower mesosphere and in the stratospheric polar vortex and smaller throughout much of the upper stratosphere (the contour of ISAMS/CTM = 1 is highlighted in black). At the altitudes of interest, ISAMS CO have been shown to compare well (agreement to within the ISAMS standard deviation) with rocket data in May 1992 (Valverde et al. 1996), suggesting that the CTM may be largely underestimating the CO contribution from CO₂ photodissociation and downward transport from large source regions in the thermosphere. This not surprising due to the highly simplified chemistry used in this model run and lack of explicit vertical diffusion. These results suggest that ISAMS CO may be a useful quantity for testing and improving the vertical transport and CO photochemistry in more realistic CTM experiments.

Although further validation of ISAMS version 12 CO is necessary, comparison between ISAMS and CTM CO could provide useful validation of data quality as well as model constraints on the transport and chemistry in the upper stratosphere and lower mesosphere. The good agreement in horizontal structure lends confidence to the horizontal winds and transport scheme used by the CTM, while the discrepancy in vertical structure needs to be addressed by further analyses.

e. MLM diagnostics of vortex merger

The MLM diagnostics described in section 4 can be used to examine barrier evolution and mixing that accompany large stratospheric wave events. Local minima in equivalent length generally indicate barriers to horizontal mixing while maxima indicate regions of large mixing. Figure 3.11 provides synoptic maps of ISAMS CO at 1 hPa for 1 and 6 January 1992 along

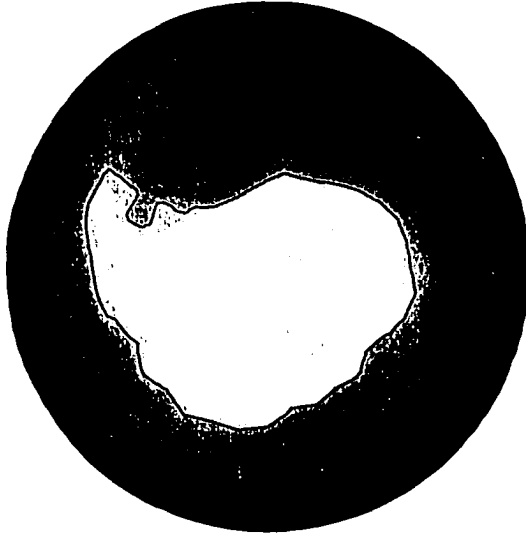
with normalized equivalent length, ξ (defined in section 4). On 1 January the circumpolar vortex is slightly elongated on the 30–210° axis with an emerging tail and intruding tongue of low latitude air, while ξ shows a minimum near 60° equivalent latitude, indicating a mixing barrier. The 60° equivalent latitude contour, identified in black on Fig. 3.11a, shows that the mixing barrier is near the vortex “edge”, identified here by the region of strong CO gradients. Five days later the vortex has been pushed off the pole and is deformed into a “comma” shape. ξ no longer shows a local minimum near 60° indicating that the distinct mixing barrier has disappeared. ξ gives effectively a measure of the perimeter length of a given contour: as evident from Fig. 3.11 the length of the 60° equivalent latitude contour has increased as a result of the altered vortex shape: the situation on 6 January more conducive to horizontal mixing processes.

In order to examine the meridional structure of mixing processes during January 1992, MLM diagnostics are applied to CTM output from 10 to 0.1 hPa. The MLM method assumes mixing ratios are generally monotonically increasing or decreasing with latitude in a hemisphere. Due to the tropical upper stratosphere maximum in CO, MLM cannot be reliably applied to CO in that region. However, if two tracers are in contour equilibrium (that is if their contours overlap, even if the gradients differ) one can prove mathematically (see Appendix at end of this chapter) that their equivalent lengths will be identical. A comparison of CTM CO (Fig. 3.12a–d) with CTM N₂O (Fig. 3.12e–h) for 1, 6, 11, and 16 January shows that CO and N₂O at 1 hPa have similar contour shapes (at least for the large-scale features). Since N₂O has monotonic gradients throughout the Northern Hemisphere stratosphere, we can apply MLM diagnostics to N₂O rather than CO to obtain a 2D picture of barrier evolution and horizontal mixing.

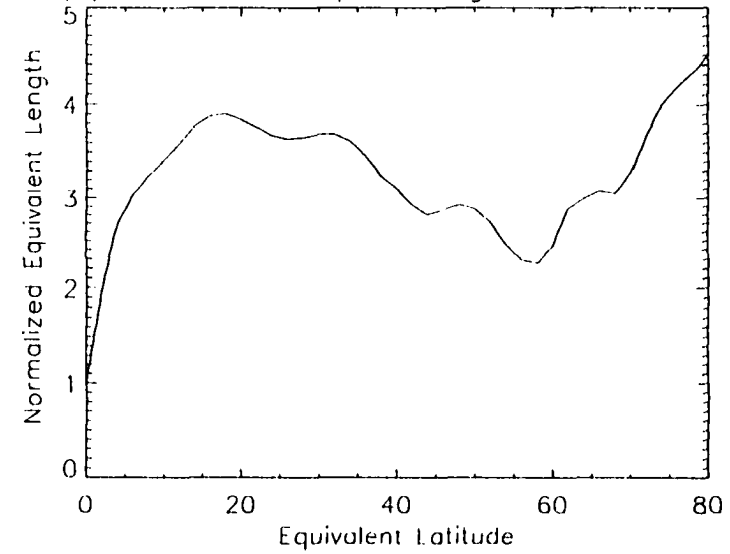
The normalized equivalent length ξ at 1.0 hPa on 1 January 1992 calculated from CTM N₂O is provided in Fig. 3.12i. This shows similar structure to ξ calculated from ISAMS CO (Fig. 3.11b), although the mixing barrier appears stronger and is centered near 70° rather than 60° equivalent latitude. The difference in magnitude of ξ between the ISAMS and CTM analyses is due partly to the different horizontal resolution of the two data sets (Nakamura

Figure 3.11 (a) ISAMS CO and (b) normalized equivalent length (from the MLM formulation, see text) at 1.01 hPa for 1 January 1992. (c), (d) Same as (a), (b), but for 6 January 1992.

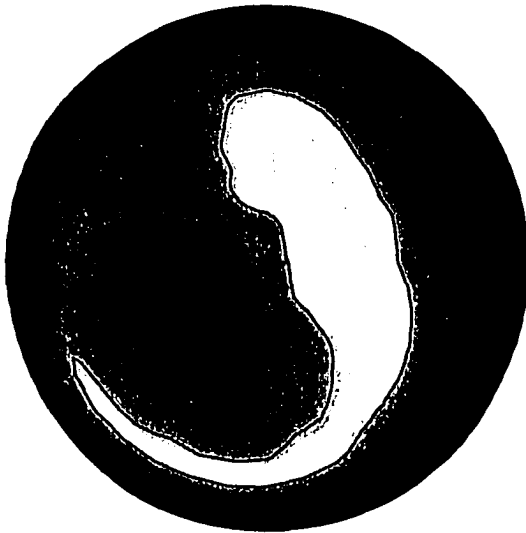
(a) ISAMS CO at 1.01 hPa for 1 Jan 92



(b) Normalized Equiv. Length for 1 Jan 92



(c) ISAMS CO at 1.01 hPa for 6 Jan 92



(c) Normalized Equiv. Length for 6 Jan 92

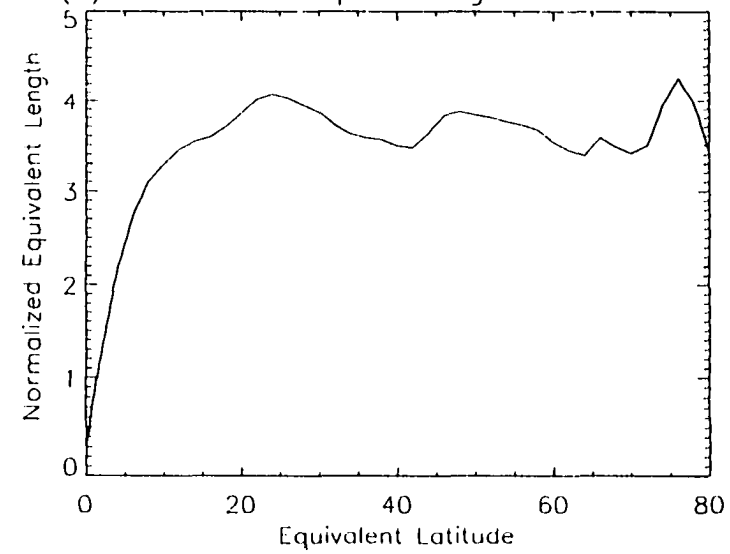
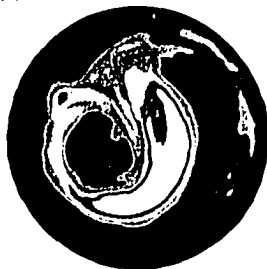


Figure 3.12 (a)–(d) CTM CO at 1 hPa for 1, 6, 11, and 16 January 1992. (e)–(h) CTM N₂O at 1 hPa. (i)–(l) Equivalent length calculated from CTM N₂O at 1 hPa. (m)–(p) Two-dimensional cross-section of normalized equivalent length (filled contours) calculated from CTM N₂O overlaid by contours of the N₂O value corresponding to each pressure and equivalent latitude (white contours).

(a) CTM CO at 1 hPa for 1 Jan 92



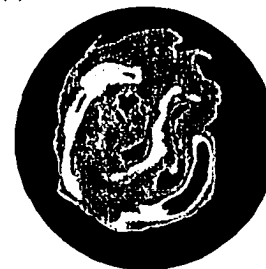
(b) CTM CO at 1 hPa for 6 Jan 92



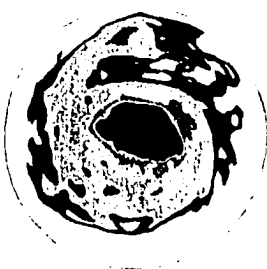
(c) CTM CO at 1 hPa for 11 Jan 92



(d) CTM CO at 1 hPa for 16 Jan 92



(e) CTM N2O at 1 hPa for 1 Jan 92



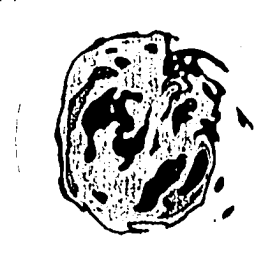
(f) CTM N2O at 1 hPa for 6 Jan 92



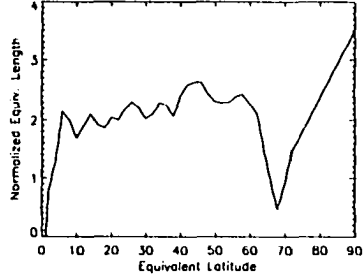
(g) CTM N2O at 1 hPa for 11 Jan 92



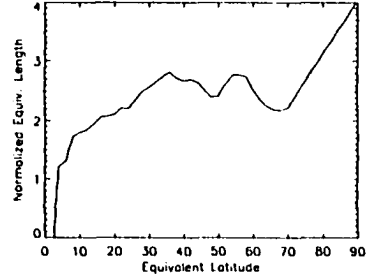
(h) CTM N2O at 1 hPa for 16 Jan 92



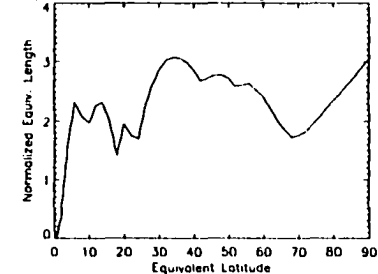
(i) Normalized Equivalent Length for 1 Jan 92



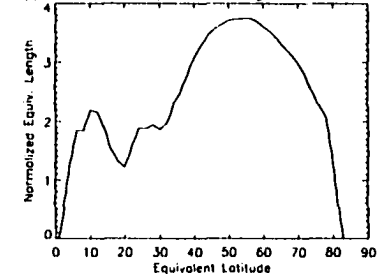
(j) Normalized Equivalent Length for 6 Jan 92



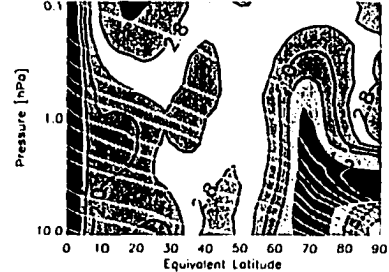
(k) Normalized Equivalent Length for 11 Jan 92



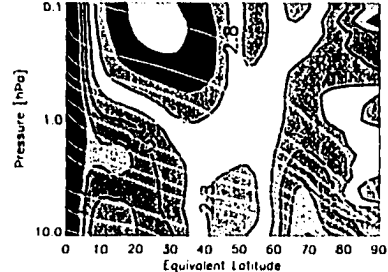
(l) Normalized Equivalent Length for 16 Jan 92



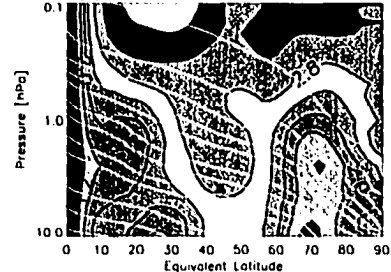
(m) MLM for CTM N2O on 1 Jan 92



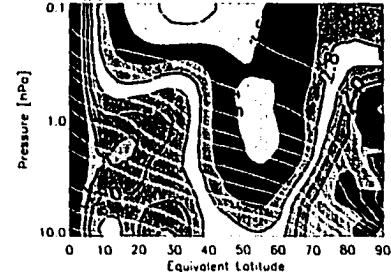
(n) MLM for CTM N2O on 6 Jan 92



(o) MLM for CTM N2O on 11 Jan 92



(p) MLM for CTM N2O on 16 Jan 92



1996). The mixing barrier appears to weaken by 6 January (similar to Fig. 3.11d), attempts a slight comeback by 11 January and is completely eliminated by 16 January, when a broad region of large mixing encompasses 40° to 80° equivalent latitude. The rapid mixing occurring during this period is evident in the synoptic plots of CTM CO (Fig. 3.12a–d) and CTM N_2O (Fig. 3.12e–h). The main vortex cell, highlighted by bright regions in CO and dark regions in N_2O , which covers a large area on 1 January, has nearly disappeared by 16 January, leaving a broad well-mixed region in the upper stratosphere.

Two-dimensional maps of ξ are plotted in Fig. 3.12m–p as a function of pressure and equivalent latitude. On 1 January a strong barrier is evident at 70° from 10 to 1 hPa with minimal regions of large mixing (here defined arbitrarily by $\xi \geq 2.8$). Five days later the barrier has weakened significantly while a region of large ξ develops roughly from 10° to 50° equivalent latitude and from 1 to 0.1 hPa. The polar upper stratospheric barrier strengthens slightly by 11 January as the entire lower mesosphere is saturated by large mixing. By 16 January the lower mesosphere is thoroughly mixed as values of ξ greater than 2.8 extend from 10° to 90° equivalent latitude. The upper stratosphere shows a well defined mixed region from 40° to 60° at 10 hPa, widening to 40° to 80° at 1 hPa.

These analyses of CTM N_2O appear to indicate that the large mixing associated with planetary wave activity from 1–16 January first appears in the mesosphere and subsequently descends into the upper stratosphere. This is possibly related to differences with altitude in the meridional PV gradient, which provides the restoring mechanism for propagating planetary waves. In the upper stratosphere, strong PV gradients are associated with the polar vortex (the northern stratospheric vortex in early January 1992 maximizes near 2–4 hPa and 60° – 70° N), while weaker gradients occur in the mesosphere. This means that the mesosphere is less capable of supporting planetary-wave propagation, so irreversible mixing by the breaking of vertically-propagating planetary-waves will occur more rapidly in the mesosphere than in the stratosphere. The breakdown of the polar upper stratospheric barrier described by MLM diagnostics is shown here to be a complex process, involving episodes of growth and decay. The equivalent length provides a useful diagnostic of the short term changes involved in winter

vortex evolution.

6. Conclusions

Observations of ISAMS CO from 10 to 0.1 hPa are presented during the dynamically active early northern winter 1991/1992. High CO mixing ratios saturate the polar vortex, as seen by comparing CO with derived Ertel potential vorticity. 2D analyses in the meridional plane show a CO maximum near the Arctic winter pole due to diabatic sinking, decreasing mixing ratio with decreasing latitude in the mesosphere, and an upper stratospheric low latitude maximum, likely due to methane oxidation. The evolution of ISAMS CO is compared with output from a six-week run (initialized on 8 December 1991) of the GSFC 3D chemistry and transport model. The horizontal distributions compare well, even during the highly dynamic period from 1–16 January 1992, while significant differences are evident in the zonal mean meridional structure from 10 to 0.1 hPa, including stronger vertical gradients of ISAMS CO and better capture by ISAMS of the persistent tropical upper stratospheric maximum. Transport barriers and regions of significant mixing are identified by minima and maxima in the constituent “equivalent length,” a modified Lagrangian mean diagnostic. On 1 January 1992 a mixing barrier is identified near the vortex edge in both ISAMS CO and CTM N₂O. This barrier weakens over the next two weeks as planetary wave activity erodes the polar vortex, leaving a well-mixed lower mesosphere and broad surf zone in the upper stratosphere.

Although the ISAMS CO data do contain significant noise due to unavoidable difficulties in the retrieval, with care the data can be used to enhance significantly our knowledge of the chemistry and transport of the upper stratosphere and lower mesosphere. ISAMS CO has been particularly useful for examining advective and diffusive tracer transport, CH₄ oxidation in the upper stratosphere, vortex evolution and breakup, location and evolution of horizontal mixing barriers, and 3D chemistry and transport model validation.

Acknowledgements

We want to thank R. J. Wells for helpful comments on the manuscript and invaluable assistance with the ISAMS data. Drs. R. Swinbank and A. O'Neill developed the UKMO data (used in the PV-mapping) from which PV was calculated using code from Dr. M. Chipperfield. NCEP-derived PV data were provided by Dr. G. Manney. Many of the IDL and FORTRAN programs used for this study were modified from programs written by Dr. H. Pumphrey. *UARS* level 3AT data were obtained from the EOS Distributed Active Archive Center (DAAC, code 902.2) at the Goddard Space Flight Center, Greenbelt, MD. The activities of the EOS DAAC and the *Upper Atmosphere Research Satellite (UARS)* Project (code 916) are sponsored by NASA's Mission to Planet Earth Program. ISU coauthors are sponsored in part by National Aeronautics and Space Administration Grant NAG 5-2787. This work was done while D. Allen was a Guest Graduate Student at Argonne National Laboratory, Argonne, IL.

Appendix: Proof that equivalent length is the same for all species in contour equilibrium

By definition any two tracers in contour equilibrium hold a compact relationship. That is, the mixing ratio of one is specified by that of another:

$$\chi_1(x, y, \theta, t) = \chi_1(\chi_2(x, y, \theta, t)). \quad (3.11)$$

where χ_1 and χ_2 are the mixing ratios of the two species. The above relationship does not necessarily have to be monotonic (one-to-one). Equivalent length defined through χ_1 is

$$L_\epsilon^2 = (\partial\chi_1/\partial A)^{-2} \langle |\nabla\chi_1|^2 \rangle. \quad (3.12)$$

where the angle brackets denote the contour average. However, since

$$\frac{\partial\chi_1}{\partial A} = \frac{d\chi_1}{d\chi_2} \frac{\partial\chi_2}{\partial A}; \quad \nabla\chi_1 = \frac{d\chi_1}{d\chi_2} \nabla\chi_2. \quad (3.13)$$

Eq.(3.12) can be rewritten as

$$L_\epsilon^2 = (\partial\chi_1/\partial A)^{-2} \langle |\nabla\chi_1|^2 \rangle = (\partial\chi_2/\partial A)^{-2} (d\chi_1/d\chi_2)^{-2} \langle (d\chi_1/d\chi_2)^2 |\nabla\chi_2|^2 \rangle \quad (3.14)$$

$$= (\partial\chi_2/\partial A)^{-2} \langle |\nabla\chi_2|^2 \rangle \quad (3.15)$$

The last identity uses the fact that $d\lambda_1/d\lambda_2$ is a constant on the tracer contour. Hence equivalent length is identical whether λ_1 or λ_2 is used. Notice, however, that the gradients of the two tracers are not necessarily the same since in general $d\lambda_1/d\lambda_2 \neq 1$ in Eq.(3.13).

CHAPTER 4 GENERAL CONCLUSIONS

The 4-day wave

This dissertation involves two topics in middle atmosphere dynamics: the 4-day wave and observations of middle atmosphere CO. The method of study involves analyses of atmospheric data from two limb-sounding instruments on board the Upper Atmosphere Research Satellite using various diagnostic techniques and comparison with model results. Chapter 2 takes advantage of the vertical coverage and resolution of the Microwave Limb Sounder (MLS) instrument to analyze the 4-day wave during August–September 1992 and 1993. Strong 4-day wave events are evident for both years in MLS temperature, geopotential height, and quasigeostrophic potential vorticity derived from MLS geopotential heights. A double-peaked temperature structure is found with maxima in the upper stratosphere and lower mesosphere and strong vertical phase variation in between, as predicted by 3D modeling results. Four-day eastward period signals are also evident in MLS ozone. The amplitude and phase of these signals compare well with results from a linear advective–photochemical model of the ozone response to wind and temperature perturbations associated with the 4-day wave. A region of negative quasigeostrophic potential vorticity gradient is shown to overlap positive EP flux divergence, in agreement with previous studies, suggesting that instability dynamics is involved in the wave forcing.

The observed three-dimensional wave structure is shown to resemble the potential vorticity charge concept, wherein a PV anomaly in the atmosphere induces a vertical temperature dipole, circulation about the vertical axis, and a geopotential anomaly. This analogy suggests that the 4-day wave may be more fundamentally viewed as a PV anomaly than a temperature anomaly. The wave life cycle begins with an unstable atmosphere that allows growth in PV

anomaly amplitude, which induces anomalies in temperature, geopotential, and wind. The PV charge paradigm, coupled with its generation by instability mechanisms, offers an elegant and conceptually satisfying explanation of the physics of the 4-day wave.

In the broad picture of middle atmosphere dynamics, the 4-day wave (a type of vortex) provides an interesting example of what could be called a “vortex within a vortex.” Since the feature occurs near the polar vortex region, the circulation accompanying the wave may stir air across the vortex edge as the wave rotates around the pole. Analyses of the 4-day wave in 3D models would be useful for assessing the mixing processes accompanying the feature. Since the publication of this work, we have learned of possible evidence of the 4-day wave in a general circulation model developed in the United Kingdom (Dr. Warwick Norton, personal communication). By carefully examining constituent transport in the model, it may be possible to quantify the magnitude of mixing across the vortex edge due to the 4-day wave.

From a more fundamental viewpoint, the 4-day wave may be the best known example of a solitary wave (or soliton) in the middle atmosphere. One can show (Dodd et al. 1982) that the equation of potential vorticity conservation under quasigeostrophic, adiabatic, frictionless conditions actually reduces to the Korteweg-deVries (KdV) equation when the trial solution is expanded in terms of stretched coordinates which focus on long-wavelength solutions. The nonlinear KdV equation has the well known analytic soliton solution in which the wave propagates indefinitely without change of shape or speed. In the geophysical case, the nonlinear term (which represents advective steepening of the wave shape) exactly balances the dispersive term (which causes broadening of the wave). More work is needed to elucidate the relationship between the observed 4-day wave and the solitary Rossby wave solution, with fruitful results expected.

Observations of middle atmosphere CO

Chapter 3 involves the analyses of carbon monoxide in the middle atmosphere as observed from the Improved Stratospheric and Mesospheric Sounder (ISAMS). To date these are the best available data on the global distribution and seasonal evolution of CO in the upper stratosphere

and lower mesosphere. This study shows high CO mixing ratios in the polar vortex, generally increasing mixing ratio with height from 10 to 0.1 hPa, decreasing mixing ratio with decreasing latitude in the mesosphere, and an upper stratospheric tropical maximum, which is shown to be likely due to methane oxidation. The evolution of ISAMS CO was compared with output from the GSFC 3D CTM, initialized with the ISAMS CO distribution. The horizontal evolutions compared well, even during the highly dynamic period in early January 1992, while significant differences were seen in the zonal mean meridional structure, with CTM mixing ratios biased high in the upper stratosphere outside the polar vortex and low in the stratospheric vortex and lower mesosphere. Novel modified Lagrangian mean techniques were used to identify mixing barriers and well-mixed regions during the vortex merger from 1-16 January 1992. A barrier identified in the upper stratosphere on 1 January was shown to weaken over the next two weeks as planetary wave activity eroded the polar vortex. A region of large mixing developed in the mesosphere and subsequently descended into the upper stratosphere; the apparent downward propagation of the mixing region may be due to differences in the potential vorticity gradient with height, since weaker mesospheric PV gradient are less able to support Rossby wave propagation than the stronger upper stratosphere gradients.

ISAMS CO data provide an excellent source for studying the dynamics and carbon chemistry of the upper stratosphere and lower mesosphere. Since the mixing ratio increases with altitude, CO data are available well into the mesosphere, while the signals from long-lived tracers with tropospheric sources and stratospheric sinks such as N_2O or CH_4 are generally too small for reliable measurement. CO is found to be a particularly good tracer of the polar vortex evolution and may also be useful for examining the meridional diabatic circulation and vertical diffusion. Finally, ISAMS CO have proven useful for validation of a 3D CTM. It is evident from the comparisons here that, although the horizontal transport in the GSFC CTM looks reliable, unrealistic vertical transport causes large differences with observations. This may be due to deficiencies in the model and/or the vertical assimilation winds that drive the model.

It was my hope in this study to show that, although the ISAMS CO data contain sig-

nificant noise due to unavoidable difficulties in the retrieval, with care the data can be used to significantly enhance our knowledge of the chemistry and transport of the middle atmosphere. Additional research will focus on the structure and dynamical evolution of the upper stratosphere and lower mesosphere during the Southern Hemisphere early winter. Comparison will be made with the GSFC CTM as well as application of modified Lagrangian mean and trajectory analyses to elucidate tracer transport in the southern polar vortex region.

APPENDIX: GLOSSARY

Note: These definitions are applied to the earth's atmosphere only; words such as "diffusion" will have different meanings in other contexts.

Adiabatic process: A change of state of a system in which there is no transfer of heat or mass across the boundaries of the system. Adiabatic compression (expansion) results in warming (cooling) of the system.

Advection: The transport of air parcels (or mass) by the atmospheric velocity field (wind).

Aleutian high: An anticyclone centered in longitude and latitude near the Aleutian islands, off the south-west coast of Alaska.

Anomaly: The departure of a quantity from its time mean or spatial mean value. Used synonymously in this study with perturbation.

Anticyclone: A closed circulation that has a rotation around the local vertical axis opposite to that of the earth's rotation—clockwise (counter-clockwise) in the Northern (Southern) Hemisphere.

Assimilation: Data assimilation involves gathering data that are scattered in space and time and integrating that data into a sequence of globally-coherent 3D pictures of chemical and meteorological quantities that constitute the earth's atmosphere.

Asynoptic: A view of the atmosphere in which data are taken over a specified region at different times.

Austral: Referring to the Southern Hemisphere

Baroclinic: Atmospheric state where the density depends on pressure and temperature. Under the geostrophic and hydrostatic approximations for an ideal gas the baroclinic state exhibits vertical shear of horizontal wind proportional to the meridional temperature gradient.

Barotropic: Atmospheric state where the density depends only on the pressure. Under the geostrophic and hydrostatic approximations for an ideal gas the barotropic state exhibits horizontal wind with direction and magnitude that are independent of altitude.

Brunt-Väisälä parameter: The frequency of oscillation (N) of vertically displaced parcels in an atmosphere in hydrostatic equilibrium. Mathematically,

$$N^2 = \left(\frac{g}{\theta} \frac{\partial \theta}{\partial z} \right). \quad (\text{A.1})$$

where θ is potential temperature, g is the earth's gravitational acceleration, and z is height.

Circulation: The flow of air through a given area or volume.

Circumpolar: That which surrounds one of the earth's poles.

Climatology: Used here as a long-term average of a given quantity.

Conserved quantity: A quantity identifiable in an air parcel that maintains a constant value following the motion of the parcel (also see potential vorticity derivation).

Constituent: One component of a multi-component system; e.g., ozone is an atmospheric constituent.

Coriolis Parameter: $f = 2 \Omega \sin \phi$, where ϕ is latitude and Ω is the earth's angular velocity.

Cyclone: A closed circulation that has a rotation around the local vertical axis in the same manner as that of the earth's rotation—clockwise (counter-clockwise) in the Southern (Northern) Hemisphere.

Cyclonic scale: Generally associated with migratory pressure systems in the lower troposphere of size 1000 to 2500 km. Also called synoptic scale.

Diabatic: A change of state of a system in which there is transfer of heat or mass across the boundaries of the system.

Diffusion: The exchange of air parcels in space due to random molecular motions, in contrast to advection. Atmospheric modelers may define diffusion more broadly as constituent transport on scales smaller than the grid-scale of the model.

Dynamics: The study of the fluid motions of the atmosphere on scales large enough so that the discrete molecular composition of the atmosphere can be ignored.

Easterly: From east to west.

Eastward: From west to east.

Eulerian mean: An average taken in a frame of reference with fixed points in space (relative to the earth).

Geopotential: Potential energy of a unit mass relative to sea level. Also equal to the work done raising a unit mass from sea level to a given height z .

$$\Phi = \int_0^z g \, dz \quad (\text{A.2})$$

where Φ is geopotential and $g(z)$ is the earth's gravitational acceleration.

Geopotential height: The geopotential divided by $g_0 = 9.80665 \, \text{ms}^{-2}$, the average gravitational acceleration at sea level.

Geostrophic: An atmospheric state where an exact balance occurs between the Coriolis force and the horizontal pressure gradient force, resulting in the geostrophic approximation to the horizontal wind:

$$u = -\frac{1}{f} \frac{\partial \Phi}{\partial y} \quad v = \frac{1}{f} \frac{\partial \Phi}{\partial x}, \quad (\text{A.3})$$

where u (v) is the zonal (meridional) geostrophic velocity, Φ is geopotential, f is the Coriolis parameter, and x (y) correspond to the zonal (meridional) coordinate.

Hydrostatic: An atmospheric state where an exact balance occurs between the gravitational force and the vertical pressure gradient force. Under hydrostatic equilibrium the surfaces of constant pressure and density are horizontal and directly coincide. This results in the hydrostatic equation:

$$\frac{\partial p}{\partial z} = -\rho g \quad (\text{A.4})$$

where p is pressure, z is height, ρ is density, and g is the earth's gravitational acceleration.

Instability: In the atmosphere, a flow field is said to be unstable if a small perturbation introduced into the flow grows with time, drawing energy from the mean flow. Mathematically, a condition where the solution of a partial differential equation has an amplitude that increases exponentially with time.

Isentropic surface: An atmospheric layer with constant potential temperature (or entropy).

Jacobian: For the horizontal coordinates x and y the Jacobian of the quantities u and v is:

$$J(u, v) = \frac{\partial u}{\partial x} \frac{\partial v}{\partial y} - \frac{\partial u}{\partial y} \frac{\partial v}{\partial x}. \quad (\text{A.5})$$

Jet: Strong horizontal winds located in a relatively narrow stream in the atmosphere. The polar stratospheric vortex is often referred to as the stratospheric jet.

Lagrangian mean: An average taken in a frame of reference which follows the motion of an air parcel.

Mean meridional circulation: A general term for the observed zonally averaged meridional and vertical wind. At solstice in the stratosphere and mesosphere this involves rising (sinking) near the summer (winter) pole, cross-equatorial transport from summer to winter hemisphere, and rising motion in the tropical lower stratosphere. Often referred to as the diabatic circulation.

Meridional: Pertaining to the north-south direction, i.e. along a line of constant longitude.

Middle atmosphere: The atmospheric layer roughly from 10 to 100 km, containing the stratosphere, mesosphere, and lower thermosphere.

Midlatitude: Referring generally to the region between the tropics and the polar region, 30° to 60° in either hemisphere.

Mixing ratio: The fraction of the volume (or mass) of a constituent contained in a unit volume (or mass) of air. Expressed in this study as parts per million volume (ppmv).

Nondispersive wave: A wave feature in which the phase speed is independent of wavenumber, so that the shape of the feature does not change with time.

Nyquist frequency: The limiting frequency of a Fourier analysis of discretely sampled data. For sampling interval Δt , the Nyquist frequency is $1/(2\Delta t)$.

Parcel: A "point" in the atmospheric continuum consisting of a large number of molecules, but small with respect to the volume under consideration, which has unique values for each physical quantity that characterizes the atmospheric state.

Perturbation: See Anomaly.

Phase speed: In an oscillating disturbance, the propagation speed of a point of constant phase. For motion of form $e^{i(kx-\omega t)}$ the phase speed is found to be ω/k .

Photochemical lifetime: The time required for the concentration of a given constituent to decrease to $1/e$ of its initial value.

Planetary wave: See Rossby wave.

Polar region: Generally the region from 60° to the pole in either hemisphere.

Polar night: Latitudes at which the sun never crosses the earth's horizon during a 24-hour period. This region extends from the North Pole to the Arctic circle ($66^\circ 32' \text{ N}$) on the winter solstice (about 22 December) and from the South Pole to the Antarctic circle ($66^\circ 32' \text{ S}$) on the summer solstice (about 21 June).

Polar night vortex: A high latitude westerly jet that occurs in the winter stratosphere, also referred to as the polar night jet. Polar vortex can also refer to the large-scale tropospheric polar jet, however, in this study we deal exclusively with the stratospheric vortex.

Potential temperature: The temperature a parcel of dry air (with pressure p and temperature T) would have if brought adiabatically to standard pressure (1000 hPa). Mathematically it is defined by

$$\theta = T \left(\frac{1000}{p} \right)^{\frac{R}{c_p}} \quad (\text{A.6})$$

where R is the dry air gas constant and c_p is the specific heat of dry air at constant pressure.

Potential vorticity (Q): The scalar product of the absolute vorticity and the potential temperature gradient. $Q = \rho^{-1} \zeta_a \cdot \nabla \theta$. (derivation follows).

We start with Newton's second law applied to the atmosphere in a reference frame that rotates with the earth.

$$\frac{D\mathbf{V}}{Dt} = -2\boldsymbol{\Omega} \times \mathbf{V} - \frac{1}{\rho} \nabla p + \mathbf{g} + \mathbf{F}. \quad (\text{A.7})$$

where each term on the right hand side represents a force per unit mass acting on an air parcel. These include the Coriolis ($-2\boldsymbol{\Omega} \times \mathbf{V}$), pressure gradient ($-\rho^{-1} \nabla p$), gravitational (\mathbf{g}), and frictional (\mathbf{F}) forces. $D(\)/Dt = \partial(\)/\partial t + \mathbf{V} \cdot \nabla(\)$ is the total derivative.

By taking the curl of Eq.(A.7) we obtain an equation for the absolute vorticity $\zeta_a = 2\boldsymbol{\Omega} + \nabla \times \mathbf{V}$:

$$\frac{\partial \zeta_a}{\partial t} + \nabla \times (\zeta_a \times \mathbf{V}) = \frac{1}{\rho^2} \nabla \rho \times \nabla p + \nabla \times \mathbf{F} \quad (\text{A.8})$$

By taking the scalar product of Eq.(A.8) with $\nabla \theta$, the gradient of potential temperature, we obtain the flux form of the potential vorticity equation:

$$\frac{\partial(\rho Q)}{\partial t} + \nabla \cdot (\rho Q \mathbf{V} - \dot{\theta} \zeta_a - \mathbf{F} \times \nabla \theta) = 0. \quad (\text{A.9})$$

$Q = \rho^{-1} \zeta_a \cdot \nabla \theta$ is the potential vorticity and $\dot{\theta}$ refers to the total time derivative of potential temperature ($\dot{\theta} = D\theta/Dt = \partial\theta/\partial t + \mathbf{V} \cdot \nabla \theta$). This shows the remarkable fact that Q has no source term, and therefore it cannot be created nor destroyed in the flow, away from boundaries, even in the presence of diabatic and frictional effects (Haynes and McIntyre 1987). By combining Eq.(A.9) with the mass continuity equation, using θ as

the vertical coordinate, and assuming that frictional and diabatic terms can be neglected (i.e., $\dot{\theta} = 0$ and $\mathbf{F} = 0$), we find:

$$\frac{D_{\theta}Q}{Dt} = 0. \quad (\text{A.10})$$

where the total derivative follows the parcel motion on isentropic surfaces. So under adiabatic, frictionless conditions, the potential vorticity of a given air parcel will remain constant, thus Q can be used as a tracer of the atmospheric motion.

Quasigeostrophic approximation: Approximation to the equations of motion that assumes geostrophic equilibrium in certain contexts, but not in others. This allows the filtering of higher frequency atmospheric oscillations (e.g., sound and gravity waves), but retains cyclonic-scale motions.

Rossby wave: A potential vorticity-conserving oscillating motion in the atmosphere for which the restoring mechanism is due to the isentropic gradient of potential vorticity. Rossby waves propagate westward with respect to the zonal flow with periods of several days, vertical wavelengths of order 10 km, and horizontal wavelengths from hundreds of km up to zonal wavenumber 1 [zonal wavenumber: see wavenumber]. Synonymous with planetary wave.

Solstice: The two times of the year when the sun's path extends farthest from the equator. In the Northern Hemisphere, summer (winter) solstice occurs near 21 June (22 December). Dates are reversed for the Southern Hemisphere.

Spectral analyses: Analysis technique that separates discrete data in time and/or space into frequency and/or wavenumber components using discrete Fourier decomposition.

Synoptic: A view of the atmosphere in which data are taken simultaneously over a large region to obtain a "snapshot" at a given moment in time.

Tracer: A quantity used to analyze the motion of air parcels. Conserved tracers will maintain a constant value following the parcel trajectory, and therefore information about air motions can be obtained by observing the time evolution of such a tracer.

Trajectory: A curve connecting the points in space through which an advected parcel passes in a given time.

Transport: Process by which a quantity is carried past a fixed point in space.

Tropics: Technically, tropics refers to latitudes between the Tropic of Cancer ($23^{\circ}27' \text{ N}$) and the Tropic of Capricorn ($23^{\circ}27' \text{ S}$). In practice, many atmospheric scientists use the less rigid definition of 30°N to 30°S .

Vortex: Usually refers to a flow with closed streamlines and termed cyclonic or anticyclonic depending on the direction of the circulation.

Wave: Generally, a pattern in a given geophysical quantity that has an identifiable periodicity in time and/or space.

Wavenumber: Usually referring to the zonal direction—zonal wavenumber. It is the integer number of complete wavelengths that fit around a latitude circle.

Westerly: From west to east.

Westward: From east to west.

Zonal: Pertaining to the east–west direction, i.e., along a line of constant latitude.

Zonal mean: The average of a quantity around a latitude circle.

REFERENCES

- Aellig, C. P., N. Kämpfer, and A. Hauchecorne, 1995: Variability of mesospheric CO in the fall and winter as observed with ground-based microwave radiometry at 115 GHz. *J. Geophys. Res.*, **100**, 14 125–14 130.
- Allen, D. R., J. L. Stanford, L. S. Elson, E. F. Fishbein, L. Froidevaux, and J. W. Waters, 1997: The 4-day wave as observed from the Upper Atmosphere Research Satellite microwave limb sounder. *J. Atmos. Sci.*, **54**, 420–434.
- Allen, M., Y. Yung, and J. W. Waters, 1981: Vertical transport and photochemistry in the terrestrial mesosphere and lower thermosphere (50–120 km). *J. Geophys. Res.*, **86**, 3617–3627.
- Andrews, D. G., J. R. Holton, and C. B. Leovy, 1987: *Middle Atmosphere Dynamics*. Academic Press, 489 pp.
- , D. G., and M. E. McIntyre, 1976: Planetary waves in horizontal and vertical shear: The generalized Eliassen–Palm relation and the mean zonal acceleration. *J. Atmos. Sci.*, **33**, 2031–2048.
- , and ———, 1978: Generalized Eliassen–Palm and Charney–Drazin theorems for waves on axisymmetric mean flows in compressible atmospheres. *J. Atmos. Sci.*, **35**, 175–185.
- Barath, F. T., and Coauthors, 1993: The Upper Atmosphere Research Satellite microwave limb sounder instrument. *J. Geophys. Res.*, **98**, 10 751–10 762.
- Bevilacqua, R. M., A. A. Stark, and P. R. Schwartz, 1985: The variability of carbon monoxide in the terrestrial mesosphere as determined from ground-based observations of the $J = 1 \rightarrow 0$ emission line. *J. Geophys. Res.*, **90**, 5777–5782.
- Bishop, C. H., and A. J. Thorpe, 1994: Potential vorticity and the electrostatics analogy: Quasi-geostrophic theory. *Quart. J. Roy. Meteor. Soc.*, **120**, 713–731.
- Bowman, K. P., and P. Chen, 1994: Mixing by barotropic instability in a nonlinear model. *J. Atmos. Sci.*, **51**, 3692–3705.

- Brasseur, G., and S. Solomon, 1986: *Aeronomy of the Middle Atmosphere*, 2d ed., D. Reidel, 452 pp.
- Chang, A. Y., and Coauthors, 1996: A comparison of measurements from ATMOS and instruments aboard the ER-2 aircraft: Tracers of atmospheric transport, *Geophys. Res. Lett.*, **23**, 2389-2392.
- Clancy, R. T., D. O. Muhleman, and G. L. Berge, 1982: Microwave spectra of terrestrial mesospheric CO, *J. Geophys. Res.*, **87**, 5009-5014.
- , D. O. Muhleman, and M. Allen, 1984: Seasonal variability of CO in the terrestrial mesosphere, *J. Geophys. Res.*, **89**, 9673-9676.
- DeMore, W. B., and Coauthors, 1992: *Chemical kinetics and photochemical data for use in stratospheric modeling*, JPL Pub. 92-20.
- Dodd, R. K., J. C. Eilbeck, J. D. Gibbon, and H. C. Morris, 1982: *Solitons and Nonlinear Wave Equations*, Academic Press, pp. 249-256.
- Douglass, A. R., C. J. Weaver, R. B. Rood, and L. Coy, 1996: A three-dimensional simulation of the ozone annual cycle using winds from a data assimilation system, *J. Geophys. Res.*, **101**, 1463-1474.
- Edmon, H. J., Jr., B. J. Hoskins, and M. E. McIntyre, 1980: Eliassen-Palm cross sections for the troposphere, *J. Atmos. Sci.*, **37**, 2600-2616; Corrigendum, **38**, 1115.
- Elson, L. S., and L. Froidevaux, 1993: The use of Fourier transforms for asymptotic mapping: Applications to the Upper Atmosphere Research Satellite microwave limb sounder, *J. Geophys. Res.*, **98**, 23 039-23 049.
- Fishbein, E. F., and Coauthors, 1996: Validation of UARS MLS temperature and pressure measurements, *J. Geophys. Res.*, **101**, 9983-10 016.
- Fraser, G. J., G. Hernandez, and R. W. Smith, 1993: Eastward-moving 2-4 day waves in the winter Antarctic mesosphere, *Geophys. Res. Lett.*, **20**, 1547-1550.
- Froidevaux, L., and Coauthors, 1996: Validation of UARS MLS ozone measurements, *J. Geophys. Res.*, **101**, 10 017-10 060.
- Girard, A., J. Besson, D. Brard, J. Laurent, M. P. Lemaitre, C. Lippins, C. Muller, J. Vercheval, and M. Ackerman, 1988: Global results of grill spectrometer experiment on board Spacelab 1, *Planet. Space Sci.*, **36**, 291-300.
- Goldsmith, P. F., M. M. Litvak, R. L. Plambeck, and D. R. Williams, 1979: Carbon monoxide mixing ratios in the mesosphere derived from ground-based microwave measurements, *J. Geophys. Res.*, **84**, 416-418.

- Gunson, M. R., C. B. Farmer, R. H. Norton, R. Zander, C. P. Rinsland, J. H. Shaw, and B.-C. Gao, 1990: Measurements of CH₄, N₂O, CO, and O₃ in the middle atmosphere by the atmospheric trace molecule spectroscopy experiment on Spacelab 3. *J. Geophys. Res.*, **95**, 13 867–13 992. .
- Gunson, M. R., and Coauthors, The atmospheric trace molecule spectroscopy (ATMOS) experiment: Deployment on the ATLAS space shuttle missions. *Geophys. Res. Lett.*, **23**, 2333–2336.
- Jackman, C. H., E. L. Fleming, S. Chandra, D. B. Considine, J. E. Rosenfield, 1996: Past, present, and future modeled ozone trends with comparisons to observed trends. *J. Geophys. Res.*, **101**, 28 753–28 767.
- Hartmann, D. L., 1983: Barotropic instability of the polar night jet stream. *J. Atmos. Sci.*, **40**, 817–835.
- , and R. R. Garcia, 1979: A mechanistic model of ozone transport by planetary waves in the stratosphere. *J. Atmos. Sci.*, **36**, 350–364.
- Haynes, P. H., and M. E. McIntyre, 1987: On the evolution of vorticity and potential vorticity in the presence of diabatic heating and frictional or other forces. *J. Atmos. Sci.*, **44**, 828–841.
- Hays, P. B., and J. J. Olivero, 1970: Carbon dioxide and monoxide above the tropopause. *Planet. Space Sci.*, **18**, 1729–1733.
- Holton, J. R., 1992: *An Introduction to Dynamic Meteorology*. 3d ed., Academic Press, 511 pp.
- Hoskins, B. J., M. E. McIntyre and A. W. Robertson, 1985: On the use and significance of isentropic potential vorticity maps. *Quart. J. Roy. Meteor. Soc.*, **111**, 877–946.
- Ishioka, K., and S. Yoden, 1994: Non-linear evolution of a barotropically unstable vortex. *J. Meteor. Soc. Japan*, **72**, 63–80.
- Kunzi, K. F., and E. R. Carlson, 1982: Atmospheric CO volume mixing ratio profiles determined from ground-based measurements of the $J = 1 \rightarrow 0$ And $J = 2 \rightarrow 1$ emission lines. *J. Geophys. Res.*, **87**, 7235–7241.
- Lait, L. R., and J. L. Stanford, 1988a: Applications of asymptotic space–time Fourier transform methods to scanning satellite measurements. *J. Atmos. Sci.*, **45**, 3784–3799.
- , and —, 1988b: Fast, long-lived features in the polar stratosphere. *J. Atmos. Sci.*, **45**, 3800–3809.
- Lary, D., M. P. Chipperfield, J. A. Pyle, W. A. Norton, and L. P. Riishojgaard, 1995: Three-dimensional tracer initialization and general diagnostics using equivalent latitude-potential-temperature coordinates. *Q. J. R. Meteorol. Soc.*, **121**, 187–210.

- Lawrence, B. N., and W. J. Randel. 1996: Variability in the mesosphere observed by the Nimbus 6 PMR. *J. Geophys. Res.*, **101**, 23 475–23 489.
- , G. J. Fraser, R. A. Vincent, and A. Phillips. 1995: The 4-day wave in the Antarctic mesosphere. *J. Geophys. Res.*, **100**, 18 899–18 908.
- Lin, S. J., and R. B. Rood. 1996: Multidimensional flux form semi-Lagrangian transport schemes. *Mon. Wea. Rev.*, **24**, 2046–2070.
- López-Puertas, M., M. A. López-Valverde, D. P. Edwards, and F. W. Taylor. 1993: Non-local thermodynamic equilibrium populations of the first vibrational excited state of CO in the middle atmosphere. *J. Geophys. Res.*, **98**, 8933–8947.
- López-Valverde, M. A., M. López-Puertas, C. J. Marks, and F. W. Taylor. 1993: Global and seasonal variations in the middle atmosphere carbon monoxide from UARS/ISAMS. *Geophys. Res. Lett.*, **20**, 1275–1278.
- , M. López-Puertas, J. J. Remedios, C. D. Rodgers, F. W. Taylor, E. C. Zipf, and P. W. Erdman. 1996: Validation of measurements of carbon monoxide from the improved stratospheric and mesospheric sounder. *J. Geophys. Res.*, **101**, 9929–9955.
- , M. López-Puertas, and C. J. Marks. Non-LTE modelling for the retrieval of CO abundances from ISAMS measurements. 1991: in *Technical Digest on Optical Remote Sensing of the Atmosphere*, **18**, 31–33. Optical Society of America, Washington, D.C.
- Madden, R. A., and P. R. Julian. 1971: Detection of a 40–50 day oscillation in the zonal wind in the tropical Pacific. *J. Atmos. Sci.*, **28**, 702–708.
- Manney, G. L., 1991: The stratospheric 4-day wave in NMC data. *J. Atmos. Sci.*, **48**, 1798–1811.
- , and W. J. Randel. 1993: Instability at the winter stratopause: A mechanism for the 4-day wave. *J. Atmos. Sci.*, **50**, 3928–3938.
- , T. R. Nathan, and J. L. Stanford. 1988: Barotropic stability of realistic stratospheric jets. *J. Atmos. Sci.*, **45**, 2545–2555.
- , R. Swinbank, S. T. Massie, M. E. Gelman, A. J. Miller, R. Nagatani, A. O'Neill, and R. W. Zurek. 1996: Comparison of UKMO and NMC stratospheric analyses during northern and southern winter. *J. Geophys. Res.*, **101**, 10 311–10 334.
- Matsuno, T., 1970: Vertical propagation of stationary planetary waves in the Northern Hemisphere. *J. Atmos. Sci.*, **27**, 871–883.
- McIntyre, M. E., 1980: Towards a Lagrangian-mean description of stratospheric circulations and chemical transport. *Phil Trans. Roy. Soc., London*, **A296**, 129–148.

- Murakami, M., 1979: Large-scale aspects of deep convective activity over the GATE area. *Mon. Wea. Rev.*, **107**, 994–1013.
- Murphy, A. K., 1985: Satellite measurements of atmospheric trace gases, Ph. D. thesis, Oxford Univ., Oxford, England.
- Nakamura, N., 1996: Two-dimensional mixing, edge formation, and permeability diagnosed in an arc coordinate. *J. Atmos. Sci.*, **53**, 1524–1537.
- , 1997: Leaky containment vessels of air: A Lagrangian-mean approach to the stratospheric tracer transport. *Advances in Fluid Mechanics Series: Dynamics of Atmospheric Flows. Part I. Atmospheric Transport and Diffusion Processes*, M. P. Singh and S. Raman, Eds. Ashurst Lodge, Computational Mechanics Publications.
- O'Neill, A., W. M. Grose, V. D. Pope, H. Maclean, and R. Swinbank, 1994: Evolution of the stratosphere during the northern winter 1991/92 as diagnosed from U. K. Meteorological Office analyses. *J. Atmos. Sci.*, **51**, 2800–2817.
- Orsolini, Y., and P. Simon, 1995: Idealized life cycles of planetary-scale barotropic waves in the middle atmosphere. *J. Atmos. Sci.*, **52**, 3817–3835.
- Prata, A. J., 1984: The 4-day wave. *J. Atmos. Sci.*, **41**, 150–155.
- Randel, W. J., 1990: Kelvin wave-induced trace constituent oscillations in the equatorial stratosphere. *J. Geophys. Res.*, **95**, 18 641–18 652.
- , 1993: Global normal-mode Rossby waves observed in stratospheric ozone data. *J. Atmos. Sci.*, **50**, 406–420.
- , and L. R. Lait, 1991: Dynamics of the 4-day wave in the Southern Hemisphere polar stratosphere. *J. Atmos. Sci.*, **48**, 2496–2508.
- , ———, and G. L. Manney, 1992: Dynamics of the 4-day wave: Evidence for instability in the winter upper stratosphere. Preprints, *Eighth Conf. on the Middle Atmosphere*, Atlanta, GA, Amer. Meteor. Soc., 106–109.
- Remedios, J. J., S. L. Ruth, C. D. Rodgers, F. W. Taylor, A. E. Roche, J. C. Gille, M. R. Gunson, J. M. Russell III, J. Park, E. C. Zipf, and P. W. Erdman, 1996: Measurements of methane and nitrous oxide distributions by the improved stratospheric and mesospheric sounder: retrieval and validation. *J. Geophys. Res.*, **101**, 9843–9871.
- Ricaud, P., J. de La Noë, B. J. Connor, L. Froidevaux, J. W. Waters, R. S. Harwood, I. A. MacKenzie, and G. E. Peckham, 1996: Diurnal variability of mesospheric ozone as measured by the UARS/MLS instrument: Theoretical and ground-based validations. *J. Geophys. Res.*, **101**, 10 077–10 089.
- Rodgers, C. D., 1976: Retrieval of atmospheric temperature and composition from remote measurements of thermal radiation. *Rev. Geophys. and Space Phys.*, **14**, 609–624.

- Rood, R. B., and A. R. Douglass. 1985: Interpretation of ozone temperature correlations. 1. Theory. *J. Geophys. Res.*, **90**, 5733–5744.
- Rosier, S. M., B. N. Lawrence, D. G. Andrews, and F. W. Taylor. 1994: Dynamical evolution of the northern stratosphere in the early winter 1991/92, as observed by the improved stratospheric and mesospheric sounder, *J. Atmos. Sci.*, **51**, 2783–2799.
- Ruth, S. L., J. J. Remedios, B. N. Lawrence, and F. W. Taylor. 1994: Measurements of N₂O by the UARS improved stratospheric and mesospheric sounder during the early northern winter 1991/92, *J. Atmos. Sci.*, **51**, 2818–2833.
- Salby, M. L., 1982a: Sampling theory for asynoptic satellite observations. Part I: Space-time spectra, resolution, and aliasing. *J. Atmos. Sci.*, **39**, 2577–2600.
- , 1982b: Sampling theory for asynoptic satellite observations. Part II: Fast Fourier synoptic mapping. *J. Atmos. Sci.*, **39**, 2601–2614.
- Schoeberl, M. R., and Coauthors. 1989: Reconstruction of the constituent distribution and trends in the Antarctic polar vortex from ER-2 flight observations, *J. Geophys. Res.*, **94**, 16 815–16 845.
- , and L. R. Lait. 1991: Conservative coordinate transformations for atmospheric measurements. In EOS NATO Summer School. G. Visconti and J. Gille, Ed. American Geophysical Union.
- Solomon, S., R. R. Garcia, J. J. Olivero, R. M. Bevilacqua, P. R. Schwartz, R. T. Clancy, and D. O. Muhleman. 1985: Photochemistry and transport of carbon monoxide in the middle atmosphere, *J. Atmos. Sci.*, **42**, 1072–1083.
- Sutton, R. T., H. Maclean, R. Swinbank, A. O'Neill, F. W. Taylor. 1994: High-resolution stratospheric tracer fields estimated from satellite observations using Lagrangian trajectory calculations., *J. Atmos. Sci.*, **51**, 2995–3005.
- Taylor, F. W., and Coauthors. 1993: Remote sensing of atmospheric structure and composition by pressure modulator radiometry from space: the ISAMS experiment on UARS, *J. Geophys. Res.*, **98**, 10 799–10 814.
- Thorpe, A. J., and C. H. Bishop. 1995: Potential vorticity and the electrostatics analogy: Ertel-Rossby formulation. *Quart. J. Roy. Meteor. Soc.*, **121**, 1477–1495.
- Venne, D. E., and J. L. Stanford. 1979: Observations of a 4-day temperature wave in the polar winter stratosphere. *J. Atmos. Sci.*, **36**, 2016–2019.
- , and ———, 1982: An observational study of high-latitude stratospheric planetary waves in winter. *J. Atmos. Sci.*, **39**, 1026–1034.
- Waters, J. W., W. J. Wilson, and F. I. Shimabukuro. 1976: Microwave measurements of carbon monoxide, *Science*, **191**, 1174–1175.

- Wofsy, S. C., J. C. McConnell, and M. B. McElroy, 1972: Atmospheric CH₄, CO, and CO₂. *J. Geophys. Res.*, **77**, 4477-4493.
- . Interactions of CH₄ and CO in the earth's atmosphere, 1976: . *Annu. Rev. Earth Planet. Sci.*, **4**, 441-469.
- Ziemke, J. R., and J. L. Stanford, 1990: One-to-two month oscillations in the stratosphere during southern winter. *J. Atmos. Sci.*, **47**, 1778-1793.

ACKNOWLEDGMENTS

I would like to thank my wife and best friend, Ruthie, for her unfailing love and support, and my son, Peter, who helped me set priorities. I thank my parents, Gerald and Corinne Allen, and my parents-in-law, Charles and Deloris Gosling, who helped make this accomplishment possible. I also thank Dr. Ruth R. Reck, who helped make my time at Argonne so enjoyable. Finally, I thank Dr. John L. Stanford for his advice and guidance during my time at ISU. His quiet encouragement and constant support gave me the confidence to complete this work.

This research was supported by National Aeronautics and Space Administration Grant NAG 5-2787. Part of the work was done as a guest graduate student in the Environmental Research Division of Argonne National Laboratory.